HER🌑N

Contents

THEORY AND EXPERIMENTS ON THE BEHAVIOUR OF CRACKS IN CONCRETE SUBJECTED TO SUSTAINED SHEAR LOADING

J. W. Frénay

IMAG Institute of agricultural engineering,
Structures Department, formerly
Delft University of Technology,
Stevin Laboratory

Summary

There is a lack of information about the behaviour of cracked concrete subjected to in-plane sustained shear loading. This subject is the aim of the present study. A short literature survey discusses the basic mechanisms of shear transfer across a crack, viz. interlocking of the opposing crack halves due to protruding irregularities and dowel action by the embedded reinforcing bars that cross the shear plane. The combined mechanism of the short-term tests is significantly affected by the concrete compressive strength, the steel yield stress of the bars and by the restraint of the crack.

Next, tests were conducted on 46 push-off specimens each provided with a central crack. The initial crack width did not exceed 0.10 mm. High-strength concrete was chosen with 28-day cube compressive strengths $f_{ccm} = 51$ or 70 N/mm^2. To analyse the shear transfer mechanisms separately, the $120 * 300$ mm^2 shear plane was restrained in two ways. Either free steel rods were applied, or 8 mm diameter reinforcing bars ($\varrho = 1.1$–2.2%) perpendicularly crossed the crack plane. The adjusted constant stress levels ranged from 45 to 89% of the static shear strength. The movements parallel and perpendicular to the crack plane were regularly recorded on either side of the specimen, for at least 90 days. The recorded instantaneous and time-dependent displacements have been mathematically represented as functions of the experimental parameters. A sensitivity analysis proved the large influence of f_{cc} on the response. Shear stress-crack width relations of the reinforced cracks showed a gradual "weakening". Generally, a highly non-linear response occurred with respect to the concrete grade and the adjusted shear stress level. Supplementary research focused on microscopic observations of the dowel and on the restraint stiffness of the crack plane, measured by means of strain gauges.

The test results have been theoretically described by an extended version of Walraven's two phase model accounting for the interlocking of aggregates and matrix material in the crack. The dowel mechanism is described by a modification of Rasmussen's formula. A damage parameter $\lambda_f(t) \leq 1.0$ is introduced that accounts for a gradual decrease in the short-term concrete strength according to $\lambda_f(t) * f_{cc}$. The reduction represents the deterioration of the cement-based matrix material. The two transfer mechanisms are equally affected by $\lambda_f(t)$; it has been compared with a simple model derived from data of uniaxial creep tests on cement-based material described in the literature.

A second adaptation concerns the static friction coefficient $\lambda_\mu(t) * \mu$ for the contact between aggregate particles and matrix material. Both parameters λ_f and λ_μ appear proportional to $\log(t)$, and they provide reliable predictions of the experimentally obtained time-dependent stress-displacement relations of a single crack. The results of this study should be used in non-linear finite element programs to support the design of complex structural concrete applications.

Theory and experiments on the behaviour of cracks in concrete subjected to sustained shear loading

1 Introduction

The development of computer technology during the last few decades has provided new design tools for the structural engineer. At the same time, the building industry underwent an evolution characterised by:
- the erection of huge, large-scale structures;
- the exploration of new fields of interest, for which concrete is applied under different circumstances. Examples are: nuclear containment vessels, offshore platforms and storage facilities for liquefied gasses;
- a trend to build more efficiently and more cost-effectively.

Special attention had to be paid to structural safety. On the one hand more severe loading conditions were encountered, on the other hand complex and slender structures react rather sensitively to applied loads or deformations. These phenomena do not allow conventional design techniques and criteria to be applied in advance, nor do they permit reliance on engineering experience only. Local damage or even structural failure could spell dire consequences for the community, both temporally and spatially. To cope with these problems elaborate computational methods have been developed based on ongoing research.

The *theoretical* research focused on the development of realistic constitutive laws for concrete [3, 6, 47]. The primary purpose of these efforts was the implementation of the numerical models in finite element programs. Detailed *experimental* investigations were needed in order to supply reliable data for these models. An important object of research concerns the *in-plane* shear transfer across existing cracks in concrete. Interface shear transfer may make a vital contribution to the bearing capacity of structures [1, 22, 23, 37]. While the behaviour of reinforced concrete members has been extensively investigated in the case of bending and the physical model is generally accepted, there is still a lack of knowledge and modelling relating to shear forces in cracked concrete. The reason is that shear loading leads to complicated physical mechanisms, such as multiaxial stress conditions with inclined crack formation in the flanges of beams or walls, interlocking of cracks, dowel action and reduced bond resistance of the embedded bars. That is why the conventional beam theory with plane cross-sections cannot simply be applied to the shear design.

With respect to shear, Mörsch [52] developed design formulas for reinforced concrete beams assuming a truss model with 45° diagonal compression struts. Today, extensive research has led to modern shear design criteria, such as the *shear friction analogy* [33], the *yield-line theory* [38] and the "refined" *truss model* with a variable inclination as mention in the Eurocode [19, 61]. The design shear force may depend on the com-

pressive strength of the concrete diagonals between the pattern of parallel cracks. The distribution of forces is represented by truss action (shear reinforcement and inclined concrete struts). Because of the action of aggregate interlock in the cracks, a redistribution of forces is possible. The direction of the compression struts decreases with the increase of the load, so that more stirrups are activated. As a result, the stress in the concrete diagonals also increases. Failure occurs if the crushing strength of the concrete is reached. Recently, various authors have reported on the structural contribution of the shear transfer across cracks, see in [15, 39, 40, 57, 73].

Much research effort has been devoted to the shear transfer mechanism across a single crack [3, 74]. The behaviour of cracked reinforced concrete panels can now be satisfactorily predicted for monotonic short term shear loading conditions. However, nothing is known about the transfer mechanism in the case of a *sustained* shear loading. An additional problem concerns cracks in *high-strength* concrete, with a view to its applications in offshore conditions [12, 18, 26, 61]. This research aims at predicting the time-dependent mechanical behaviour of cracked reinforced concrete when subjected to in-plane sustained shear loading. As no experimental data were available yet, a number of sustained shear tests were carried out. Special attention was paid to high-strength concrete, small initial crack widths (0.01–0.10 mm) and fairly high shear stress levels. This report begins with a literature survey reviewing recent research into shear transfer across a crack in concrete. Chapters 3 and 4 outline the set-up of an experimental program and include the most important test results, especially regarding the time-dependent displacement increases of the opposing crack faces due to an external sustained shear loading. Chapter 5 is concerned with the theoretical modelling of the observed crack response. The conclusions, the notation and a list of references are given in the last part of this study.

2 Literature survey

2.1 *Basic mechanisms of shear transfer*

This chapter is restricted to the transfer mechanisms occurring under monotonic shear loading. Fig. 2.1a shows a unit area of the crack plane which is crossed by one embedded reinforcing bar at a random angle $\theta\,(0° < \theta \leq 90°)$. The initial crack displacements are a separation $\delta_{no} > 0$ and a slip $\delta_{to} = 0$. In medium-strength concrete, cracks usually initiate along the relatively weak bond zones between the matrix material and the aggregate particles. The contact areas between the opposing crack faces depend on the mix composition and on the actual crack displacements [74]. The application of a shear stress τ results in an increase of these displacements. The displacement values depend on the normal and shear stiffness of the crack plane. The reinforcing bar in Fig. 2.1b accounts for a restraint of the crack plane. Once the axial bar stiffness is too low, for instance due to lack of bond or yielding of the steel bar, no equilibrium can be found and the displacements increase more and more. This case is defined as shear failure, characterized by the shear strength τ_u.

6
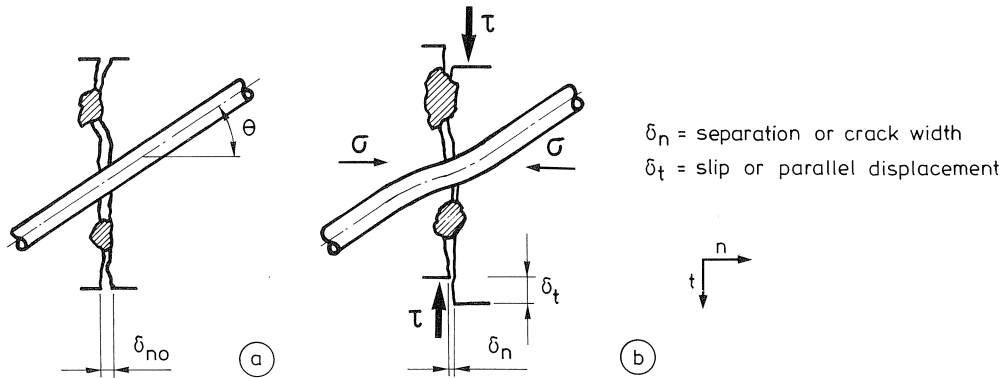
Fig. 2.1. Unit area of crack plane in (a) unloaded and (b) loaded state.

δ_n = separation or crack width
δ_t = slip or parallel displacement

$$\tau_d = \frac{\text{dowel force } V_d}{\text{crack area } A_c}$$

aggregate interlock   dowel action
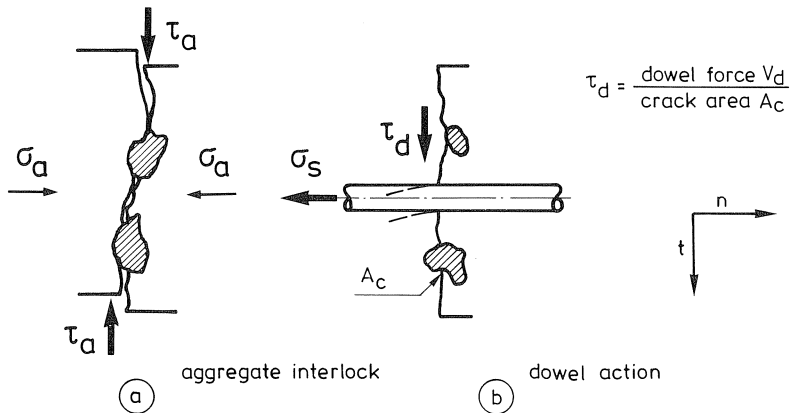
Fig. 2.2a–b. Basic mechanisms for shear transfer across a crack; $\theta = 0°$.

In Figs. 2.2a–b the two transfer mechanisms can be identified separately:

a. *Aggregate interlock of the rough crack faces.* Generally, the crack follows an irregular path and shows an uneven surface. Shear transfer is provided by the mechanical locking of the particles protruding from one face and pushing into the matrix of the opposing crack face;

b. *Dowel action of the reinforcing bar.* Dowel action is defined as the load carrying capacity of a bar in the direction perpendicular to the longitudinal bar axis. For $\theta \neq 90°$, the bars will contribute to the stiffness both parallel and perpendicular to the crack plane.

An interaction of both mechanisms takes place in cracked reinforced concrete. The application of shear stress causes slip and in addition makes the crack surface tend to separate slightly. The reinforcing bar is stressed in tension; the steel tensile strains and the bond slip permit a crack width increase. Moreover, the steel bars restrain the crack

7

plane and hence they influence the dowel mechanism, which initially determines the direction of the crack-opening [59]. In assessing the mechanisms of shear transfer it is clear that the primary variables are [74]:
– concrete grade and bar characteristics (diameter, steel yield strength);
– restraint perpendicular to the crack plane.
Section 2.2 deals with previous experiments related to the static shear transfer mechanisms.

2.2 Experiments on shear transfer

2.2.1 Aggregate interlock mechanism

One of the first investigations was carried out by Colley and Humphrey [11] in 1967. Alternating repeated shear forces were applied on a centric crack of a concrete pavement, thus simulating heavy traffic loading. The number of cycles to failure depended on the type and size of the aggregates used and decreased as soon as a certain crack width was exceeded.

In the years 1968–1980 several static shear tests were conducted on cracked concrete. Usually, the test set-up concerned two plain concrete blocks separated by a preformed crack which was sufficiently restrained. Shear force-displacement relations were established by, amongst others, Fenwick and Paulay [22], Taylor [69] and White and Holley [76].

Either a constant crack width was maintained or the crack width was variable. In general the initial crack widths were rather large, i.e. $\delta_{no} = 0.25$–0.75 mm. The initial crack widths are related to the field of application; structures with cracks caused by external loads and/or imposed deformations, cracks due to over-pressurization in a nuclear containment vessel, etc. The test results were significantly affected by the size and type of aggregate, the concrete grade, δ_{no} and by the restraint stiffness. Based on displacement-controlled static shear loading tests, Paulay and Loeber [55] found an empirical shear stress-displacement relation for their variable crack width tests (constant stress-crack width ratio):

$$\tau_a = 0.51 + 7.07\sqrt{\delta_t} \quad [\text{N/mm}^2] \tag{2.1}$$

Houde and Mirza [35] performed similar push-off tests and found that τ_a is almost proportional to $\sqrt{f_{cyl}}$ and $\delta_{no}^{-1.5}$. Walraven [74] used 32 push-off type specimens similar to those of Mattock [46], see Fig. 2.3a. By means of nuts the external restraint rods were fastened to stiff steel plates fixed on the small sides of the specimens. Dowel action of these bars was negligible. The shear loading was applied in a displacement-controlled manner. The variables of the tests were: initial crack width (0.01; 0.2 and 0.4 mm), 150 mm cube strength and type of aggregate (Fuller grading curve, gravel: $f_{cc} = 19.9$–56.1 N/mm^2, light-weight: $f_{cc} = 38.2$ N/mm^2) and its maximum size (16 and 32 mm). The test results of six specimens are presented in Fig. 2.3b. Empirical bilinear stress-displacement relations were found which accurately fit with the recorded data. The

8

	δ_n [mm]	σ_c [N/mm²]
A	0	6.8
B	0	3.6
C	0.4	1.0
D	0.2	1.6
E	0.2	1.4
F	0.2	0.4
G	0.4	0.3

Note:

σ_c refers to $\delta_n = 0.6$mm
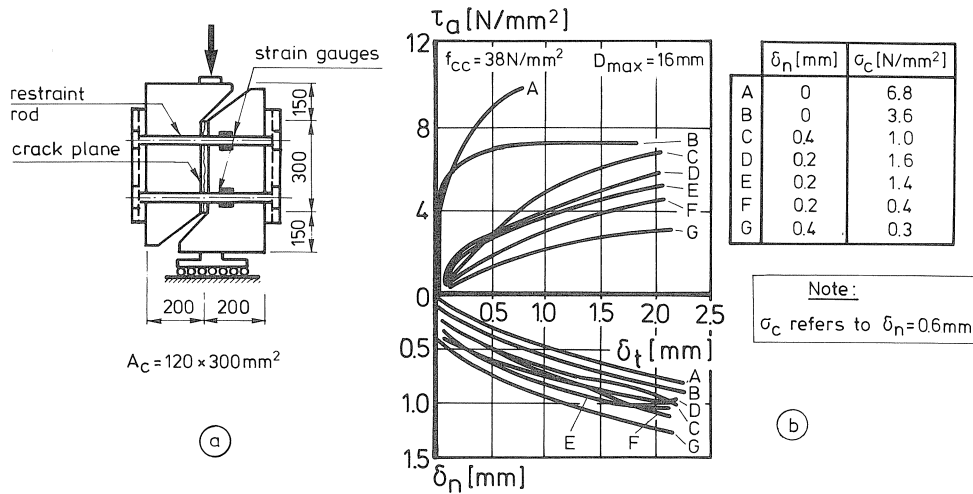
Fig. 2.3. Tests of Walraven [74]; (a) specimen with external restraint rods and (b) shear stress-displacement relations and measured crack-opening curves for normal-weight concrete.

light-weight concrete exhibited a less steep crack-opening curve, indicating a relatively smooth crack surface. This was probably caused by cracks that run mainly through the aggregate particles which are weaker than the matrix material.

Several recent research projects have focused on the shear transfer of plain concrete with a relatively small initial crack width of 0.05–0.20 mm. Tests were conducted by Divakar et al. [16], Millard et al. [49] and Nissen [54]. Tassios et al. [68] investigated prismatic concrete blocks in which two small parallel cracks ($\delta_{no} < 0.1$ mm) were initiated, see Fig. 2.4a. The test variables were: roughness of the interface (smooth, sand-blasted or rough), concrete cylinder strength ($f_{cyl} = 16$–40 N/mm² using crushed limestone with $D_{max} = 30$ mm) and the constant compressive stress on the crack plane

Fig. 2.4. (a) Test set-up of Tassios et al. [68] and (b) measured crack-opening paths.

9

($\sigma_c = 0.5$–2.0 N/mm^2). Fig. 2.4b shows that the crack-opening curves seem to be influenced by the normal compressive stress. This is in accordance with the findings of other researchers [16, 49, 54, 74].

2.2.2 Dowel mechanism

The following subjects will be outlined in this section:
- a short review of *the first studies* of the dowel mechanism, including the load-displacement behaviour and the dowel strength;
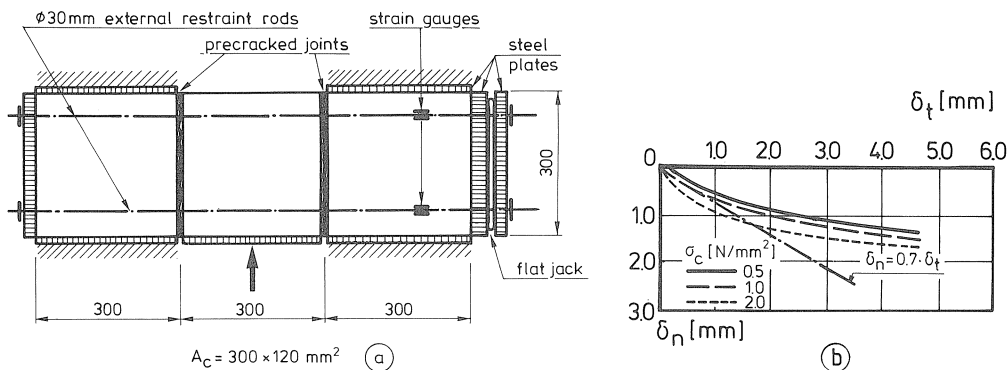- recent *experimental research* on dowel action in two-dimensional elements, such as containment vessels, shell structures, etc.

First research projects

Teller and Sutherland [70] studied the dowel action of transverse expansion joints in concrete pavements. Timoshenko et al. [71] modelled the dowel as a beam of semi-infinite length, placed on a foundation assumed to show linear-elastic material behaviour. The mathematical solution is characterized by the modulus of subgrade support k. Experimental values differ widely, $k = 500$–1500 N/mm^3 [43]. One specific reason is the non-linear behaviour of the concrete due to crushing; thus k should vary parallel to the bar axis. Moreover, the dowel behaviour is influenced by the casting direction, the concrete strength, the bar characteristics and the position of the bar.

The supporting concrete situated directly under the bar is subjected to radial and circumferential stresses. Marcus [43] investigated uniformly loaded embedded reinforcing bars (Fig. 2.5a). He found that the bearing strength exceeds f_{cc}. Fig. 2.5b
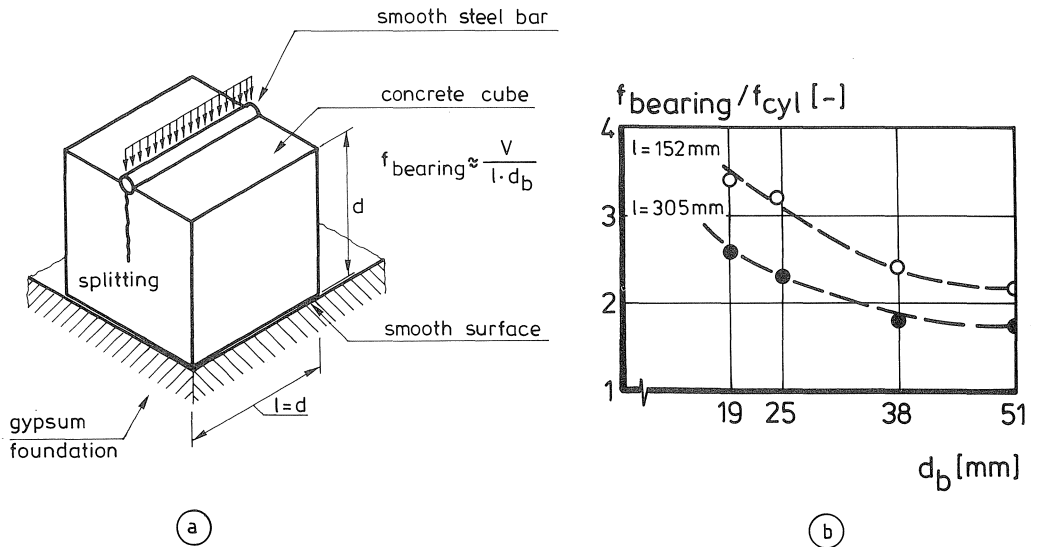

Fig. 2.5.   (a) Test set-up of [43] and (b) results for $f_{cyl} = 21$–29 N/mm^2.

10

shows that this ratio depends on the bar diameter and the embedment length. In general the bearing stresses in the concrete account to a large extent for the shear transfer of the dowel. Broms [8] proposed a simple model for the dowel mechanism based on the lateral resistance of foundation piles in cohesive soil. Due to the development of a plastic hinge in the pile, the model of a beam on an elastic foundation is not appropriate here. A similar behaviour can be expected in the case of a dowel embedded in concrete.

Recent experimental research

Basically three types of investigation were performed (Figs. 2.6a–c). The direct shear tests are often related to small diameter bars and a thick concrete cover, so that the bearing capacity is governed by steel yielding and concrete crushing under the bar. Divided-beam and beam-end tests were often developed in order to study the concrete splitting failure mechanism and the anchorage length of the bar.

Rasmussen [60] carried out ten direct dowel tests on smooth steel bars (Fig. 2.7a) with $f_{cyl} = 11\text{-}44\,\text{N/mm}^2$; $f_{sy} = 225\text{-}439\,\text{N/mm}^2$ and $d_b = 16\text{-}26\,\text{mm}$. On the basis of a simple model according to Fig. 2.7b, he found:

$$V_{du} = \bar{c} \cdot [\sqrt{(\varepsilon c)^2 + 1} - (\varepsilon c)] \cdot d_b^2 \sqrt{f_{cyl} \cdot f_{sy}} \quad [\text{N}] \tag{2.2}$$

where $\varepsilon = 3e \cdot \sqrt{f_{cyl}/f_{sy}}/d_b$. From tests $\bar{c} = 1.31$ was found if e is neglected.

direct dowel test   divided-beam test   beam-end test

(a)   (b)   (c)
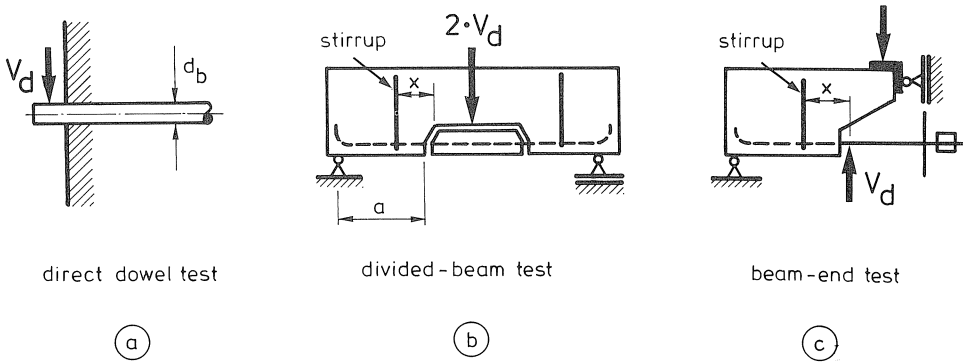
Fig. 2.6a–c.   Different types of dowel test set-up.

Additional investigations on dowel action are reported by Dulacska [17] and in [4, 22]. Jimenez et al. [37] found that the "initial" shear stiffness was about proportional to $d_b^{9/4}$. The authors reported that the axial steel stress caused significant damage to the concrete surrounding the bar on both crack halves. Utescher et al. [72] investigated the behaviour of smooth embedded dowels. In the case of a thick concrete cover ($c_{//} >$ approximately $5d_b$) a small crater-shaped area was observed close to the bar, indicating high local bearing stresses. Failure was satisfactorily described by Rasmussen's equation (2.2).

Tassios et al. [68] performed dowel tests and found that the plastic hinge is situated $0.6d_b - d_b$ away from the shear plane. The plastic yielding moment of the bar is

expressed as a function of the load eccentricity and the bearing strength, so that:

$$V_{du}^2 + (10 f_{cyl} \cdot e \cdot d_b) \cdot V_{du} - 1.7 d_b^4 \cdot f_{cyl} \cdot f_{sy} = 0 \quad [N^2] \tag{2.3}$$

For $e = 0$ mm equation (2.2) is found. The authors gave a qualitative indication of the reduced dowel action in case of axial stresses in the bar.
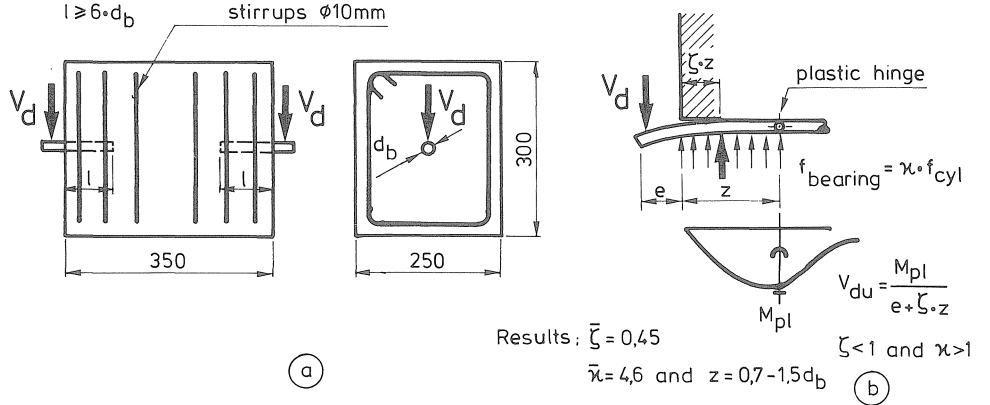
Fig. 2.7. Experiments of Rasmussen [60]; (a) test set-up and (b) assumed load transfer of a dowel ($z = 0.7{-}1.5 d_b$; $\bar{\zeta} = 0.45$; $\bar{\varkappa} = 4.6$).

With respect to the divided-beam tests (Fig. 2.6b) several experiments were carried out. Information about the test set-ups is summarized in Table 2.1. Usually, longitudinal (side) splitting occurred and a residual dowel strength of $0.5{-}0.8 V_{dcr}$ was reported.

Table 2.1.   Review of divided-beam tests conducted

reference	no. of tests	f_{cyl} [N/mm²]	d_b [mm]	no. of bars	$c_{//}/d_b$	δ_{no} [mm]	stirrups
[2]	31	12–62*	16–26	2–8**	1 –2.2	0.1–10	yes
[28]	14	–	10–22	2	2.2–3.1	2	no
[41]	12	19	22–29	2	1.2–2	0.6	no
[69]	46	13–39	6 or 22	2	1.2	1.5	yes

* f_{cc}-values
** in two layers

2.2.3   Combined mechanism

In the preceding sections 2.2.1 and 2.2.2 the individual mechanisms have been experimentally isolated to assess their most important parameters.
Attention is now paid to the shear behaviour of cracked reinforced concrete.

Observations near shear failure
Part of the research originally focused on the shear transfer problem of a slab. Investiga-

tions are reported by Johansen [38], Mills [50], Nielsen [53], Prince and Kemp [58] and Morley [64].

None of the tests considers either the effects of confinement of the reinforcement near the crack plane due to concentrated bearing stresses or shear transfer due to aggregate interlock. Many static *in-plane* push-off tests have been performed, originally intended to determine the shear strength of reinforced connections between precast and cast-in-place concrete. See also Fenwick et al. [22] and Hanson [33]. Other research efforts are summarized in Table 2.2. From the observations it can be concluded that:

- for *low reinforcement ratios* steel yielding and slip in the shear plane occurred. For $\varrho f_{sy} < 4$ N/mm^2 the concrete strength did not affect τ_u;
- for *high reinforcement ratios* slip took place as a result of rotation of the concrete struts between the parallel cracks, see Fig. 2.8a. The crack roughness and the reinforcement provided a "locking up" so that the shear strength was hardly affected by the presence of the crack. This phenomenon did not occur in light-weight concrete [46];
- Mattock et al. [45] reported reduced shear strengths in case of reinforcement provided with rubber sleeves on each side of the crack plane.
  Ultimate slips were six times higher. Walraven [74] pointed out that the sleeves reduce both dowel action and the bond behaviour of the bars.

The shear friction hypothesis for cracked reinforced concrete was proposed by Birkeland and Birkeland [5], see Fig. 2.8b. Equilibrium can be expressed in terms of stress:

$$\tau_u = \varrho f_{sy} \cdot \tan{(\theta)} \quad [\text{N/mm}^2] \tag{2.4a}$$

where $\tan{(\theta)}$ is the coefficient of internal friction (based on tests [33], $\tan{(\theta)} = 1.7$ for monolithic concrete and 0.8–1 for ordinary construction joints). Mast [44] proposed the
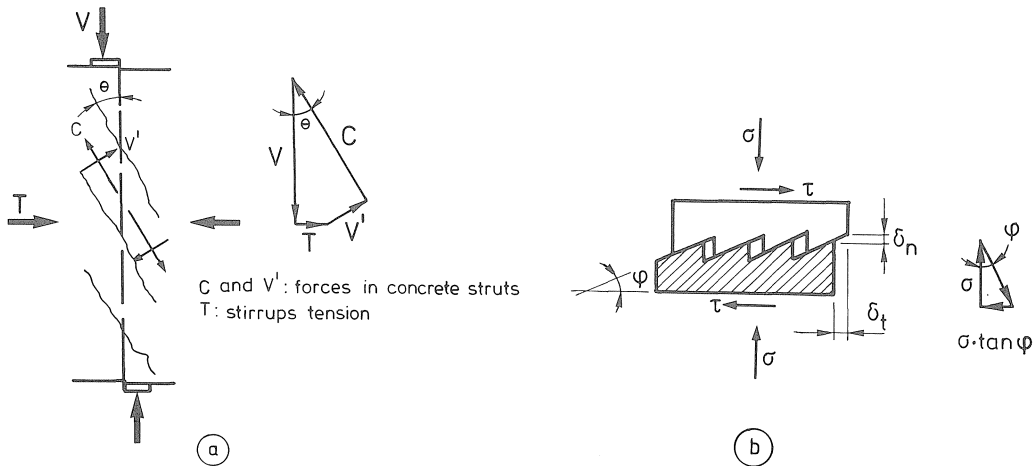

Fig. 2.8. (a) Shear transfer in initially uncracked concrete [45] and (b) the shear-friction model.

13

use of $\varrho f_{sy} + \sigma_N$ in the above formula, where σ_N denotes the external stress imposed perpendicular to the shear plane. Moreover, a cohesive strength (or: "dowel strength") was added according to [21, 34, 36]:

$$\tau_u = 2.8 + 0.8(\varrho f_{sy} + \sigma_N) \quad [\text{N/mm}^2] \tag{2.4b}$$

where $\tau_u < 0.3 f_{cyl} < 10.8$ N/mm². Mattock et al. [46] reported cohesive strengths of 1.40–1.75 N/mm² in the case of light-weight concrete, with $\tau_u < 0.2 f_{cyl} < 5.6$ N/mm².

Table 2.2. Overview of push-off tests ($D_{max} = 16$–22 mm)

reference	type of spec.*	number of spec.**	f_{cyl} [N/mm²]	ϱf_{sy}***** [N/mm²]	d_b [mm]	θ [–]
[34]	ps	15/23	17–36	0.4–10.2	9.5–16	–
	pl	6/6	35	1.3– 5.3	6.4– 9.5	–
	mp***	6/10	28–45	2.2– 6.9	9.5	0–75°
[45]	cp	0/12	28	2.5– 4.1	9.5–13	$e > 0$
	ps****	9/6	28	3.6– 5.9	9.5	–
[46]	po	28/32	18–42	0 – 9.8	9.5	lightw. c.
[56]	po	6/30	21–31	0.9– 4.3	6.5–13	–
[74]	see Fig. 2.3a	0/33	17–48	1.1–15.2	4 –16	–
		0/8	29	2.4	8	45–135°

    * cp = corbel push-off; ps = push-off; pl = pull-off; mp = modif. push-off
    ** uncr/cr.
    *** σ_N = compression
    **** σ_N = tension
    ***** $f_{sy} = 298$–465 N/mm²

Observations before failure

The first investigations focused on the shear stress-displacement behaviour of push-off specimens [45, 56]. Displacement-controlled shear tests on cracked reinforced concrete specimens were also conducted by Walraven [74], for $\delta_{no} = 0.01$–0.09 mm. See Table 2.2 and Figs. 2.3a and 2.9a-b. The crack-opening curves hardly appeared to be influenced by the reinforcement characteristics ($d_b = 4$–16 mm; $\theta = 0$–90°; $\varrho = 0.56$–2.24% and $D_{max} = 16$ mm). Only for $\varrho < 1.0\%$ was there an influence of D_{max}. The light-weight and the high-strength gravel concrete revealed rather flat crack-opening curves (also observed on specimens provided with rubber sleeves). In contrast with an unreinforced crack, the crack-opening curve of a reinforced crack is hardly affected by the axial stiffness. Other tests were carried out by Jimenez et al. [37] and by Tassios et al. [68].
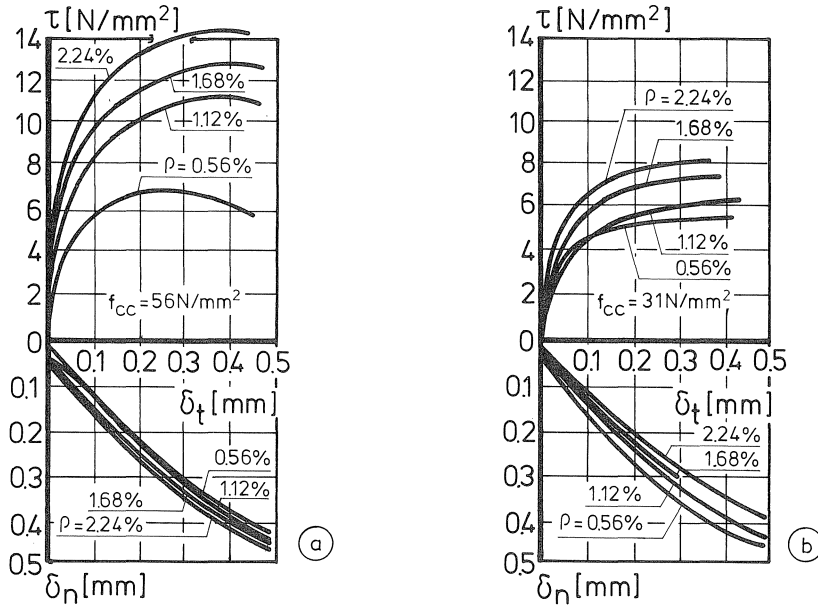
14

Fig. 2.9.   Tests of Walraven [74]; (a) $f_{cc} = 31$ and (b) $f_{cc} = 56$ N/mm^2.

2.3   *Modelling of shear transfer*

In this section the modelling of the in-plane shear transfer in cracked concrete is outlined for a monotonically increasing shear loading. The models should be physically based and it should be possible to implement them in finite element programs.

Two extreme crack response curves can be distinguished for the case of a displacement-controlled shear loading [23, 54], namely retaining a constant crack width, related to an *infinite* normal stiffness of the crack plane, or a constant normal stress which can be achieved by a constant external normal force together with a *zero* normal stiffness. A theoretical model should consider the interaction between the stresses and displacements $(\sigma, \tau, \delta_n, \delta_t)$. A few recently developed theoretical models will be reviewed:

a. Rough-crack model of Bazant and Gambarova [3].

This model is a mathematical description of the observed crack behaviour. The interface stresses depend on the ratio δ_t/δ_n, D_{max} and f_{cyl}.

b. Two-phase model of Walraven [74].

This model suggests that concrete is a two-phase material consisting of stiff aggregate particles embedded in an ideally-plastic cement matrix (Figs. 2.10a–b). The shear plane consists of a distribution of rigid spheres of a range of sizes embedded to various depths in the matrix material. An expression is derived to predict the chances of finding a particular sized aggregate particle at a certain embedment depth. Equilibrium is related to frictional sliding and crushing of matrix material along the contact areas a_x and a_y (Fig. 2.10c). These depend on δ_t, δ_n and on the mix proportions (D_{max} and the volumetric percentage of aggregate). The constitutive relations of the crack are:

15

$$\sigma_{\mathrm{a}} = \sigma_{\mathrm{pu}} \cdot (A_{\mathrm{x}} - \mu A_{\mathrm{y}}) \quad \text{and} \quad \tau_{\mathrm{a}} = \sigma_{\mathrm{pu}} \cdot (A_{\mathrm{y}} + \mu A_{\mathrm{x}}) \quad [\text{N/mm}^2] \tag{2.5a}$$

$$\mu = \tau_{\mathrm{pu}}/\sigma_{\mathrm{pu}} = \text{coefficient of friction} = 0.40 \qquad [-] \tag{2.5b}$$

$$\sigma_{\mathrm{pu}} = \text{matrix yield strength} = 6.39 f_{\mathrm{cc}}^{0.56} \qquad [\text{N/mm}^2] \tag{2.5c}$$

The model agrees well with Walraven's static tests and with those of Paulay et al. [55]. Combining equations (2.5a–c) results in the curves presented in Fig. 2.10d; the "free slip" at $\sigma_{\mathrm{a}} = 0$ depends on the initial crack-opening.
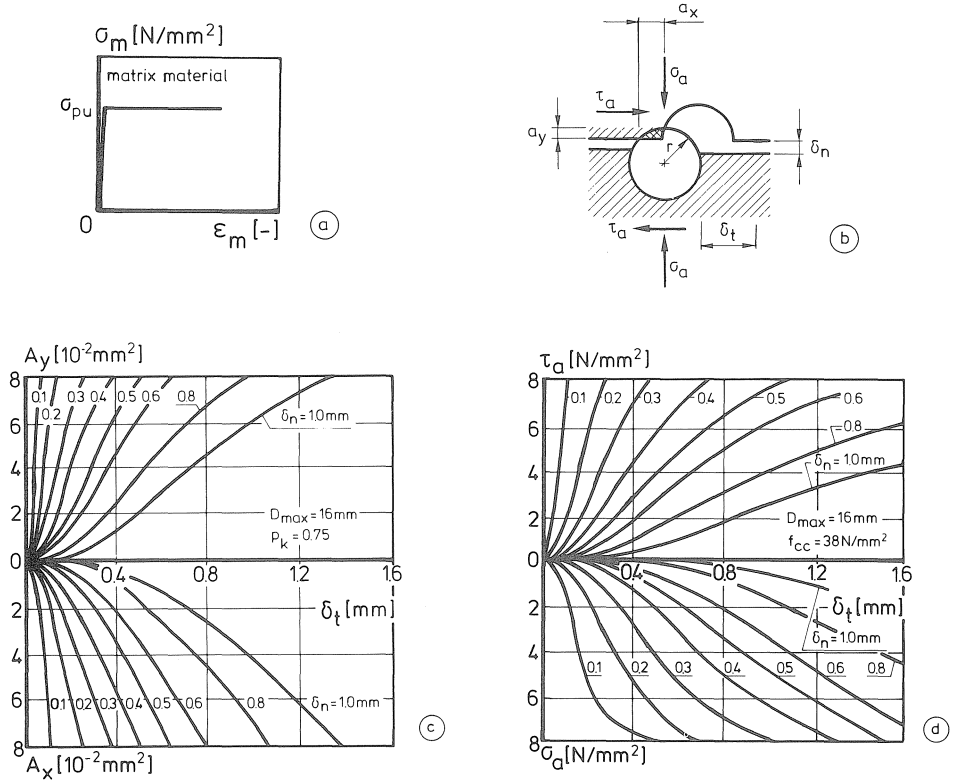
Fig. 2.10.   Model of Walraven [74]; (a)–(b) assumed matrix deformation; (c) contact areas and (d) stresses for a single crack.

c. Other models.

These were presented by Divakar et al. [16], Fardis et al. [20], Millard et al. [49], Nissen [54] and Yoshikawa et al. [79]. Usually, the normal stress on the shear plane is written as a function of the initial shear stiffness, see Fig. 2.11. Pruijssers [59] stated that in reinforced cracked concrete, the initial crack-opening direction is governed by deformation of the bars. After the development of plastic hinges in the bars, aggregate interlock becomes the dominant mechanism. This approach is illustrated and extended in chapter 5.
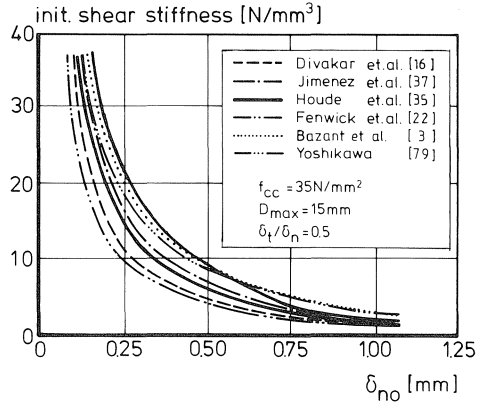
Fig. 2.11. Measured and calculated initial shear stiffness values.

A few remarks are now made on the numerical modelling techniques for the shear transfer mechanism. Two distinct approaches of the finite element method [23, 80] have been developed in order to model the cracking of concrete, see Figs. 2.12a–b.
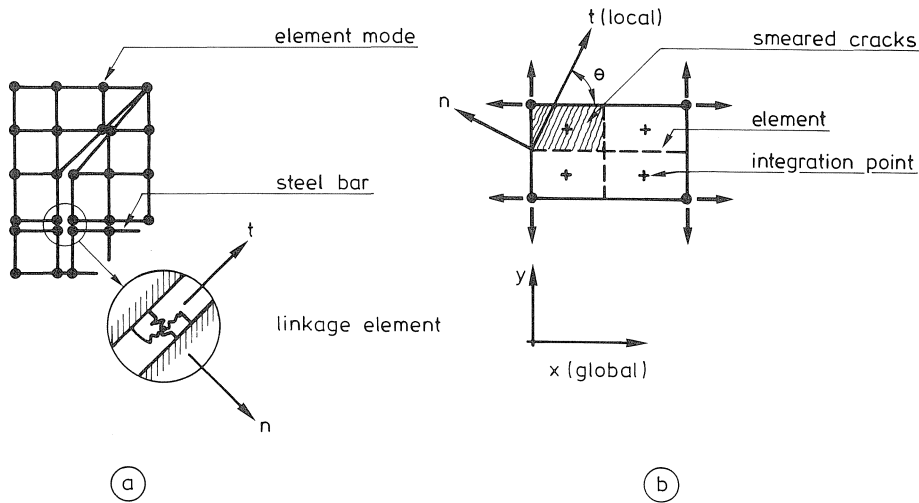
Fig. 2.12. (a) Discrete and (b) smeared crack approach.

The *discrete* method allows cracks to propagate usually only along the boundaries of elements by a disconnection of the nodes. The method is a powerful tool for local fracture prediction. The *smeared* crack approach [48, 63] represents relative crack displacements by crack strains which could be regarded as an infinite number of small parallel equidistant cracks.

The reduced shear transfer due to cracks in plain or reinforced concrete, is usually expressed by the retention factor β (Fig. 2.13a):

$$G_{cr} = \beta\, G_{co} \quad [\text{N/mm}^2] \tag{2.6a}$$

where $G_{co} = 0.5 E_c/(1 + v_c)$. From Fig. 2.13a it can be derived that

$$G_{cr} = (G_{co}^{-1} + (K \cdot l_c)^{-1})^{-1},$$

where $l_c = $ crack spacing and $K = $ shear stiffness of a crack. Note, that $K \to \infty$ leads to $\beta = 1.0$.
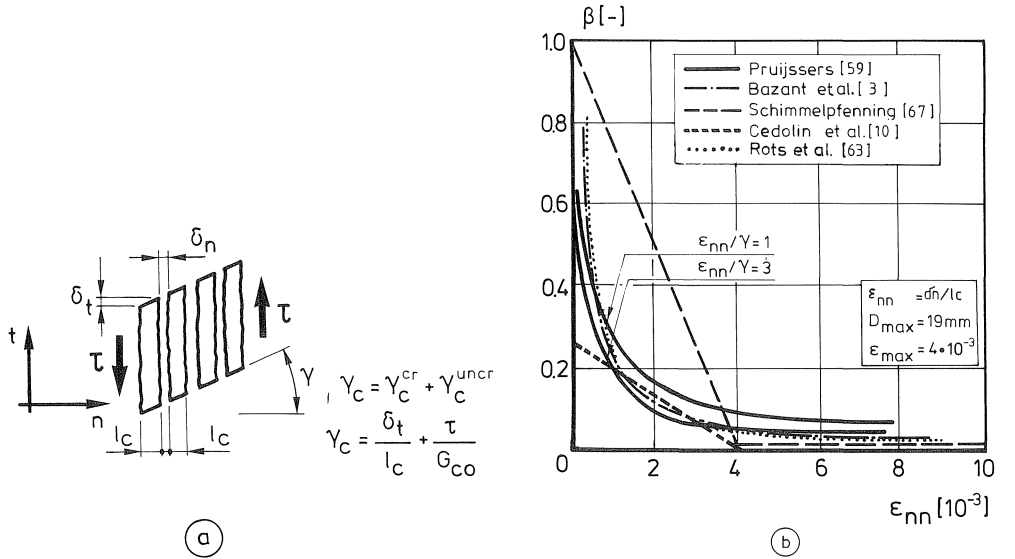
Fig. 2.13. (a) Shear deformation of a cracked panel; (b) shear retention factor β for plain concrete.

In the case of reinforcing bars crossing the crack, several empirical formulas for G_{cr} were reported, see for example in [10, 32, 35, 67]. Jimenez et al. [37] and Vecchio et al. [73] both found $G_{cr} = 0.05\text{--}0.07\,G_{co}$ for cracked reinforced concrete panels. Some formulas distinguish separately the mechanisms of aggregate interlock and dowel action. Pruijssers [59] used a decomposition of the concrete strains and based an expression on the model of Walraven [74]:

$$G_{cr} = \frac{1}{\alpha \varepsilon_{nn} + 1} \cdot G_{co} \quad [\text{N/mm}^2] \tag{2.6b}$$

where α is a function of γ/ε_{nn}, f_{cc} and D_{max}. See Fig. 2.13b. Vecchio et al. [73] later derived a similar formula. In practical terms, equation (2.6b) expresses the interaction between shear and normal stresses in the crack.

18

2.4 Concluding remarks

The *aggregate interlock* tests reveal that the crack-opening curves are significantly influenced by the concrete grade and the restraint "stiffness" of the crack plane. Cracks usually develop along the weak interfaces between the cement matrix and the particle surfaces. Different authors report that the *dowel* strength of statically loaded embedded bars is proportional to $d_b^2 \sqrt{f_{cyl} \cdot f_{sy}}$, provided that the concrete cover is sufficient, and it is reached at small transverse bar displacements. The maximum bending moment in the steel bar is assumed to be situated at $0.5-1.5 d_b$ away from the crack plane, for a minimum embedment length of $8 d_b$. Due to high bearing stresses under the bar the bond properties improve, so that only minor slip or even "perfect bond" may occur. The *combined* mechanism in cracked reinforced concrete has only been investigated for short-term circumstances. The crack-opening curves are hardly affected by the reinforcement ratio and less steep curves were observed for high-strength gravel and for light-weight concrete.

The theoretical models of Bažant et al. [3] and Walraven [74] have been successfully applied to the observed interlocking of cracked concrete subjected to monotonic shear loading. With respect to the static loading of cracked *reinforced* concrete, the two-phase model of Walraven has been combined with Rasmussen's formula, equation (2.2), see in [59]. The conclusion is that the previous research did not investigate the time-dependent stress-displacement relations for sustained shear loading conditions with crack widths $\delta_n < 0.25$ mm. This problem will be analyzed in chapters 3–5.

3 Experiments

3.1 Scope

The behaviour of cracked concrete subjected to sustained shear loading has been observed by means of two types of push-off specimen; 34 experiments on *reinforced* cracked concrete and 12 tests on *plain* cracked concrete.

This chapter deals with the most important aspects of the test set-up and the parameters chosen. A comprehensive overview is presented in [27]. Some additional detailed tests are treated in section 4.5.

3.2 Testing equipment and procedure

The shape of the push-off specimen chosen is almost identical to the type used by Mattock et al. [46] and Walraven [74] for static experiments. The dimensions of the crack area are 120×300 mm^2. See Figs. 3.1a-b.

The specimens were cast in steel moulds and were covered with plastic sheets immediately after casting. After two days they were demoulded and stored in a fog room (20 °C, 99% R.H.). Next, from an age of 22 days they were kept at 20 °C, 50% R.H.

For the *reinforced* crack, 8 mm diameter closed stirrups – each overlapped on the short side to ensure effective anchorage – intersected the crack plane perpendicularly. In the
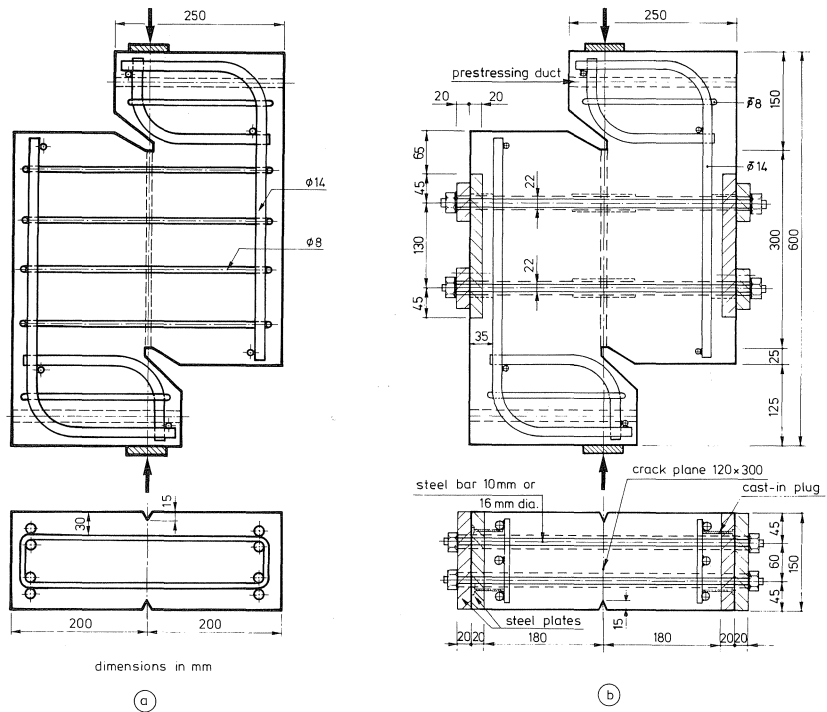
Fig. 3.1. Details of push-off specimens with a single crack for (a) reinforced concrete and (b) plain concrete restrained by rods.

other type of specimen (Fig. 3.1b) four 10 or 16 mm diameter rods passed through 22 mm diameter cylindrical holes. They were fastened between thick steel plates fixed on the short sides of the specimen. An almost constant restraint stiffness perpendicular to the crack plane was ensured. The rods were not expected to transfer any dowel force. The axial steel stress of each rod was measured by means of strain gauges. The initial steel stress was adjusted by bolts.

The cantilevers of each specimen were transversely post-tensioned to improve the introduction of the external shear force into the crack plane. Prior to the actual test each specimen was pre-cracked in a vertical position by means of a three point bending test (Figs. 3.2a–b). A steel knife was pushed into a V-shaped groove along the shear plane. Successively, the front and the rear sides of the specimen were split. At the top and bottom of the shear plane the crack widths were measured with 0.01 mm accuracy displacement transducers. Next, the specimen was placed centrally in a metal frame (Fig. 3.4). Prior to the long-term test, the desired shear loading level was applied step-wisely by a hydraulic jack, measured by a load cell installed under the specimen. An oil-accumulator was added to the hydraulic system to compensate for small pressure losses.

20
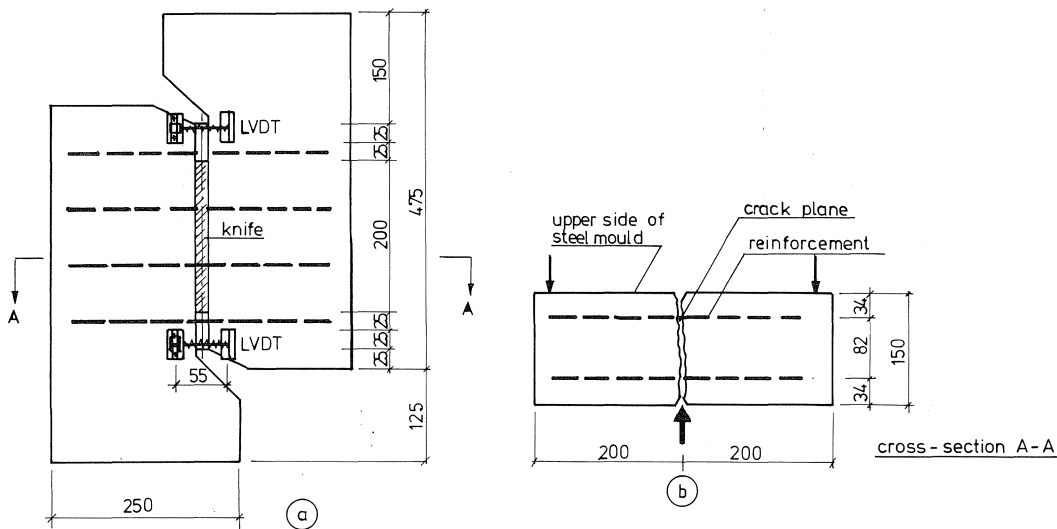
Fig. 3.2a–b. Details of the splitting procedure of the specimen.

The test period can be divided into four phases:
- *preparation* of the specimen. Steel reference points were fixed on the concrete and, after pre-cracking, the specimen was placed in the frame;
- *application* of the shear loading at a rate of $10–30 \cdot 10^{-3}$ N/mm^2 per sec.;
- *periodical* measurements under sustained loading of both the shear force and the crack displacements. After approximately 21 days the recordings were repeated weekly;
- *removal* of the sustained loading. Unloading occurred after at least 90 days of load application. The remaining crack displacements were periodically measured over a period of three weeks. Next, the static shear strength of the specimen was determined.

In chronological order the displacements of the crack were recorded in two ways (Figs. 3.3a–b):
- duration $t \leq 24$ hours: displacement transducers measured the crack width and the shear slip on both faces of the specimen;
- duration $t > 24$ hours: change to another measuring system due to the limited number of transducers permanently available for the complete test series. A hand-held measuring device accurate to 0.003 mm and with a built-in opto-electric displacement transducer was used here.

Experimental data handling by micro-computer was opted for. The measured displacements were corrected in view of the direct and the time-independent (creep, shrinkage) deformations of the concrete between the reference points near the crack.

21
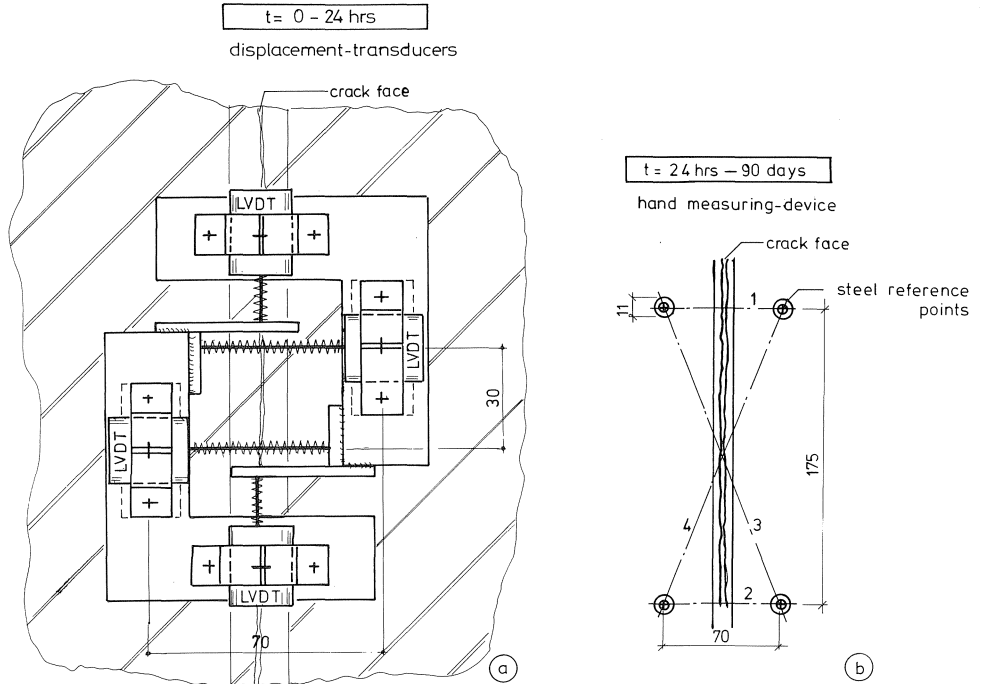
Fig. 3.3a–b. Front view of both measuring systems.

3.3 Experimental parameters

The experimental program comprises five parameters:

– *cube compressive* strength f_{cc}. Two different concrete mixes were used, both containing Portland cement type B (acc. to the Netherlands Standard; medium rapid hardening) and glacial river aggregates of 16 mm maximum size. The particle distribution was in accordance with Fuller, see appendix I. High-strength concrete was chosen in view of the application to offshore structures and to study the crack roughness. Average 28-day cube strengths were 51 and 70 N/mm² respectively;

– *restraint* of the crack plane. Either four restraint steel rods or 8 mm diameter embedded reinforcing bars were used. The reinforcement ratio was between 1.12% (4 stirrups) and 2.24% (8 stirrups);

– *initial crack width* δ_{no}. It was hardly possible to adjust the desired initial crack width accurately. During pre-cracking the crack width was about 0.10 mm and it reduced to 0.01–0.06 mm after removal of the knife;

– *steel grade* f_{sy} and *initial normal* compressive stress σ_{co} on the crack plane. Deformed steel bars were used with a yield strength of $f_{sy} = 460$ or 550 N/mm² (specific rib areas $f_R = 0.050$ and 0.059 respectively). The adjusted initial stress of the external rods corresponded to $\sigma_{co} = 1\text{–}2$ N/mm²;

1. flat hydraulic jack
2. ball joint
3. steel plates
4. prestressing steel
5. concrete specimen
6. tie rod
7. sliding layer
8. crack plane
9. load cell and socket joint
10. stirrup
11. add. reinforcement

Fig. 3.4. Front view of specimen and loading arrangement.
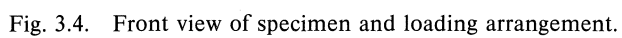
– *shear stress-level* τ/τ_u. The level was based on the static shear strength τ_u which is a calibration value (Figs. 3.5a–b). From 67 static tests on cracked reinforced concrete push-off specimens it was found that [75]:

$$\tau_u = \alpha \left(\varrho f_{sy} \right)^{\beta} \quad \text{provided that: } \tau_u \leq 0.26 f_{cc} \quad [\text{N/mm}^2] \tag{3.1a}$$

where $\alpha = 0.882 f_{cc}^{0.406}$ and $\beta = 0.159 f_{cc}^{0.303}$. The τ_u of cracked plain concrete for an initial crack width of 0.1 mm was given by [27]:

$$\tau_u = 1.647 \sigma_{co}^{0.427} \cdot f_{cc}^{0.321} \quad \text{provided that: } \tau_u \leq 0.26 f_{cc} \quad [\text{N/mm}^2] \tag{3.1b}$$
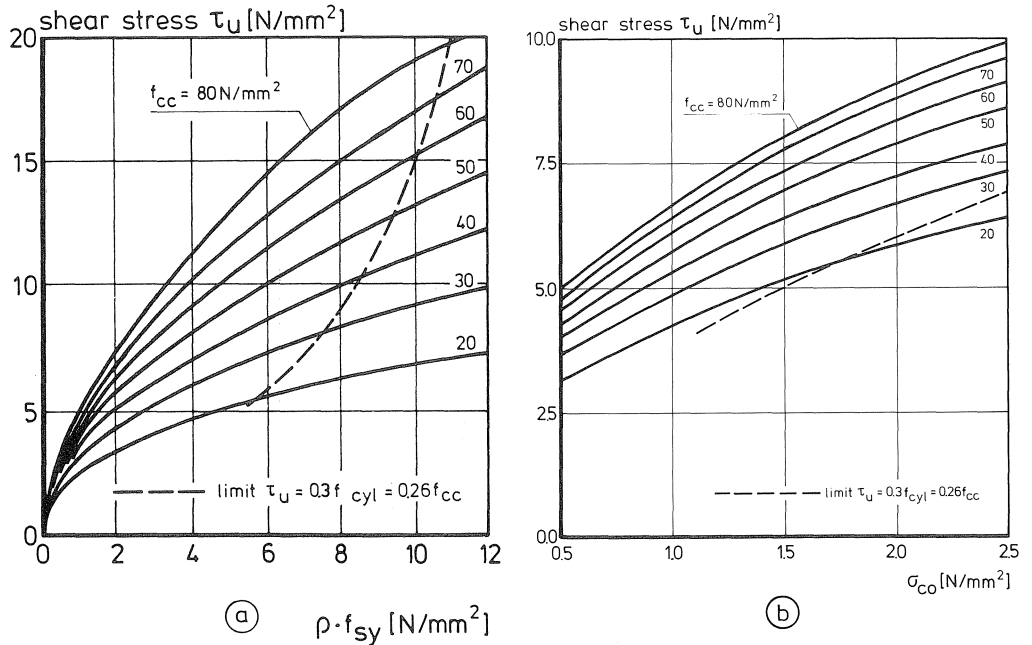
Fig. 3.5. Static shear strength τ_u for (a) cracked reinforced concrete and (b) cracked plain concrete push-off specimens.

The shear stress-levels used in the test series are relatively high compared with the serviceability state of structural applications. This was done in order to obtain crack displacements in a measurable range. For reinforced push-off specimens $\tau = 5.7$–11.5 N/mm^2, so that $\tau/\tau_u = 0.45$–0.89. For the plain concrete push-off specimens $\tau = 4.0$–6.5 N/mm^2 and $\tau/\tau_u = 0.49$–0.84. A survey of the complete test program is presented in Tables 3.1–3.2. Figs. 3.6a–b summarize the cube compressive strengths measured.

24

Table 3.1. Survey of the test program for reinforced concrete specimens

t_0 [days]	shear plane	mix*	f_{cc} [N/mm²]	ϱ** [%]	f_{sy} [N/mm²]	δ_{no} [mm]	τ/τ_u [–]
28	cr.	A 15	48–54	1.12–2.24	460 or 550	0.01–0.06	0.45–0.89
28	cr.	B 15	67–74	1.12–2.24	460 or 550	0.01–0.06	0.55–0.86
10	cr.	A 1	44	1.12	550	0.01	0.78
10	cr.	B 1	58	1.12	550	0.01	0.74
28	uncr.	A 1	50	1.68	550	–	–
28	uncr.	B 1	70	1.12	550	–	–

  * number of specimens
** 1.12% (4 stirrups), 1.68% (6) or 2.24% (8)

Table 3.2. Survey of the test program for plain concrete specimens

t_0 [days]	loading	mix*	$f_{cc}(t_0)$ [N/mm²]	d_b [mm]	σ_{co} [N/mm²]	δ_{no} [mm]	τ/τ_u [–]
29	stat.	A 1	56	10	2.5	0.02	–
28–65	stat.	B 3	65–75	10 or 16	0.4–1.1	0.01–0.03	–
28–79	sust.	A 5	49–58	10 or 16	0.9–2.0	0.01–0.02	0.49–0.80
28–35	sust.	B 3	64–73	10 or 16	1.0–2.0	0.02–0.03	0.74–0.84

* number of specimens
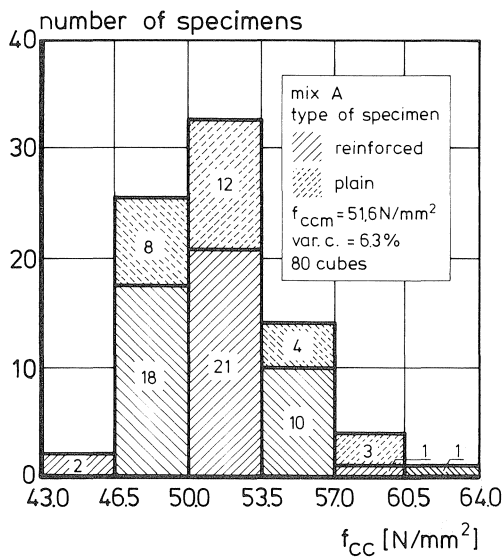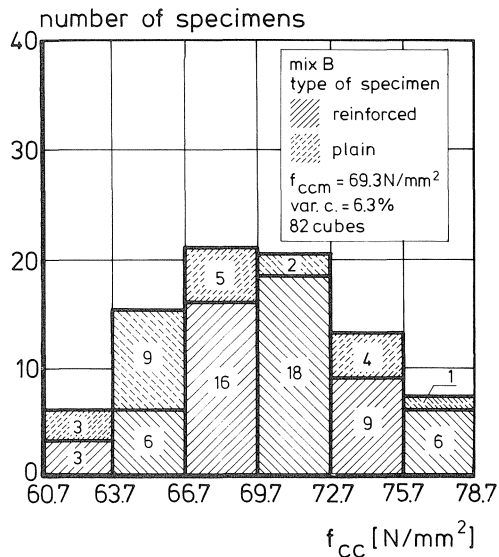
Fig. 3.6a–b. Distribution of the 28-day cube compressive strengths related to the reinforced and plain concrete push-off specimens.

4 Experimental results and parameter analysis

4.1 *Introduction*

Sections 4.2 and 4.3 present the most relevant results of the tests on cracked push-off specimens. Emphasis lies on the instantaneous and the time-dependent displacements parallel and perpendicular to the shear plane. Both sections end with a first analysis of the tests. The observed behaviour has been statistically determined as functions of the experimental parameters. The predicted long-term crack displacements are dealt with in section 4.4. In section 4.5 attention is paid to a few supplementary investigations. Comprehensive information is presented in appendix II.

4.2 *Tests on reinforced concrete specimens*

4.2.1 Displacement behaviour

The crack displacements δ_{nel} and δ_{tel} perpendicular and parallel to the crack surface respectively are related to the instant $t = 0$ h when the desired sustained shear loading has just been applied. The displacements were observed to increase by $\delta_{nc}(t)$ and $\delta_{tc}(t)$ as functions of the load duration t. This can be written as (see Figs. 4.1a–b):

$$t \geq 0 \text{ hrs: } \delta_n(t) = \delta_{nel} + \delta_{nc}(t) \quad [\text{mm}] \tag{4.1a}$$

$$t \geq 0 \text{ hrs: } \delta_t(t) = \delta_{tel} + \delta_{tc}(t) \quad [\text{mm}] \tag{4.1b}$$
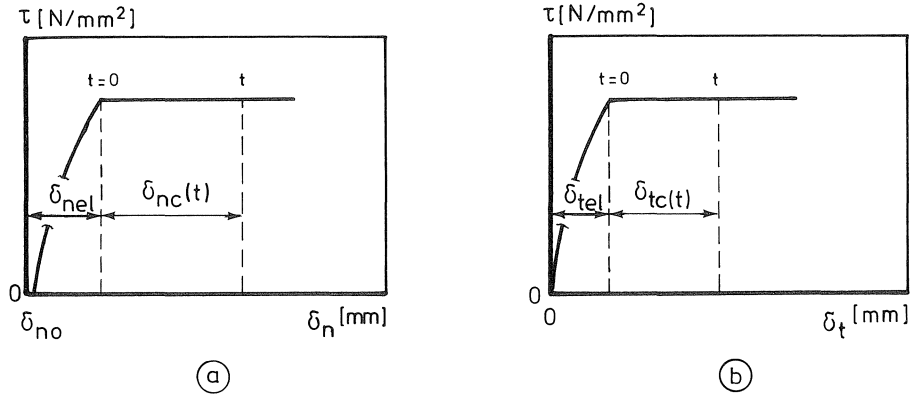
Fig. 4.1a–b. Definitions of instantaneous and incremental ("creep") displacements as functions of τ and t.

The displacements on the front (i.e. the upper side of the mould) are systematically 5–25% larger, probably due to the casting direction and method of compaction of the concrete. The developments of measured displacements during the load application are illustrated in Fig. 4.2 for one specimen: $\delta_{no} = 0.03$ mm; $\varrho = 1.12\%$; $f_{sy} = 550 \text{ N/mm}^2$ and $\tau/\tau_u = 0.77$.
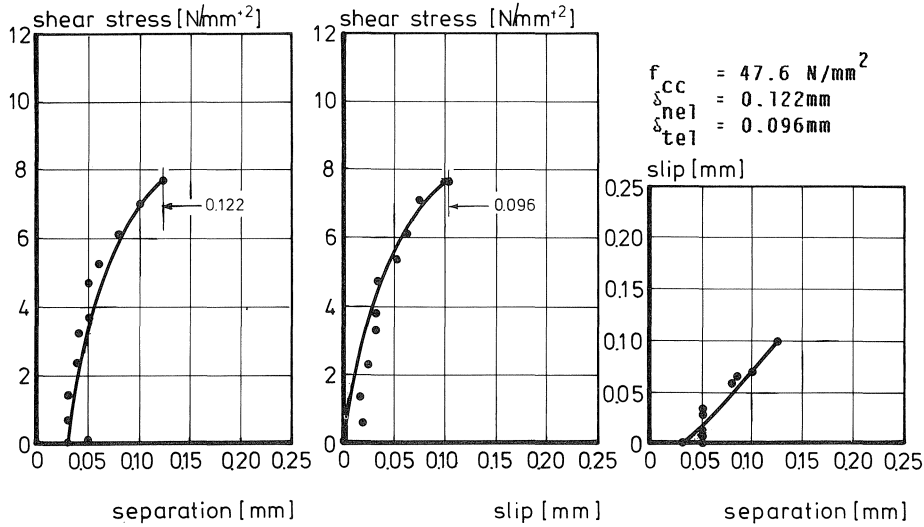
Fig. 4.2. Measured response on application of the shear load.

The measured time-dependent displacement increments of the above-mentioned specimen are presented in Fig. 4.3. The data refer to an application period of 90 days ($\cong$ 2150 hours). The regression curves and the associated statistical boundaries of the 90%-confidence areas are indicated.

On combining the instantaneous and the time-dependent increments according to equations (4.1a–b), the crack-opening paths are found, see appendix II.

4.2.2 Results of the parameter analysis

The displacement curves in section 4.2.1 have been calculated by non-linear regression analysis for various reasons:

- the time-dependent behaviour exhibits considerable scatter because the heterogeneity of the concrete gives rise to complicated time-dependent effects (shrinkage, creep, bond between concrete and steel). Furthermore, measurements are not fully reproductive as similar push-off specimens respond differently to "equal" parameter combinations;
- a statistical analysis provides a tool for an objective description;
- extrapolation to a longer sustaining period is done with more confidence;
- the influence of each parameter on the displacement response is quantified.

The time-dependent displacement curves have all been expressed by power-functions so that the measuring data should be logarithmically transformed. Generally this type of function can satisfactorily describe the creep deformations of plain concrete for short and long periods of observation [77]:

$$y = \alpha_1 + \alpha_2(x + \alpha_3)^{\alpha_4} \quad [-] \tag{4.2}$$

27
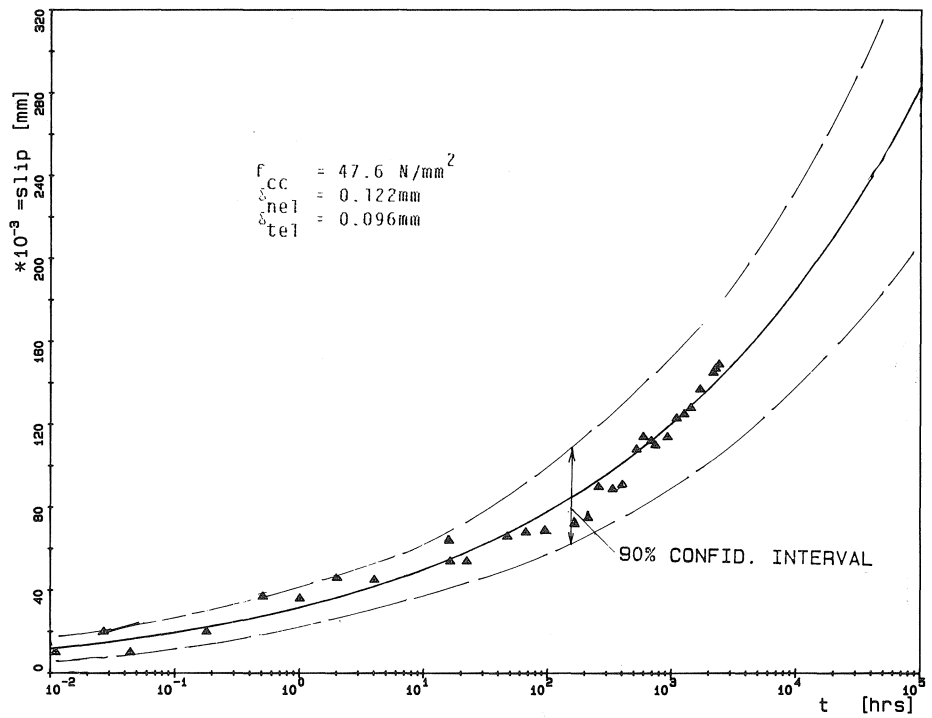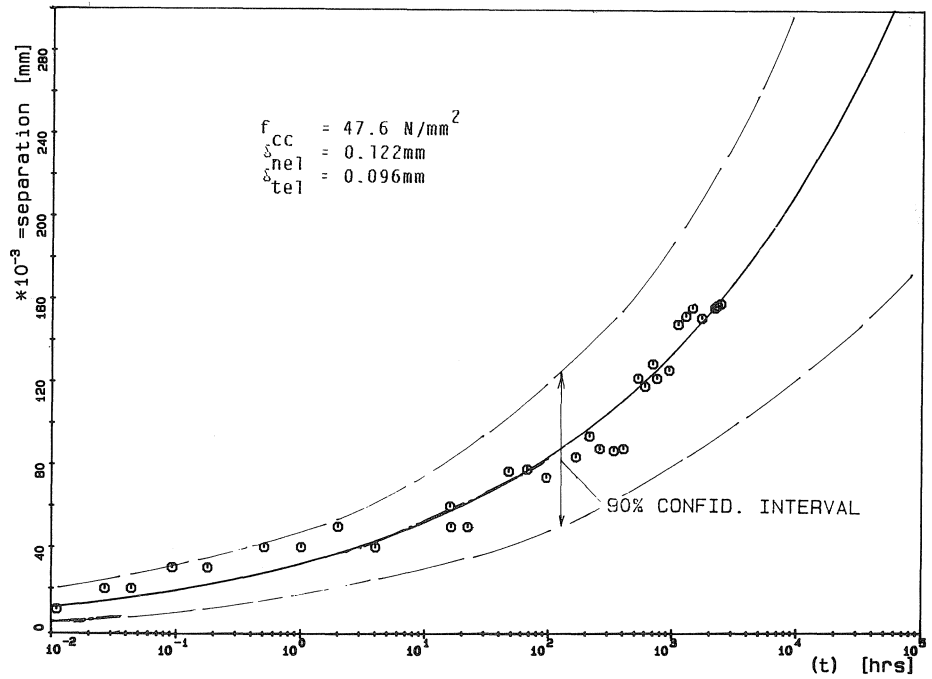
Fig. 4.3. Measured δ_{nc} and δ_{tc}-values; specimen no. 4.

in which $\alpha_1 - \alpha_4$ = regression coefficients. For each specimen equation (4.2) has been applied three times, with $x = t$, t, δ_n and $y = \delta_{nc}(t)$, $\delta_{tc}(t)$, δ_t respectively. The least square sum

$$\Sigma = \sum_{i=1}^{n} \left(y_i^{meas} - y_i^{regr} \right)^2$$

is minimized step-wise. The mean difference between an individual measurement and its regression value is defined as:

$$\bar{a} = \sqrt{\Sigma/n} \quad [mm] \tag{4.3}$$

where n denotes the number of observations. Theoretically $\bar{a}$ should be zero. From Figs. 4.4a–c it is concluded that $\bar{a}$ satisfactorily approximates the 0.005 mm error of the measured displacements. The values at the onset of the sustained test ($t = 0$ hrs; $\delta_{nc} = \delta_{tc} = 0$ mm and $\delta_t = 0$ mm for $\delta_n = \delta_{no}$) are also accurately described by means of equation (4.2).
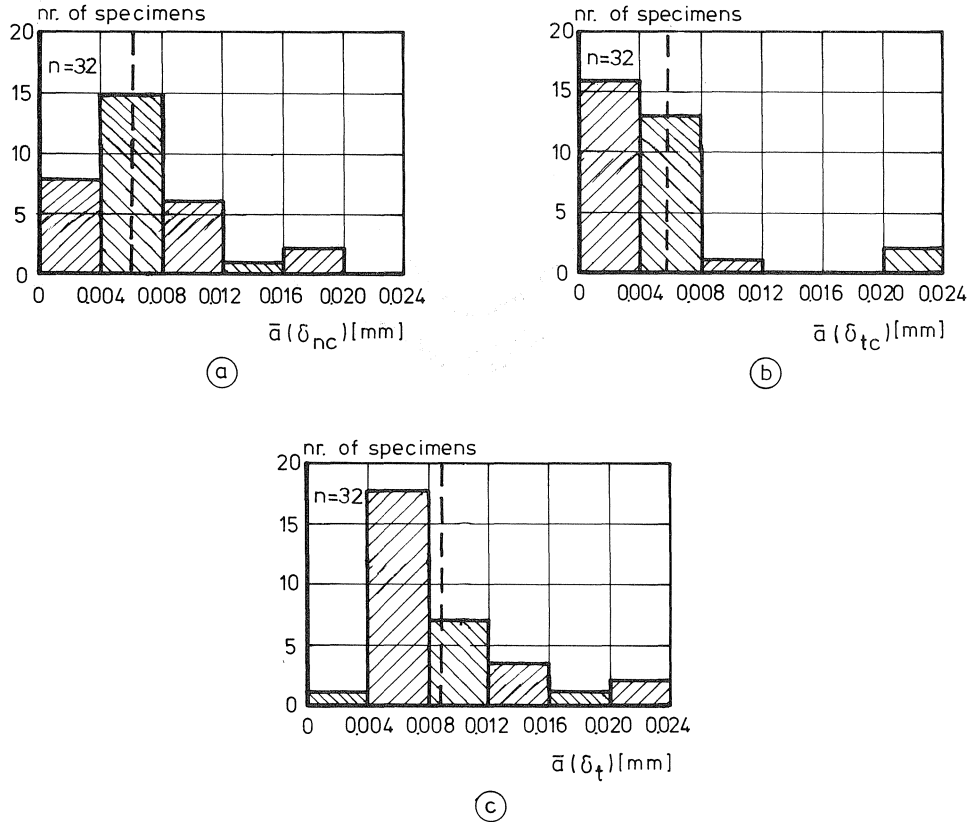
Fig. 4.4a–c. Distributions of $\bar{a}$ according to equation (4.3).

29

An extrapolation to a longer application period does not lead to a progressive change in the predicted displacements, see Fig. 4.5. If it exceeds 1500 hrs then the computed crack width increment δ_{nc} at $t = 10^5$ hrs tends to stabilize. The same is true for the parallel displacement increments. Thus, an observation period of at least three months will be sufficient.
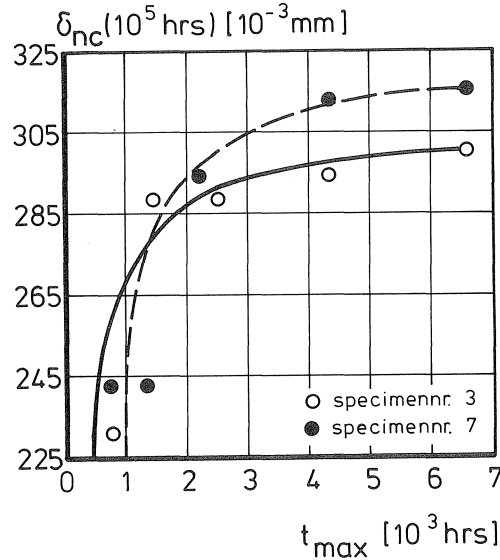
Fig. 4.5. Influence of the observation period t_{max} on the computed displacements according to equation (4.2) for $t = 10^5$ hrs.

Next, the test series was mathematically formulated in two steps:

Step 1. The calculation of unique τ-δ_n and τ-δ_t relations for monotonically increasing shear loading. Good agreement with the measurements was found if these relations are a linear combination of a power function and a reciprocal function;

Step 2. The object is to write the time-dependent displacement response as a function of f_{cc}, f_{sy}, δ_{no}, τ/τ_u. It was hard to find reliable functions for the regression coefficients $\alpha_1 - \alpha_4$ of equation (4.2). Thus an implicit method is required. This is illustrated here for the crack width increment $\delta_{nc}(t)$ in Fig. 4.6. Four prescribed values were proposed according to:

$$\delta_{nc}(t = 0 \text{ hrs}) = \alpha_1 + \alpha_2(\alpha_3)^{\alpha_4} = 0 \qquad \text{[mm]} \qquad (4.4a)$$

$$\delta_{nc}(t = 2000 \text{ hrs}) = \alpha_1 + \alpha_2(\alpha_3 + 2000)^{\alpha_4} = g_1 \qquad \text{[mm]} \qquad (4.4b)$$

$$d\delta_{nc}/dt(t = 100 \text{ hrs}) = \alpha_2\alpha_4(\alpha_3 + 100)^{\alpha_4 - 1} = g_2 \qquad \text{[mm/hrs]} \qquad (4.4c)$$

$$d\delta_{nc}/dt(t = 2000 \text{ hrs}) = \alpha_2\alpha_4(\alpha_3 + 2000)^{\alpha_4 - 1} = g_3 \qquad \text{[mm/hrs]} \qquad (4.4d)$$

Next, statistically-based functions were determined for $g_1 - g_3$ which all express a
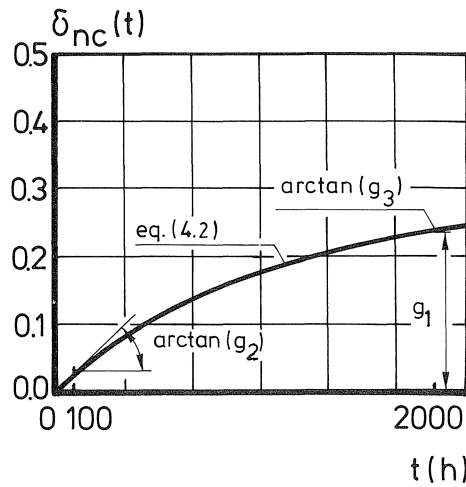
Fig. 4.6. Prescribed values indicated for the δ_{nc}-t relation.

proper formulation of the prescribed values. After they are known for each parameter combination, the (new) coefficients α_1-α_4 are iteratively solved from the set of equations (4.4a–d). To derive the δ_t-δ_n and δ_{tc}-t relations, the procedure is as outlined above for $\delta_{nc}(t)$. The choice of the magnitudes of the parameters which are introduced into the calculations is confined to the experimental range. Table 4.1 shows that the prescribed values given by the empirical formulae agree closely with the measurements.

Table 4.1. Overview of the computed and "measured" prescribed values

relation	prescribed value	no. of tests	$\bar{x}$*	v.c.**
$\tau - \delta_n$ and $\tau - \delta_t$	τ_u	67	0.99	0.07
	$\tau(\delta_n = 0.1 \text{ mm})$	31	1.04	0.20
	$\tau(\delta_t = 0.1 \text{ mm})$	31	1.06	0.12
	$\delta_{n\,top}$	17	0.94	0.17
	$\delta_{t\,top}$	17	0.95	0.23
$\delta_{nc}(t)$	g_1, g_2 and g_3	24	1.03	0.27
$\delta_{tc}(t)$	g_4, g_5 and g_6	24	1.06	0.23
$\delta_t(\delta_n)$	g_7, g_8 and g_9	24	1.00	0.20

 * $\bar{x}$ = calc./meas. value
** coefficient of variation $= s(\bar{x})/\bar{x}$

Note that the choice of $\bar{x}$ as a measure of comparison may be somewhat arbitrary. Special attention should be paid to the crack-opening curve which relates to the full duration of the test (step 1 and step 2). As an advantage, this curve has a relatively large statistical reliability. According to Fig. 4.7 there are two ways of projecting the time axis. For an arbitrary point of time $t = t_i > 0$ hrs, the points A and B will in general not coincide, i.e. there is no unique δ_n-δ_t-t relation. The final position is located midway at the most probable point D. The displacement shifts are attributed to scatter which is

Fig. 4.7. Computational method used to find a unique crack-opening curve.

inherent to (time-dependent) phenomena in concrete [14, 51]. The width of the 90% confidence interval of the crack-opening curve determines the permissible maximum shift (or: the sustaining period t_{max}). It was found from 32 tests that:

$$\bar{t}_{max} = 10^{5.70} \text{ hrs} \cong 57.2 \quad \text{and} \quad t_{max, 10\%} \cong 8.3 \quad \text{[years]} \tag{4.5}$$

All these periods are lower-boundary values due to the constant width of the 90% confidence interval assumed in the calculations.

Figs. 4.8a–b and 4.9a–b show some response curves which have been obtained by the mathematical method discussed before. The discontinuity in the time-displacement curves relates to the increments $\delta(t = 0.1 \text{ hrs}) - \delta_{el}$ that are larger for higher τ/τ_u-ratios. Some other conclusions are drawn:

– the τ-δ_n curves exhibit a displacement increase between equidistant points (equal decimal ratios) of time for higher shear stress values;

– for $f_{cc} = 51$ and 70 N/mm^2 the ratio δ_{nc}/δ_{nel} ranges between approximately 0.8–1.1 and 0.4–0.8 respectively if $\tau/\tau_u = 0.90$ and $t = 10^3$ hrs.

The latter conclusion denotes the considerable influence of the concrete compressive strength on the crack displacements. It is known that the values adopted for the experimental parameters are an approximation of the actual values. Differences arise as a result of a limited measuring accuracy (adjustment of τ and δ_{no}), variations in material properties (ϱ, f_{sy}, inhomogeneity of concrete) and environmental changes (T and R.H.). Since τ_u depends on f_{cc} – equation (3.1a) – the actual stress-level may deviate from the adjusted level. This phenomenon is shown in Fig. 4.10 for mix B.
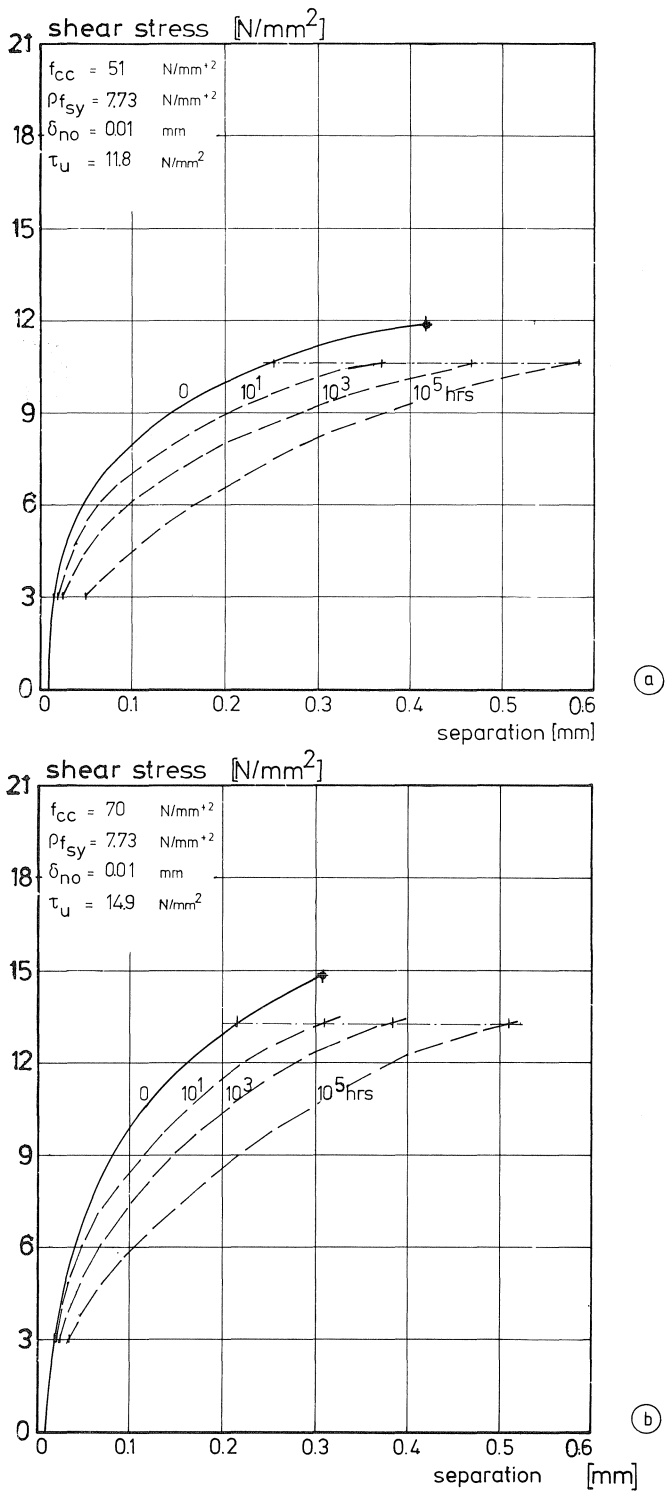
32

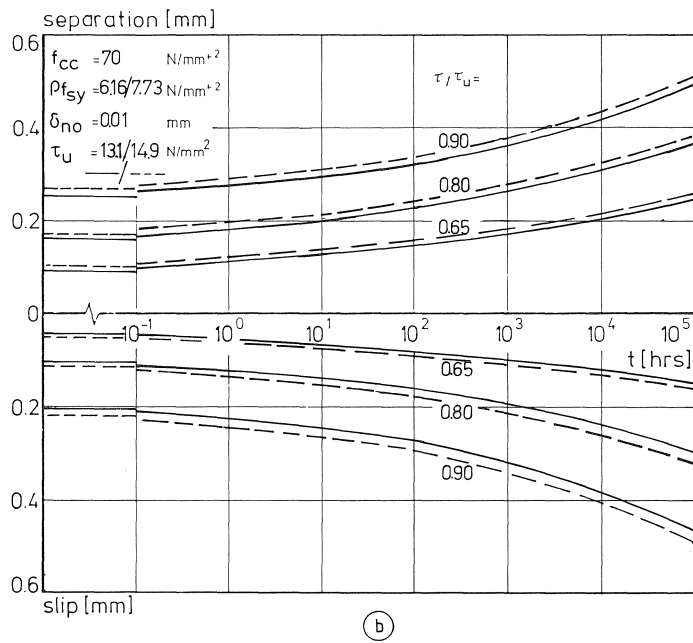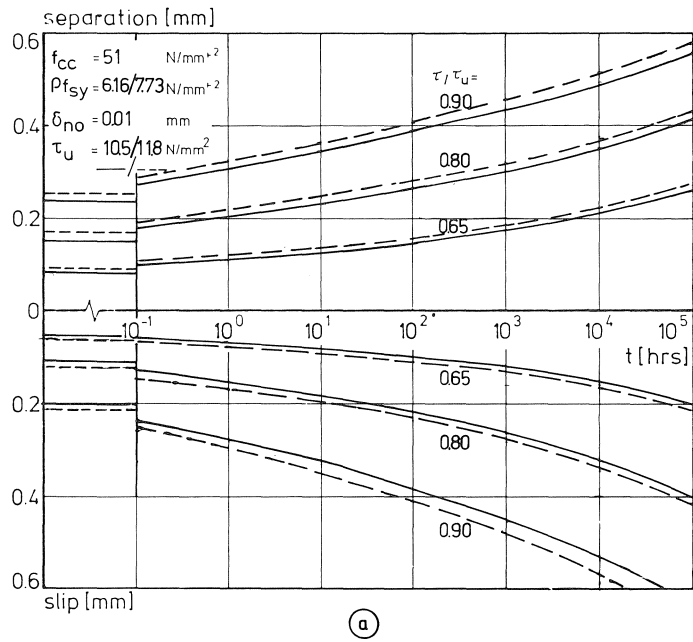Fig. 4.8. Computed τ-δ_n relations for (a) mix A and (b) mix B.

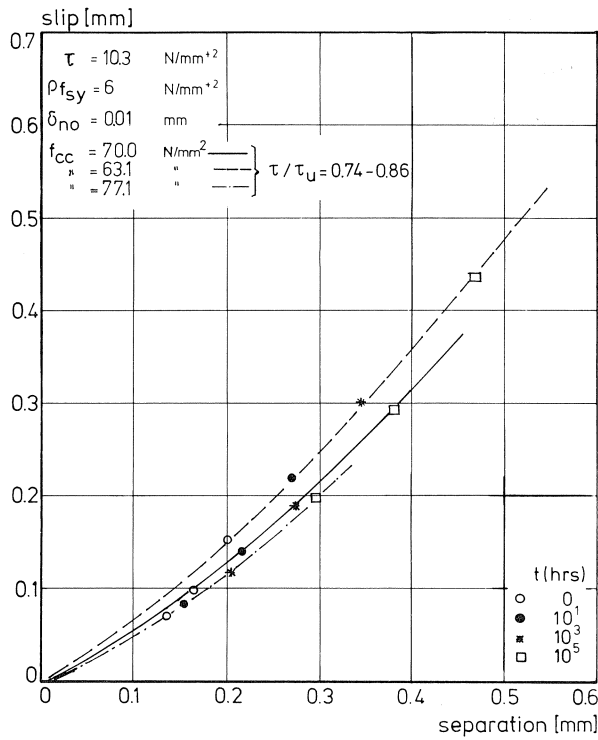Fig. 4.9a–b.   Identical to Fig. 4.8 for the displacement-time relations.

Fig. 4.10. Variation of f_{cc}: characteristic (5%, 95%) and mean (50%) concrete strengths based on a normal distribution.
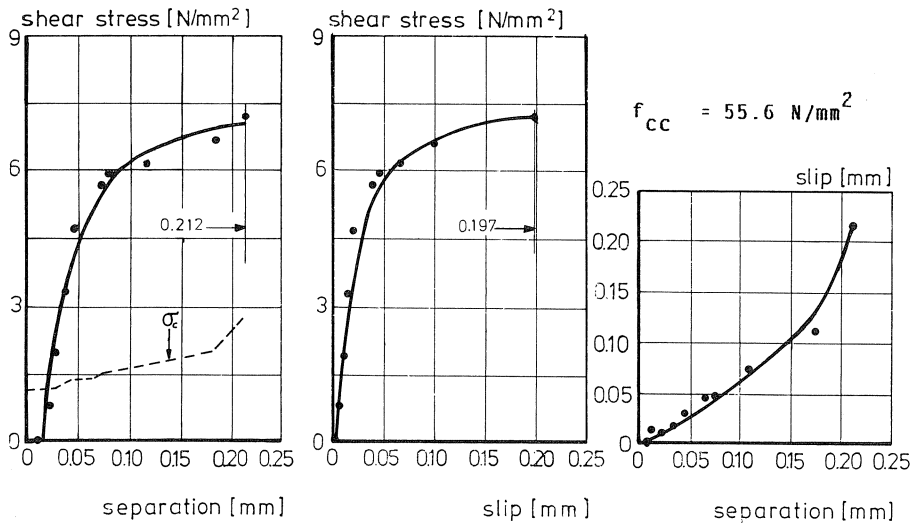

Fig. 4.11. Measured response on application of the shear load.

4.3 *Tests on plain concrete specimens*

4.3.1 Displacement behaviour

Most observations agree qualitatively with test results presented in section 4.2. The instantaneous crack displacements were now also systematically larger on the front sides of the specimens. Fig. 4.11 shows the result of one static push-off test [27]; $\sigma_{co} = 1.1$ N/mm²; $\delta_{no} = 0.1$ mm and $d_b = 16$ mm. The measured normal compressive stress on the concrete shear plane is indicated. The measured τ_u-values differed by less than 9% from equation (3.1b). The time-dependent crack-opening curves are based on a statistical treatment of the recoreded displacements, see appendix II.

The initial compressive stress σ_{co} on the crack surface corresponds to the initial crack width of the unloaded specimens. On application of the shear loading, the displacements of the crack-faces will increase. In order to maintain equilibrium, the restraint bars must be able to develop a sufficiently large increase of σ_c. Two final remarks should be made:

- the initial normal *restraint stiffness* $\alpha = \mathrm{d}\sigma_c/\mathrm{d}\delta_n$ of the crack plane is approximated on the assumption that the axial bar elongation is proportional to the crack width increase. The experimentally found mean α-values of each rod diameter agree reasonably with the calculations;
- after $t = 50$–250 hrs the normal stress sometimes *tended to drop* as a function of the crack widths. Particularly the drying shrinkage of the concrete surrounding the restraint rods may contribute to this phenomenon. Shrinkage usually became evident a few days after the wet push-off specimens were placed in the laboratory at 20 °C, 50% R.H.

4.3.2 Results of the parameter analysis

Formulae according to equation (4.2) have been statistically calculated for each sustained shear test performed. It was confirmed that the *mean* difference between the measured and computed values was smaller than the measuring accuracy. Simple formulae have been derived for δ_{nel} and δ_{tel}, which closely fit to the test data. An example is shown in Fig. 4.12. The time-dependent behaviour was simulated by means of an implicit calculation method, see also section 4.2.2. According to Table 4.2 the results reasonably approximated the test data, especially for the crack-opening curves. The computational results display a relatively high scatter, particularly due to the small number of tests performed.

One computational result is presented in Fig. 4.13. The calculations are executed for the concrete compressive strength related to the *average* concrete age at the onset of the static and sustained shear tests:

$$\text{mix A: } \bar{t}_0 = 46 \text{ days: } f_{ccm} = 55.2 \text{ N/mm}^2 \tag{4.6a}$$

$$\text{mix B: } \bar{t}_0 = 38 \text{ days: } f_{ccm} = 69.1 \text{ N/mm}^2 \tag{4.6b}$$

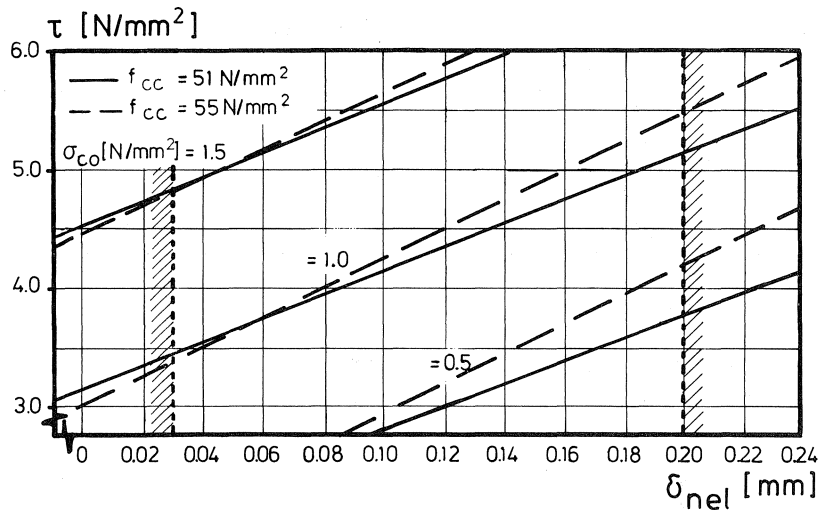For a constant shear stress, the lower the total time-dependent displacements, the

36

Fig. 4.12. Calculated development of δ_{nel} as a function of the shear stress and the concrete grade.
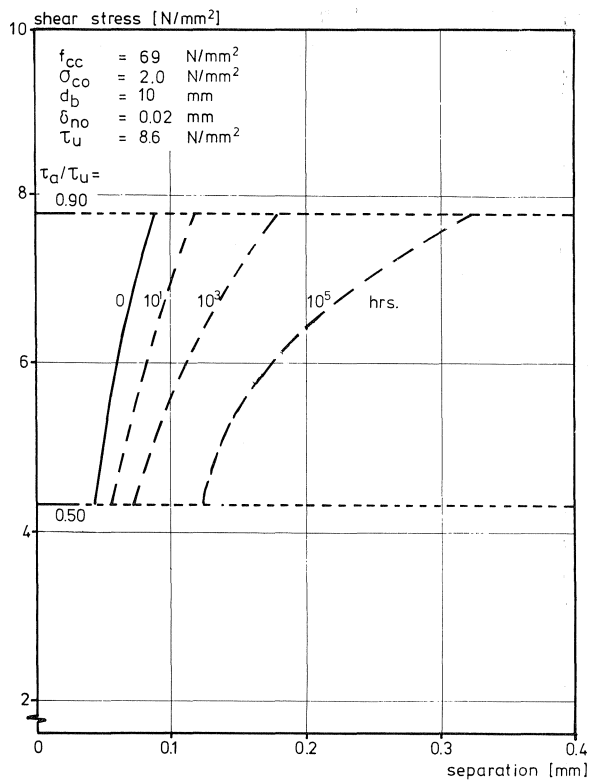

Fig. 4.13. The τ_a-δ_n relations with $d_b = 10$ mm, computed for mix B.

37

Table 4.2. Comparative overview of the computational results

relation	prescribed value	no. of tests	$\bar{x}$*	v.c.**
static	δ_{nel}	10	0.88	0.18
behaviour	δ_{tel}	10	0.80	0.27
$\delta_{\text{nc}}(t)$	g_1-g_3	8	1.04	0.22
$\delta_{\text{tc}}(t)$	g_4-g_6	8	0.93	0.15
$\delta_{\text{t}}(\delta_{\text{n}})$	g_7-g_9	8	0.95	0.12

  * $\bar{x}$ = meas./calc.
  ** coefficient of variation = $s(\bar{x})/\bar{x}$

higher the concrete grade. No significant influence of the initial crack width was found so that the mean value $\delta_{\text{no}} = 0.02$ mm is applied.

4.4 Long-term crack displacements

Table 4.3 presents the extrapolated values of crack width and parallel displacement for a loading period of $t = 10^5$ hrs $\cong 11.4$ years. It can be generally concluded from the results for $\delta_{\text{no}} = 0.01-0.05$ mm that:
- the displacements of the reinforced concrete push-off specimens are relatively small compared with those of cracked plain concrete specimens;
- at low shear stress-levels the cracks display $\delta_{\text{n}} > \delta_{\text{t}}$. The opposite conclusion applies to higher levels $\tau/\tau_{\text{u}} \approx 0.80$;
- in the case of a reinforced concrete crack, δ_{n} and δ_{t} are smaller than 0.20 mm for $\tau/\tau_{\text{u}} \leq 0.50$. This crack width limit corresponds to permissible values in the case of a fairly aggressive environment [66].

Table 4.3. Predicted displacements of a crack in reinforced (r) or plain (p) concrete subjected to a sustained shear loading; $t = 10^5$ hrs

crack	τ/τ_{u} [–]	τ [N/mm^2]	f_{cc} [N/mm^2]	δ_{n} [mm]	δ_{t} [mm]
r*	0.5	3.0– 4.6	30	0.13–0.16	0.12–0.15
	0.3	2.5– 4.4	51	0.04–0.09	0.04–0.07
	0.3	3.1– 5.8	70	0.03–0.08	0.03–0.05
r	0.8	4.8– 7.4	30	0.35–0.45	0.47–0.54
	0.8	6.7–11.7	51	0.37–0.45	0.38–0.44
	0.8	8.3–15.5	70	0.35–0.43	0.28–0.36
p**	0.8	4.8– 6.4	55	0.24–0.32	0.18–0.35
	0.8	5.3– 7.1	70	0.20–0.30	0.16–0.40

  * for $\varrho f_{\text{sy}} = 4-12$ N/mm^2
  ** for $\sigma_{\text{co}} = 1-2$ N/mm^2 and $d_{\text{b}} = 10-16$ mm

The results have also been expressed by means of a "creep" coefficient φ_{n} (and φ_{t}) which is defined according to [25, 27]:

$$\delta_{\text{n}}(t) = \delta_{\text{nel}} + \delta_{\text{nc}}(t) = \delta_{\text{nel}}(1 + \varphi_{\text{n}}(t)) \quad \text{[mm]} \tag{4.7}$$

From the analyses of φ-values and their time-dependent developments, a few conclusions can be drawn:

- after a sustained loading period of 10^5 hrs no final values are attained;
- the values display non-linearity (Fig. 4.14) with respect to τ/τ_u and f_{cc};
- φ_t-values are systematically larger than φ_n-values; 30–55% at $t = 10^5$ hrs and these differences increase with decrease in the concrete grade. A first reason is that $\delta_{tel} < \delta_{nel}$ for displacements smaller than about 0.20 mm. Moreover, in general $\delta_{tc} > \delta_{nc}$. Consequently, the crack-opening curves become steeper for a longer application period.
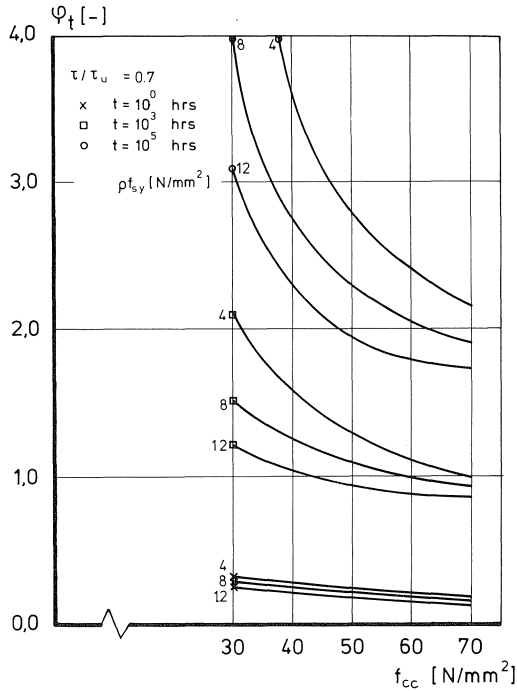
Fig. 4.14. Development of $\varphi_t(t)$ for cracked concrete [25], with $\delta_{no} = 0.01$–0.02 mm and τ_u according to equation (3.1a).

4.5 Additional tests

The response of the combined shear transfer mechanism strongly depends on the roughness of the shear plane and on the restraint stiffness of the reinforcing bars which cross the crack. For a deeper understanding, supplementary research was carried out on three specific subjects:

a. Crack initiation of the concrete
The percentage of fractured particles in the shear plane was counted for ten pre-loaded

specimens of the type shown in Fig. 3.1b. The mean ratios A_{agg}/A_c are low, approx. 23.3% (mix A) and 25.5% (mix B) of the concrete volume [27]. It is concluded that crack initiation of both types of concrete does not differ significantly.

b. *Strain gauge measurements*

Close to the crack plane the concrete and the steel bar cooperate in resisting the bending moment. This mechanism is due to good bond properties especially on the actual part of the bar supported by concrete. As a result the neutral axis of the bar is expected to shift within a length of 1–2 times the bar diameter (Fig. 4.15).
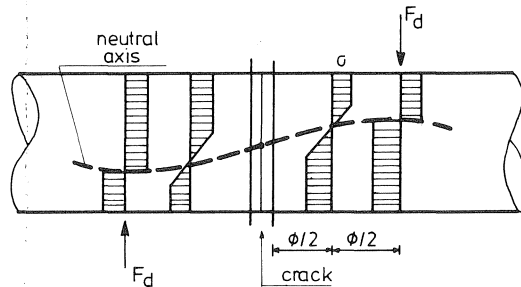
Fig. 4.15.   Assumed steel yielding of an embedded steel bar [27, 59].

Static and sustained tests were conducted on cracked reinforced push-off specimens of the type shown in Fig. 3.1a. The axial strain of the steel bars (8 or 12 mm diameter, $\varrho = 1.12\%$) was measured locally by means of bolt gauges (working length 8 × 1 mm) cemented in the cross-section area of the bar and fastened with epoxy resin. The method chosen prevented any change in the bond characteristics of the reinforcement used. See also Figs. 4.16a–b. The theoretical analyses are elaborated in chapter 5.

c. *Microscopic observations*

The dowel mechanism is assumed to cause localized plastic deformation of the steel crystals close to the crack plane of the push-off specimen. This plastic deformation of the steel was examined under a microscope (magnification 500 times). After the pushing-off of the specimen, the concrete of one half of the element was carefully removed. During the observations the approximate orientation and yielding of the steel crystals were recorded for 14 specimens. Nearly 70% of the selected data indicated localized orientation of the crystals, which supports the assumption of a local shift of the neutral axis [27, 59]. The results also revealed a point of contra-flexure in the bar.

Fig. 4.16. (a) Close-up of one bolt gauge and (b) measured restraint compressive stress $\sigma_c = \varrho \cdot \sigma_s$.

4.6 Discussion of results

Chapter 4 discusses the recorded time-dependent displacement behaviour of a single crack in concrete subjected to sustained shear loading. The crack widths observed were usually restricted to $\delta_n < 0.25$ mm, which was the original intention of the research. In none of the long-term tests shear failure occurred. It was difficult to distinguish the effect of each experimental parameter. Therefore, an implicit calculation method was developed resulting in unique empirical relationships which objectively and satisfactorily describe the specimen's response. The results revealed that the displacement response is highly non-linear with respect to the shear stress-level and the concrete grade. The cracked plain concrete restrained by steel rods displayed relatively small instantaneous crack widths.

41

However, the "creep" coefficients of the *plain* concrete with respect to δ_n and δ_t were markedly in excess of those of the *reinforced* concrete specimens. An extrapolation of the sustained loading period did not yield final displacement values. The static shear strength was hardly affected by the load history of the specimens [75]. The final section of this chapter provides some detailed investigations on the contribution of dowel action to the complete shear transfer mechanism. This information supports a fundamental approach which will be dealt with in chapter 5.

5 Theoretical analysis of shear transfer

5.1 *Introduction*

This chapter deals with a theoretical approximation of the transfer mechanism across a crack in reinforced concrete subjected to a constant shear loading. The shear transfer across a single crack in *plain* concrete is satisfactorily described for static loading by means of Walraven's two-phase model [74], as pointed out in section 2.3. With regard to a crack in *reinforced* concrete, dowel action is another transfer mechanism which has so far only been studied for static loading conditions, see section 2.2.

Two specific subjects relate to the modelling of time-dependent shear transfer across a crack in concrete [27]:

– the time-dependent deformation of matrix material, especially for multi-axial loading conditions, see in [30, 42];
– the sustained bond behaviour of embedded bars which partly governs the time-dependent crack-widening, see for example in [62].

Section 5.2 outlines the basics of an existing model which was developed for a single reinforced crack subjected to a monotonic shear loading. Next, this theory is extended to the sustained loading case in sections 5.3–5.6.

5.2 *Shear transfer model – monotonic loading*

The *aggregate interlock* model formulated by Walraven [74], see section 2.3, describes the stress-displacement relations of a plane crack. As the crack opens and slides, the total contact areas $A_x = \Sigma a_x$ and $A_y = \Sigma a_y$ of the stiff granular particles gradually increase because of plastic deformation of matrix material as illustrated in Fig. 5.1a. As the shear slip develops, an increasing number of the aggregates come into contact with the matrix material. The crack-opening path is bounded by a minimum slope $d\delta_t/d\delta_n$ for each combination of displacements, see Fig. 5.1b. This is analogous to a sufficient restraint of the crack halves [59].

Dowel action of reinforcing bars is the second mechanism of shear transfer in a crack. Pruijssers [59] transformed Rasmussen's formula equation (2.2) and he found that:

$$V_{du} = 1.35[\sqrt{(\varepsilon')^2 + 1} - \varepsilon'] \cdot d_b^2 \sqrt{f_{ccm} f_{sy}} \quad [\text{N}] \tag{5.1}$$

where $\varepsilon' = e\sqrt{f_{ccm}/f_{sy}}/d_b$. Now V_{du} is increased by 10–12% provided that $f_{cyl} = 0.85 f_{cc}$; $e \leq 0.015 d_b$ and $f_{cyl}/f_{sy} = 0.05$–0.10. Rigid bond (no slip at the interface) is adopted on
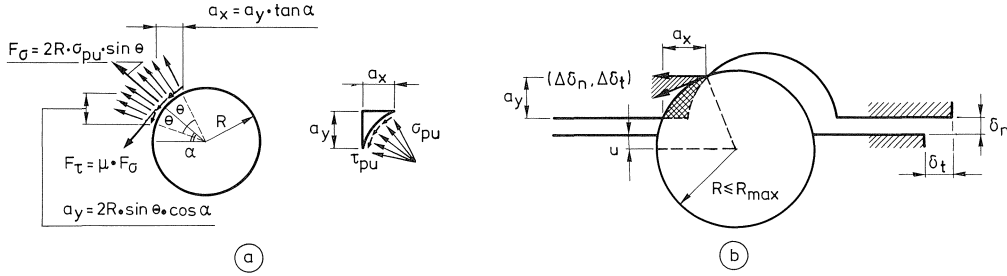
Fig. 5.1. (a) Contact areas and deformed matrix and (b) possible crack-opening directions (shaded area).

the supported part of the dowel close to the crack plane. High bond stresses are induced by local multiaxial confinement of the concrete. The analysis of previous dowel test results revealed a shift of the neutral axis towards the supported side of the bar. The cooperation of the embedded bar and the surrounding concrete causes a 34% increase in the plastic bending moment of the bar at dowel failure, see Figs. 5.2a–b.

$$M_{\mathrm{pl}} = V_{\mathrm{du}}(e + ax) = 0.22d_{\mathrm{b}}^3 \cdot f_{\mathrm{sy}} \quad [\mathrm{Nmm}] \tag{5.2}$$
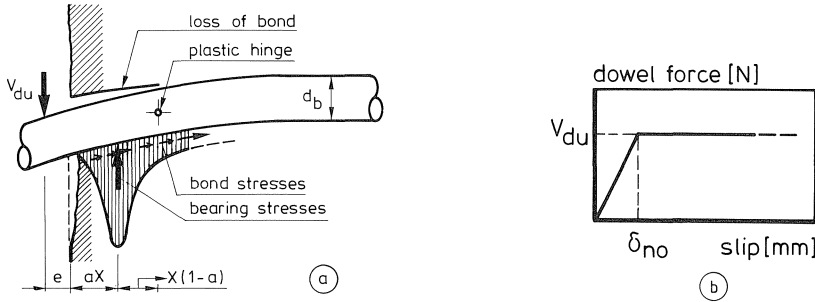
Fig. 5.2. Assumed dowel mechanism according to Pruijssers [59] and (b) assumed formalistic dowel model.

The precise distribution of bond stresses parallel to the bar axis is not considered in view of the small length of $x \approx d_{\mathrm{b}}$ in Fig. 5.2a.

Fig. 5.2b indicates that the dowel strength is reached if the crack halves slide parallel over $\delta_{\mathrm{t}} \geq$ the initial crack width δ_{no} with a proposed minimum of 0.10 mm for δ_{t}. Here the initial crack width refers to the instant when the shear load has just been applied. The actual dowel load may be reduced due to an interaction of axial and shear stresses. This is formulated empirically by means of a yield criterion [49, 68]:

$$V_{\mathrm{d}} = \gamma_{\mathrm{d}} V_{\mathrm{du}} = \sqrt{[1 - (\sigma_{\mathrm{s}}/f_{\mathrm{sy}})^2]} * V_{\mathrm{du}} \quad (\gamma_{\mathrm{d}} \leq 1) \quad [\mathrm{N}] \tag{5.3}$$

The total stresses to be transferred in a reinforced crack are defined as:

$$\tau = \tau_{\mathrm{a}} + \gamma_{\mathrm{d}}\tau_{\mathrm{d}} \quad [\mathrm{N/mm}^2] \tag{5.4a}$$

$$\sigma = \sigma_{\mathrm{a}} \quad\quad [\mathrm{N/mm}^2] \tag{5.4b}$$

43

where $\tau_d = V_d/A_c$. On combining equations (2.5a–c) and (5.1–5.4), the result for $d_b = 8$ mm and $A_c = 120 \times 300$ mm^2 is that:

$$\tau = \sigma_{pu}(A_y + \mu A_x) + 5.40\gamma_d * \varrho\alpha * \sqrt{(f_{ccm} f_{sy})}/\pi \quad [\text{N/mm}^2] \tag{5.5a}$$

$$\sigma = \sigma_{pu}(A_x - \mu A_y) \quad [\text{N/mm}^2] \tag{5.5b}$$

where $\sigma_{pu} = 6.39 f_{ccm}^{0.56}$; $\mu = 0.40$, $\alpha = \sqrt{(\varepsilon')^2 + 1} - \varepsilon'$ and $\varrho = n\pi d_b^2/(4A_c)$. Pruijssers [59] proposed multiplying *both* interlock stresses by $\gamma_a < 1$ in case of a low reinforcement ratio. This adaptation is not considered in this report. Equations (5.5a–b) denote that the stresses σ, τ are uniquely related to δ_n, δ_t. If the plastic hinges have fully developed in the dowel, then the crack-opening is dominated by the rough-crack model of Walraven, because the dowel bars no longer affect the compatibility of the crack. The computational procedure is summarized in appendix III.

At the onset of the shear test – for small shear slips $\delta_t \leq 0.10$ mm – the bearing stresses under the dowel are relatively low. At that stage the model of a beam on elastic foundation (see section 2.2.2) may be applied:

$$\tau_d = \tau_{du}\left(\frac{\delta_t}{0.10 + \delta_{t,e}}\right)^{1/3} \leq \tau_{du} \quad [\text{N/mm}^2] \tag{5.6a}$$

where:

$$\delta_{t,e} = 1.31 * 10^{-7} * d_b^{0.60} * (f_{ccm} f_{sy})^{1.20} \quad [\text{mm}] \tag{5.6b}$$

The crack-opening curve is now represented by an empirical relationship:

$$\delta_t = (\delta_{no} f_{sy}/2f_{ccm})^{1/2} * (\delta_n - \delta_{no})^{2/3} \quad [\text{mm}] \tag{5.6c}$$

5.3 *Shear transfer model – sustained loading*

The existing theoretical model of the monotonic loading case is now adapted to long-term loading conditions, according to:

$$\tau(t) = \bar{\tau} = \text{constant} \quad [\text{N/mm}^2] \tag{5.7}$$

where t denotes the duration of load application. The formulae presented in the preceding section are changed in three successive phases:

a. *Modification of the stress-displacement relations equations (5.5a–b)*
With respect to the short-term behaviour of the concrete interface, the interlock stresses σ_a, τ_a are proportional to $f_{ccm}^{0.56}$ and the dowel strength τ_{du} is directly related to $f_{ccm}^{0.50}$. These two exponents lie within the same range so that a change in the concrete strength approximately affects both transfer mechanisms similarly. Special attention should be paid to high-strength concrete in view of the increasing brittleness expressed by the ratio σ_{pu}/f_{cc}. The shear plane of the crack was extensively observed after the static push-off tests, see section 4.5. However, the high-strength concrete used for the tests – mix B with $f_{ccm} \approx 70$ N/mm^2 – revealed no systematic difference as regards the percentage of fractured particles.

44

Consequently, the rough crack model applies to all the experiments carried out. Equation (2.5c) for σ_{pu} may now *under*-estimate the true matrix strength. The matrix strength should at least be as high as $f_{cc,\,95\%}$.

This yields for mix B, see Fig. 3.6b:

$$\sigma_{pu} > f_{cc,\,95\%} \approx 69.3 * (1 + 0.063 * 1.64) = 76.5 \ \text{N/mm}^2$$

which is satisfied for a 15% increase in the exponent 0.56, thus:

due to dowel action: $f_{ccm}^{0.50} \approx 0.56 * f_{ccm}^{0.64}$ $[\text{N}^{1/2}/\text{mm}]$ (5.8a)

due to interlocking: $\sigma_{pu} \approx 4.76 * f_{ccm}^{0.64}$ $[\text{N/mm}^2]$ (5.8b)

This adaptation leads to matrix strengths which change by less than 5% from their original values, for f_{ccm} ranging from 40 to 75 N/mm^2. See also Fig. 5.3 and in [26].
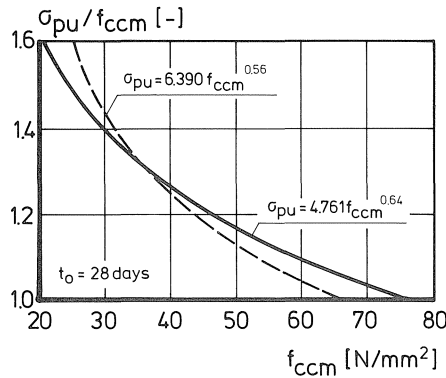
Fig. 5.3. Basic and modified formulae.

b. *Proposed time-dependent matrix strength $\sigma_{pu}(t)$*

The macroscopic deformation of the matrix material is restricted to a volume close to the surface of an aggregate particle. The average thickness of the matrix layer embedding a gravel particle is less than $t = 0.20$ mm. Consequently, the maximum shear slip amounts to $2 * t\sqrt{2} = 0.45$ mm before two opposing particles make contact in the crack plane. The *elastic* deformation provides a negligible slip of about $0.005t$ [mm]. The matrix stiffness is expected to be high due to local confinement. Virtually, the calculation considers an unfavourable situation: the interlock model appears applicable to a parallel displacement of more than 1 mm.

Creep phenomena of concrete are usually characterized by short and long-term components of deformation. The shift or "change-over" becomes evident in the form of a clear adjustment to a lower creep rate after a rather short sustaining period. However, this was not noticed for the crack displacements, even after an observation period of more than nine months, see chapter 4. Besides the normal stress on the contact areas a_x, a_y, the matrix also experiences a shear stress $\tau_{pu} = \mu\sigma_{pu}$. Thus, a multiaxial compression state exists which is even more complex due to time-dependent aspects. Based on

the preceding remarks, it was decided to use a *strength* criterion for the description of the time-dependent constitutive relation of the matrix.

A major parameter is the 28-day cube compressive strength f_{ccm} which affects both the interlocking of the crack faces and the dowel action of the bars. It is postulated that a strength reduction may evolve as a function of f_{ccm}, the duration of load application and the concrete age at the onset of loading denoted by t and t_0 respectively. In the qualitative sense, this strength decrease agrees with the observed macroscopic behaviour of cement-based materials subjected to a constant normal stress. The long-term strength f is directly associated with the uniaxial compressive strength f_{ccm} of concrete at $t_0 = 28$ days [25, 65, 77]:

$$f(t) = \lambda'_f(t, f_{ccm}) * f_{ccm} \quad (\lambda'_f \leq 1) \quad [\text{N/mm}^2] \tag{5.9a}$$

where $\lambda'_f = 1.0$ at the instant $t = 0$ h; λ'_f denotes a damage parameter. Equation (5.9a) presumes a *multiplicative* character of the material deterioration process. Combining equations (5.8b) and (5.9a) leads to:

$$\sigma_{pu}(t) = \lambda_f(t, f_{ccm}) \cdot \sigma_{pu}(t = 0) \quad (\lambda_f \leq 1) \quad [\text{N/mm}^2] \tag{5.9b}$$

where damage parameter λ_f is related to λ'_f according to:

$$\lambda_f(t, f_{ccm}) = [\lambda'_f(t, f_{ccm})]^{0.64} \quad [-] \tag{5.9c}$$

Obviously, the actual behaviour of the matrix is based on processes acting at a lower level and demanding a deep insight into and knowledge of the internal structure of the material [78]. However, the approach chosen refers to a so-called engineering model. Similar types of model have also been applied to other phenomena, such as crack width behaviour due to imposed deformations in structural concrete [7, 9]. Generally, the physical processes of the detailed (meso- or) microlevel of observation are not considered. One should bear in mind the scatter of the test results as pointed out in chapter 4. Therefore, a strictly accurate formulation is not useful and does not improve predictions of the structural response of the crack.

c. *Proposed time-dependent friction coefficient $\mu(t)$*

Besides σ_{pu} the rough crack model offers a second "degree of freedom", viz. μ which was established as 0.40 for the case of monotonic shear loading. Friction contributes significantly to the transfer of τ_a across a crack. It also affects the relationship between the restraining stress σ_a and the crack displacements. Microscopic undulations cause a frictional mechanism. The actual contact area of two solids does not depend solely on the geometry of these micro-roughnesses, but is also determined by the way how these irregularities deform. Generally, friction can be divided into an adhesive and a deformational component. This latter term relates particularly to the contact between a rather stiff and a soft material, such as the interaction between gravel and the cement matrix respectively. The literature on tribology of materials does not supply any information about the time-dependency of μ. Two opposing processes may be important:

46

- gradual *smoothening* of the contact surface mainly due to the high compressive and shear stresses. These cause increasing local compression of the matrix, depending on the mix composition as well as on the local distribution and size of the pores. Loose small-sized granular pieces can form in the macrocrack when it is initiated ("split") or during the sliding of both crack halves parallel to one other. See Fig. 5.4. These particles may also have originally gathered in air voids and may then become compacted later under shear loading. This might affect the (macroscopic) friction;
- enhanced *roughening* of the contact surface. The sustained multiaxial loading may induce local fracture of the matrix layer close to the contact areas. Probably small cracks initiate in the matrix layer perpendicular to the contact surface [78]. Another process concerns microstructural repair of the deteriorated structure by re-hydration of C-S-H crystals [29].
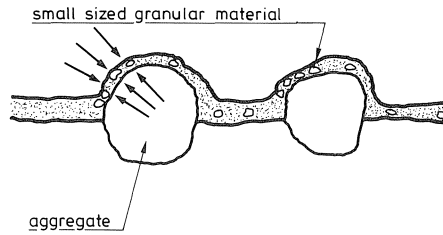
Fig. 5.4.   Shear sliding with small "interlayer" granular particles in the crack plane.

It is not clear which of the above mentioned mechanisms prevails as time passes. Therefore, a simple and general formula is proposed in which the damage parameter $\lambda_\mu(t)$ represents time-dependent effects:

$$\mu(t) = \mu(t=0) * \lambda_\mu(t) = 0.40 * \lambda_\mu(t) \quad [-] \tag{5.10}$$

Combining equations (5.3, 5.5a–b, 5.8–5.10) yields for the sustained loading case:

$$\tau = \lambda_f(t, f_{ccm}) * \sigma_{pu}\left[(A_y + 0.40\lambda_\mu(t) * A_x) + 0.204 * \alpha\gamma_d * \varrho f_{sy}^{0.50}\right] \text{ [N/mm}^2\text{]} \tag{5.11a}$$

$$\sigma = \lambda_f(t, f_{ccm}) . \sigma_{pu}\left[(A_x - 0.40\lambda_\mu(t) * A_y)\right] \qquad \text{[N/mm}^2\text{]} \tag{5.11b}$$

where $\varrho = n\pi d_b^2/4A_c$ and where α depends mainly on the loading eccentricity due to shear. There is comparable effects of λ_f on both transfer mechanisms.

Next, a computer program was especially developed in order to compare the theoretical model with the test data given in chapter 4. As for the reinforced crack the initial crack widths ranged from 0.01–0.06 mm. Two concrete grades and three reinforcement ratios were considered. The material properties used in the computer program are:
- *concrete:* mix A: $D_{max} = 16$ mm; $p_k = 0.70$; $f_{ccm} \approx 51$ N/mm^2
  mix B: $D_{max} = 16$ mm; $p_k = 0.67$; $f_{ccm} \approx 70$ N/mm^2
- *reinforcing steel:* $f_{sy} = 460$ or 550 N/mm^2; $d_b = 8$ mm; $\varrho = 1.12$–2.24%.

Contribution of the dowel mechanism

Fig. 5.5 shows the development of τ_{du}, for $A_c = 36000$ mm^2 and $d_b = 8$ mm, according to equations (5.1–5.5).
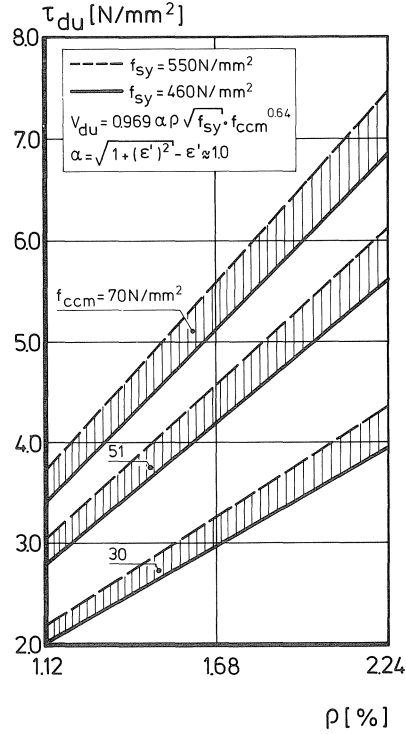
Fig. 5.5.   Dowel strength τ_{du} for $e = 1/2\delta_n = 0.20$ mm.

Contribution of the interlock mechanism

The contact areas A_x and A_y for a unit crack area were determined by numerical integration according to Walraven [74]. The crack-opening curves $100\tau_a/\sigma_{pu} = \alpha\,(\alpha = 0.5, 1, 2, \ldots 16)$ and $100\sigma_a/\sigma_{pu} = \beta\,(\beta = 0.5, 1, 2, \ldots 10)$ were all individually described by sets of third-order polynomes according to:

$$\delta_t = \gamma_1 + \gamma_2\delta_n + \gamma_3(\delta_n)^2 + \gamma_4(\delta_n)^3 \quad [\text{mm}] \tag{5.12}$$

where $\gamma_1 - \gamma_4$ are empirical constants. For given δ_n, δ_t the interlock stresses are linearly interpolated between the polynomes. Thus a discretization of interlock relationships is used. Figs. 5.6a–b present displacement paths of the crack for a monotonic shear loading. For the time-dependent case, these curves refer to a fully developed dowel load at the instant when the constant shear load has just been applied on the reinforced crack. Consequently, the sustained shear stress on the crack plane should conform to a minimum value, see equations (5.14a–b). Actually, the long-term behaviour of the crack is treated quasi-statically.

48
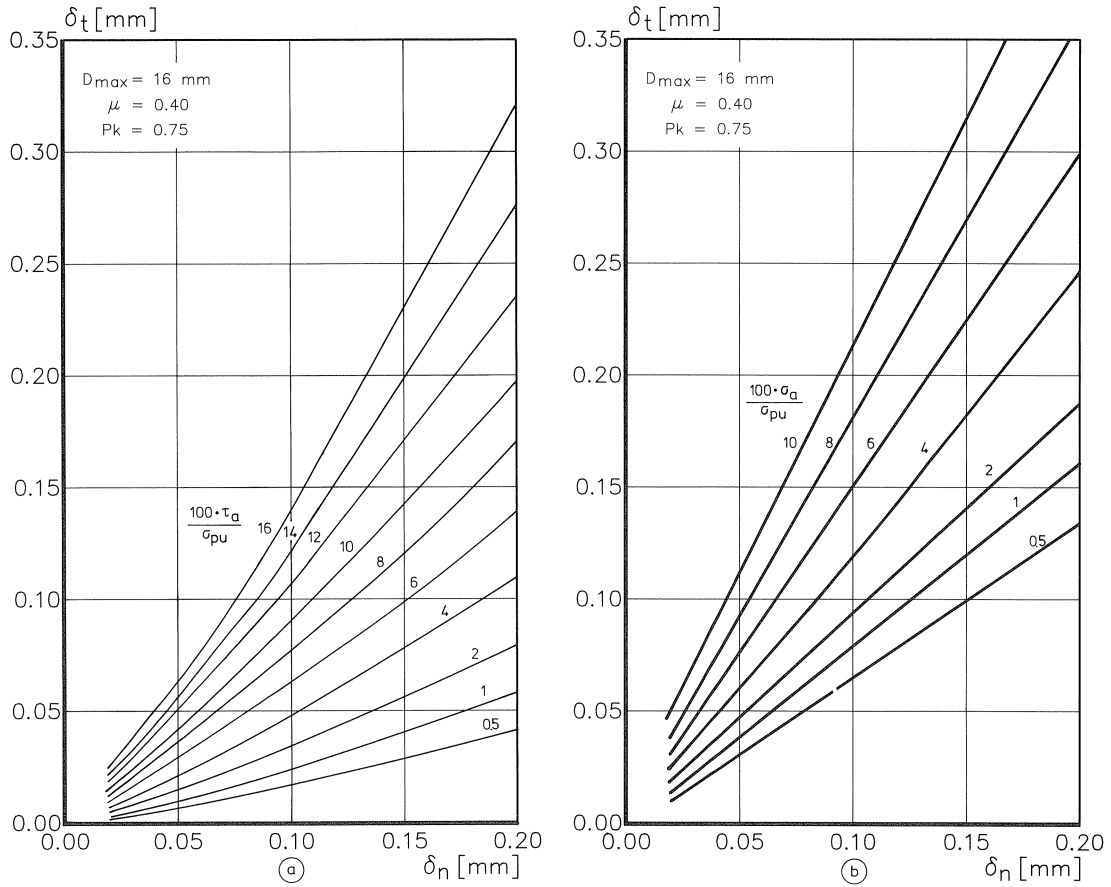
Fig. 5.6a–b.   Static δ_t-δ_n-curves according to the rough crack model.

5.4   *Experimental verification*

This section addresses the instantaneous and the time-dependent displacements of the crack plane. Next, empirical formulae are presented for the two damage parameters $\lambda_f(t)$ and $\lambda_\mu(t)$. Finally, the theoretical model is illustrated by a working example.

Instantaneous displacements

Measured average shear stress-crack width relations are compared with the calculations in Fig. 5.7. The test data are given for $\tau \leq 0.9\tau_u$: the computed dowel contribution is indicated separately. The predicted initial shear stiffness is relatively high. For widths < 0.20 mm – valid for nearly all the instantaneous displacements of the sustained tests –

the shear stresses differ less than 1.4 N/mm^2, see also Table 5.1. The different response may be attributed particularly to the sensitivity of the model to a change in the initial crack width according to equation (5.6c). Improved agreement was found for an exponent of 0.25 instead of 0.50. The computations revealed a fully developed dowel load at $\delta_t \approx 0.11$–0.13 mm, compared with $\delta_t = \delta_{no}$ and ≥ 0.10 mm in Fig. 5.2b.

Note that the differences in the crack-opening curves express the imbalance of shear forces so that the external load V exceeds the theoretical contributions of the interlock and dowel mechanisms. For equations (5.11a–b) a multiplicator c was needed. Using the recorded displacements of each test as input for the calculations, it followed that [27]:

$$\text{mix A: } \bar{c}(t = 0 \text{ h}) = 1.218 \qquad \text{v.c.} = 4.7\%$$
$$\text{mix B: } \bar{c}(t = 0 \text{ h}) = 1.391 \qquad \text{v.c.} = 3.7\%$$

where v.c. refers to the variation coefficient. The small scatter confirms that the displacement path is dominated by the actual concrete strength. The calculated compressive stresses perpendicular to the shear plane are not affected by a variation of ϱ. They agree quite well with strain gauge measurements carried out on one specimen of each mix, see section 4.5.

Table 5.1.   Ratios of predicted and measured shear stresses

τ at $\delta_n =$	$\bar{x}$	
	mix A	mix B
0.10 mm	1.20	1.06
0.15 mm	1.08	1.01
0.20 mm	1.00	0.94

The instantaneous crack widths δ_{nel} were accurately described by:

$$\delta_{nel} = n(\tau/\tau_u)^m \quad \text{[mm]} \tag{5.13}$$

where $n = 0.238(\varrho f_{sy})^{0.135}$ and $m = 4.127(\varrho f_{sy})^{-0.221}$. The average ratio of observed and calculated values amounts to 1.001 with a variation coefficient of less than 7.5%. Assuming that the dowel force of the bars has fully developed, then the *minimum* sustained shear stress levels are [25]:

$$\text{mix A: } \tau/\tau_u \geq 0.815 - 0.01 * \varrho f_{sy} \quad \text{[N/mm}^2\text{]} \tag{5.14a}$$

$$\text{mix B: } \tau/\tau_u \geq 0.860 - 0.01 * \varrho f_{sy} \quad \text{[N/mm}^2\text{]} \tag{5.14b}$$

where τ_u refers to equation (3.1a). These empirical formulae are based on computations according to the static model presented in section 5.2.

Time-dependent displacements

The crack-opening curves which refer to a monotonically increasing shear load are consistently steeper. Reliable relations were obtained for each test series according to:

$$\delta_t = \alpha(\delta_n)^\beta \quad \text{[mm]} \tag{5.15}$$
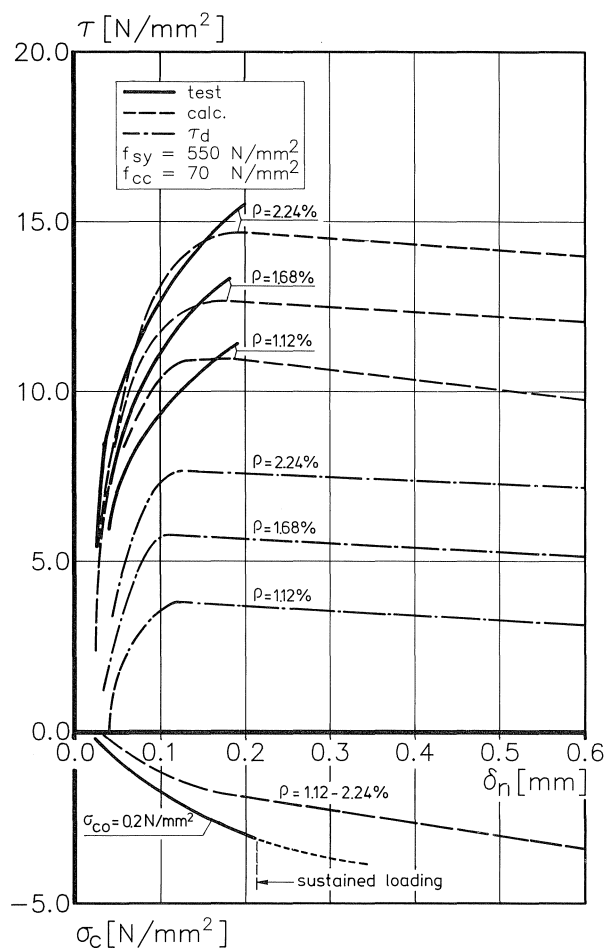
Fig. 5.7. Responses on a monotonic loading for mix B.

with correlation coefficient $r > 0.99$ in all cases, see also Table 5.2 and Fig. 5.8. The sustained shear tests refer to $\tau/\tau_u = 0.50\text{-}0.90$; $\varrho f_{sy} = 5.15\text{-}12.32$ N/mm^2; $\delta_{no} = 0.01\text{-}0.06$ mm and $0 \leq t \leq 10^5$ hours. There is a slight influence of both the shear stress level and the ultimate normal restraining stress ϱf_{sy}. The overall curves display only a significant effect of the concrete grade used.

Table 5.2. Coefficients α, β of equation (5.15)

loading	f_{ccm} [N/mm^2]	α	β
static	20–40	1.400	1.200
static	56	1.870	1.400
sustained	51	1.249	1.285
sustained	70	1.195	1.375

51
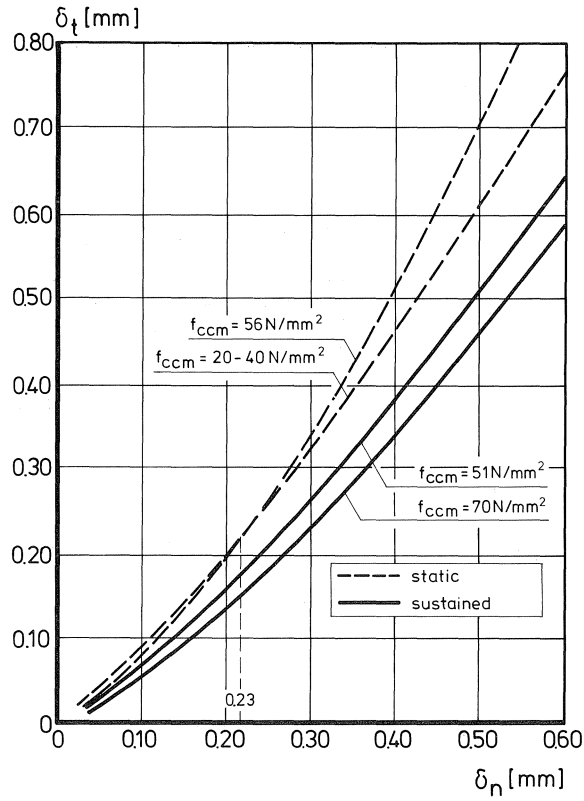
Fig. 5.8. Curves according to equation (5.15), see also Table 5.2.

The small distinction between the *static* crack-opening curves of Walraven ($f_{ccm} = 56$ N/mm^2) and those of this research ($f_{ccm} = 51$ or 70 N/mm^2) may be attributed to:
- different application methods used, viz. displacement-controlled with respect to the shear slip (Walraven's tests) versus load-controlled (this research). Gradual displacement increases of δ_n and δ_t were observed in between the stepwise application intervals of the external shear loading, particularly if $\tau \geq 0.5\tau_u$, see Fig. 5.9;
- the displacement range used for the empirical formulae denoted by equation (5.15). Walraven based his relationship on the recordings of the complete shear stress-displacement relations including the descending branch for which δ_t, $\delta_n > 1.0$ mm. However, the sustained shear tests usually refer to a maximum slip of less than 0.50 mm.

Damage parameters
The development of $\lambda_f(t)$ has been calculated for all the tests conducted. In Fig. 5.10a the shaded area corresponds to 90% of all the computational results of mix A. In general, the curves displayed a strong dependency on both the constant shear stress

52
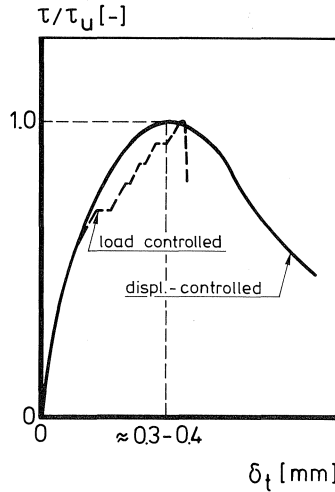
Fig. 5.9. Schematic response curves for two types of load application.

level applied and on the ultimate restraining stress ϱf_{sy}. However, these effects are not incorporated in the damage parameter according to the theoretical model. After a thorough analysis it was found that a time-dependent increase of the friction coefficient μ induces a considerable reduction in the shaded area. Figs. 5.10b–c shows two examples where final values $\mu(t = 10^5$ hrs) have been chosen as 0.50 and 0.60 respectively. A logarithmic expression appeared to satisfy well for μ. A further reduction of the "confidence area" is not useful in view of the accuracy and reliability of the test data. Therefore, equation (5.10) is represented by a simple formula:

$$\mu(t) = 0.40\lambda_\mu(t) = 0.40 * [1.00 + 100 * 10^{-3} * \log (t + 1)] \quad [-] \tag{5.16}$$

where $0 \leq t \leq 10^5$ hrs, see Fig. 5.11a. There is a remarkable change of λ_μ immediately after the onset of the test. The second damage parameter λ_f of equation (5.9c) has been successfully approximated by two empirical formulae for each mix, see Fig. 5.11b:

$$\text{mix A or B: } \lambda_f(t) = A + B * \log (t) \quad [-] \tag{5.17}$$

where $10^{-1} \leq t \leq 10^5$ hrs. B-values of each mix are gathered in Table 5.3. The A-values simply follow from $\lambda_f(0.1 \text{ h}) = 1.0$.

Table 5.3. Coefficients B of equation (5.17)

t [hrs]	B [10^{-3}]	
	mix A	mix B
10^{-1}–10^3	-13.949	-7.850
10^3 –10^5	-23.749	-10.751
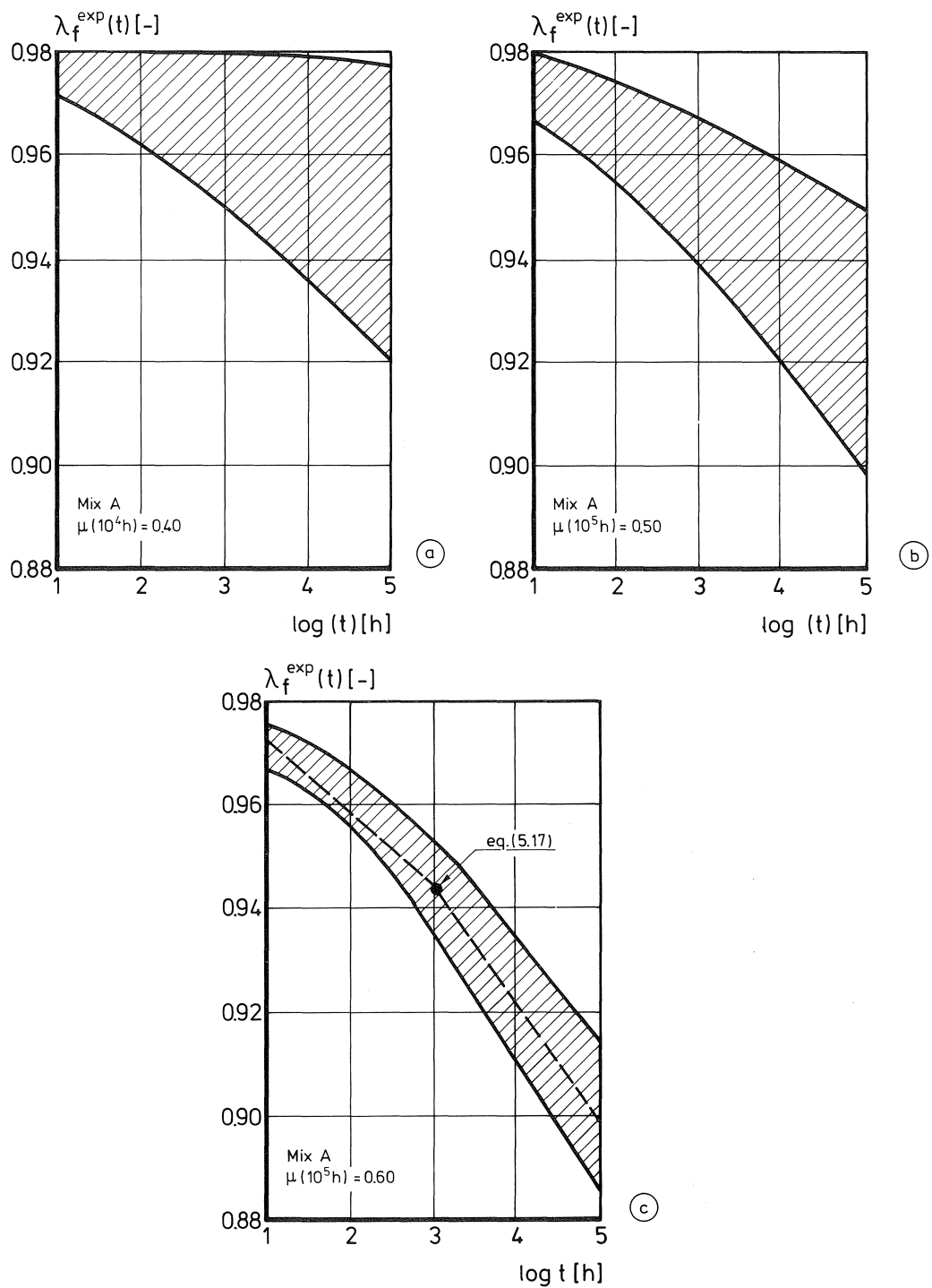
Fig. 5.10. Development of $\lambda_f(t)$ for (a) $\mu = 0.40$ and (b)-(c) for a gradual increase of the friction coefficient.

54
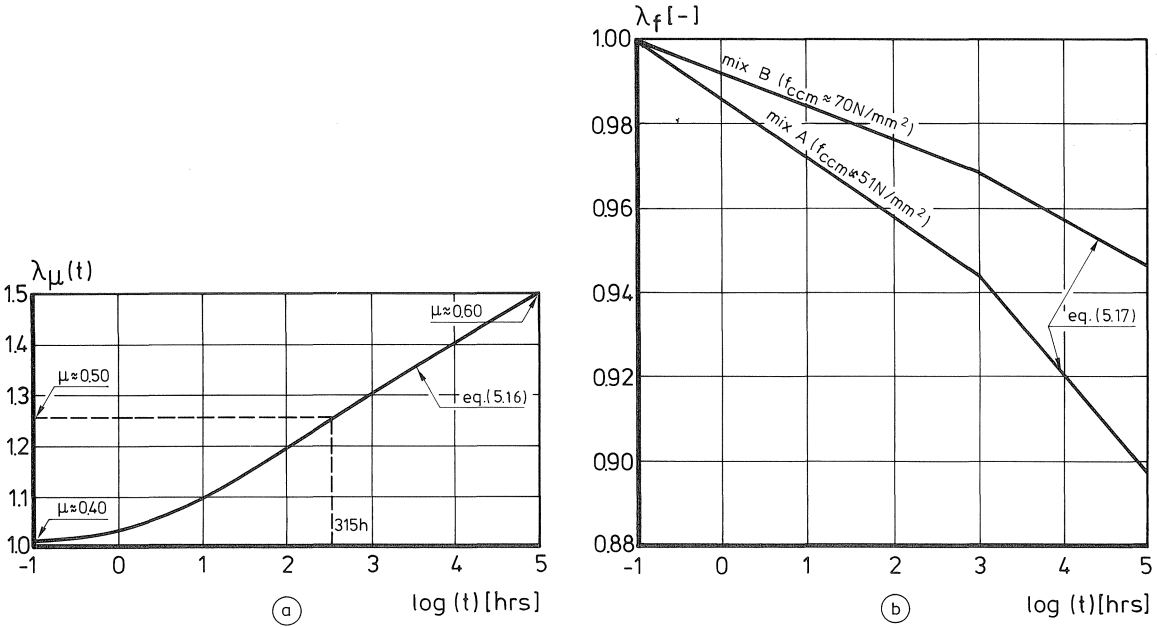
Fig. 5.11. Proposed damage parameters (a) λ_μ and (b) λ_f.

Both λ_f and λ_μ are written as logarithmic functions which resemble other types of material damage in case of a long-term application period, such as creep and fatigue [29, 37, 42, 59, 62, 77]. Apparently there is a significant difference between the deterioration processes in both types of concrete (or: matrix material). As indicated in Fig. 5.11b, mix A experiences relatively strong physical changes even for $t > 10^3$ hrs. The different responses of the concrete mixes cannot be fully attributed to the macroscopic material strengths σ_{pu} and f_{ccm}. The predicted displacement response of a single reinforced crack has been compared with the test data. The average ratios of measured and computed values ranges from 0.93 to 1.09 covering the two concrete grades tested. The computational procedure is outlined in appendix III.

Working example

The time-dependent behaviour of a single crack subjected to sustained shear loading has been predicted. The concrete properties are: mix A; $D_{max} = 16$ mm; $p_k = 0.70$; $f_{ccm} = 51$ N/mm^2. The initial crack width is 0.02 mm. The $120 * 300$ mm^2 shear plane is crossed perpendicularly by twelve 8 mm diameter steel bars ($f_{sy} = 460$ N/mm^2; $f_R = 0.050$) so that $\varrho = 1.68\%$. A stress $\tau = 0.9\tau_u = 10.65$ N/mm^2 has been permanently installed on the shear plane. The calculated instantaneous displacements amount to $\delta_{nel} = 0.238$ mm, $\delta_{tel} = 0.197$ mm according to equations (5.13) and (5.15). The results have been compared with the test data in Table 5.4. As shown in Fig. 5.12a there is a satisfactory agreement. Fig. 5.12b indicates a minor redistribution between both transfer mechanisms. Of course $\lambda_f(t)$ affects both of them.

55

Table 5.4. Comparison of the test data with the predicted time-dependent response. The damage parameters are indicated ($[*] = [\text{N/mm}^2]$)

| t [h]	δ_n^{exp} [mm]	δ_t^{exp} [mm]	δ_n^{cal} [mm]	δ_t^{cal} [mm]	λ_μ [−]	λ_f [−]	$\alpha\gamma_d$ [−]	σ_s [*]	τ_a [*]	τ_d [*]
0	0.250	0.217	0.238	0.197	1.000	1.000	0.982	35	5.18	5.47
1	0.324	0.304	0.317	0.285	1.030	0.986	0.970	58	5.30	5.35
10^1	0.361	0.354	0.364	0.341	1.105	0.972	0.966	62	5.39	5.26
10^2	0.409	0.414	0.392	0.375	1.200	0.958	0.966	63	5.47	5.18
$2*10^2$	0.423	0.434	0.406	0.392	1.230	0.954	0.965	65	5.49	5.16
$5*10^2$	0.443	0.462	0.426	0.417	1.270	0.948	0.964	65	5.56	5.12
10^3	0.459	0.485	0.460	0.460	1.300	0.944	0.962	66	5.56	5.09
10^4	0.515	0.569	0.540	0.566	1.400	0.921	0.958	67	5.65	5.00
10^5	0.570	0.670	0.578	0.607	1.500	0.897	0.957	68	5.71	4.94
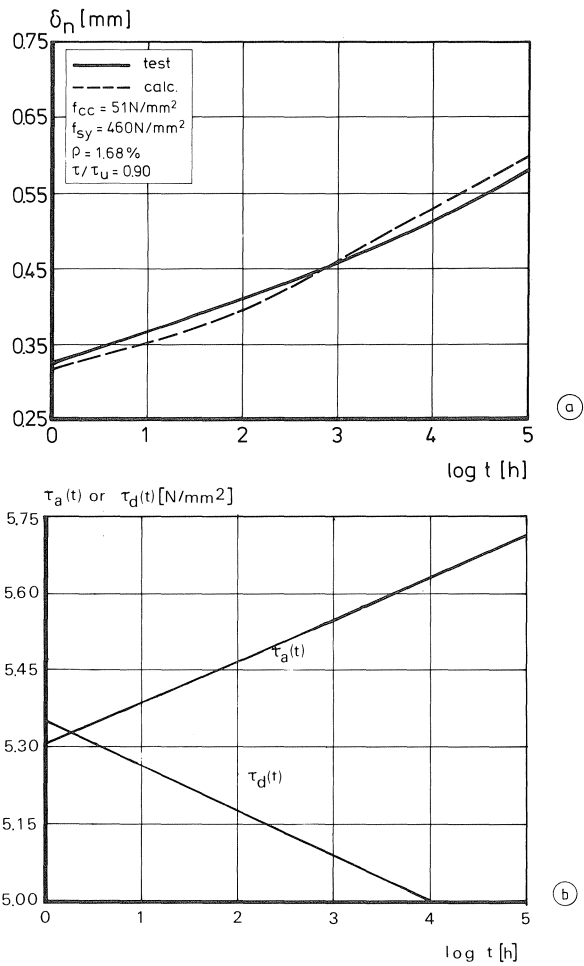
Fig. 5.12. (a) Comparison of displacement responses and (b) predicted redistribution between shear components.

5.5 *Evaluation of damage parameters*

Section 5.4 pointed out that the interlock mechanism dominates the *static* crack-opening path for a sufficiently large shear slip. For the case of a *sustained* shear loading, "damage" parameters were introduced into the theoretical model, enabling other (i.e. flatter) crack-opening directions to occur, see Fig. 5.8.

The distinction between the static and the *time-dependent* crack-opening curves is analysed in [27]. It is thought that bond creep of the embedded reinforcement leads to a reduced restraint of the crack. The restraint steel stress of the bars is quantified using equations (5.15–5.17) for the crack opening curves and the damage parameters respectively, see Fig. 5.13. For a constant parallel displacement of the crack, the static curves display rather high steel stress values which correspond to small crack widths.
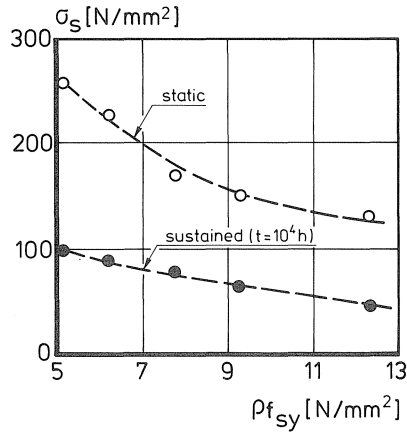
Fig. 5.13.   Calculated steel stresses at the centre of the crack plane, for mix A and $\delta_t = 0.55$ mm.

Now, suppose that the axial tensile stresses in the reinforcement are responsible for a time-dependent deformation increase in the concrete that surrounds the embedded bars. The precise distribution of bond stresses parallel to the dowel is not known but the *average* bond stresses in the interface layer – on the supported side of the dowel – are approximated according to (Fig. 5.14):

$$\bar{\tau}_{cs} = 0.5 A_s \sigma_s(t) / [0.5\pi d_b (1.5 d_b - 1.5)] = \sigma_s(t) / (6 - 6/d_b) \quad [\text{N/mm}^2] \qquad (5.18)$$

This calculation is based on a linear distribution of τ_{cs} across the slip layer and on a parabolic distribution parallel to the bar axis and along the circumference $0.5\pi d_b$. For $d_b = 8$ mm this yields: $\tau_{cs,max} = 0.86\sigma_s(t)$. These high bond stresses are transferred as a result of multiaxial confinement of the material under the dowel, situated close to the crack plane. Next, the time-dependent shear deformation of the interface layer is related to a change in the crack width. The computational results agree quite well with the recorded displacement shift. The high-strength concrete (mix B) displays a larger shift in time. This has been verified using the above-mentioned calculation procedure.

shear plane →

no bond

1.5d_b – 1.5mm

||| assumed bond stress distribution
/// matrix material with significant shear deformation

Fig. 5.14. Simplified representation of the bond stress distribution under the dowel accounting for the gradual crack width increase.

Finally, a simple power-function is proposed for the time-dependent δ_n-δ_t relationship provided that $\varrho = 1.1$–2.2%. In this case the coefficients of equation (5.15) need to be adapted to:

$$\alpha = 2.166 * f_{ccm}^{-0.140} \quad [mm] \quad \text{and} \quad \beta = 0.554 * f_{ccm}^{0.214} \quad [-] \tag{5.19}$$

The sustained shear tests conducted on *cracked plain* concrete have also been analysed. The restraining stress-crack width relations were used as input for the calculations, approximated by $\sigma_c(t) = \sigma_{co} + \alpha \cdot \sqrt{(\delta_n - \delta_{no})}$ where α is an empirica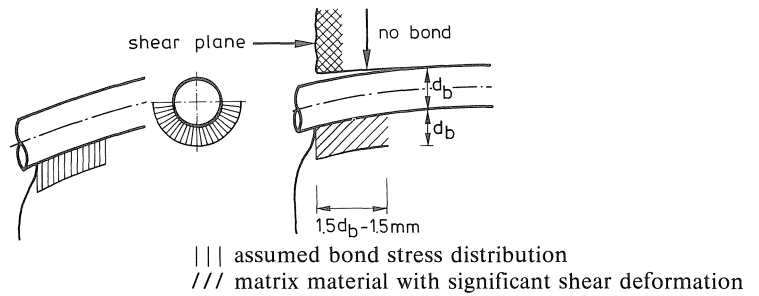l constant. The damage parameters λ_f and λ_μ were also incorporated. The calculations revealed a strong influence of the normal restraint stress used. For $t = 0$–10^5 hrs the average ratios $\bar{x}$ of measured and computed (constant) shear displacements of the tests yielded 1.09 (mix A, v.c. $= 12.4\%$) and 1.07 (mix B, v.c. $= 11.3\%$). Consequently, the two damage parameters originally derived from the equilibrium of shear forces in the reinforced crack plane are also valid for a crack in plain concrete. Moreover, these parameters account for the time-dependent transfer of forces perpendicular to the shear plane.

5.6 Long-term strength

This section deals with the phenomena which influence the damage parameter λ_f in equation (5.17), so as to provide a better knowledge of the time-dependent behaviour of a cement-based material. A first attempt is to pay attention to concrete as research on this material is extensively reported in the literature. Moreover, concrete and matrix material considerably resemble each other [13, 29]:
- both are cement-based, so that crack formation is influenced by the hydration process;
- both display crack arrest, caused by aggregate particles or air voids, see Fig. 5.17a.
The following subjects are successively discussed in this section:
- development of the short-term and long-term strength;
- damage parameter λ_f and long-term strength.

Development of the short-term strength
It is obvious that the uniaxial strength of cement-based material is determined by

58

various parameters, such as the mix composition, type of cement, compaction method and curing conditions (T, RH). A purely theoretical prediction of the material strength is beyond the scope of this research. The first derivative of $f_c(t_0)$ is described by a hyperbolic expression. This rough approximation of the actual behaviour provides a simple formula for the short-term strength:

$$f_c(t_0) = \frac{f_{cm} * t_0}{(\alpha + \beta * t_0)} \quad [\text{N/mm}^2] \tag{5.20}$$

where:

f_{cm} = mean 28-day uniaxial strength of the material [N/mm²]
α, β = empirical coefficients based on test results
t_0 = material age [days]

See also Figs. 5.15a–b. For $t_0 \to \infty$ the maximum strength of the material is: f_{cm}/β. For usual circumstances the ratio $f_{c\infty}/f_{cm}$ varies from 1.0 to 2.0. Then the ratio of the 14-day and the 28-day material strength is 0.67–1.00. Values of α and β were calculated from short-term tests performed at $t_0 = 7$–149 days:

mix A: $\alpha = 3.785$; $\beta = 0.847$; $r = 0.93$; (34 cubes);
mix B: $\alpha = 2.533$; $\beta = 0.895$; $r = 0.89$; (44 cubes).
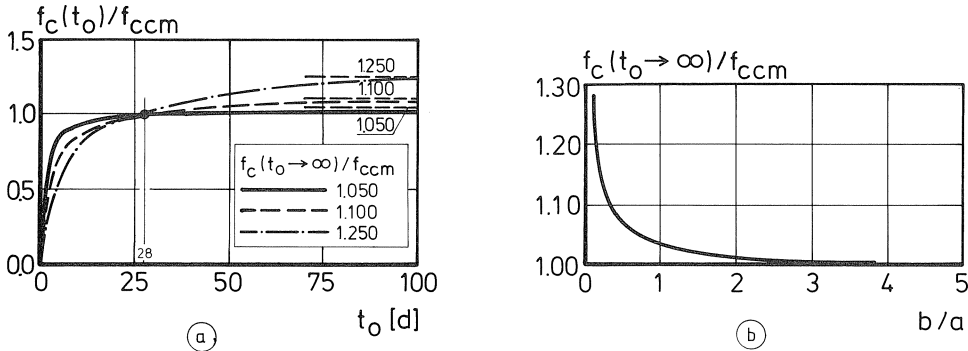
Fig. 5.15a–b. Some curves according to equation (5.20) and its first derivative.

Development of the long-term strength
Figs. 5.16a–b show the longitudinal and transverse deformation measured on sealed concrete specimens applied by uni- or biaxial compressive loading. Wittmann [77] indicated the similar response of different types of loading. He simulated the crack growth in a visco-elastic material with randomly distributed pores. Assuming equal critical crack lengths S^* for short-term and long-term failure (Fig. 5.17b), it was found for the strength ratio:

$$\eta(t, t_0) = \frac{f_{cc}\,(\text{long-term})}{f_{cc}\,(\text{short-term})} = m(t, t_0) \cdot \frac{f_{cc}(t, t_0)}{f_{cc}(t_0)} \sqrt{\frac{E_c(t_0)}{E_c(t, t_0)} \cdot \frac{1}{1 + \varphi_c}} \quad [-] \tag{5.21}$$

where η^* refers to the long-term strength of material, see Figs. 5.18a–b.
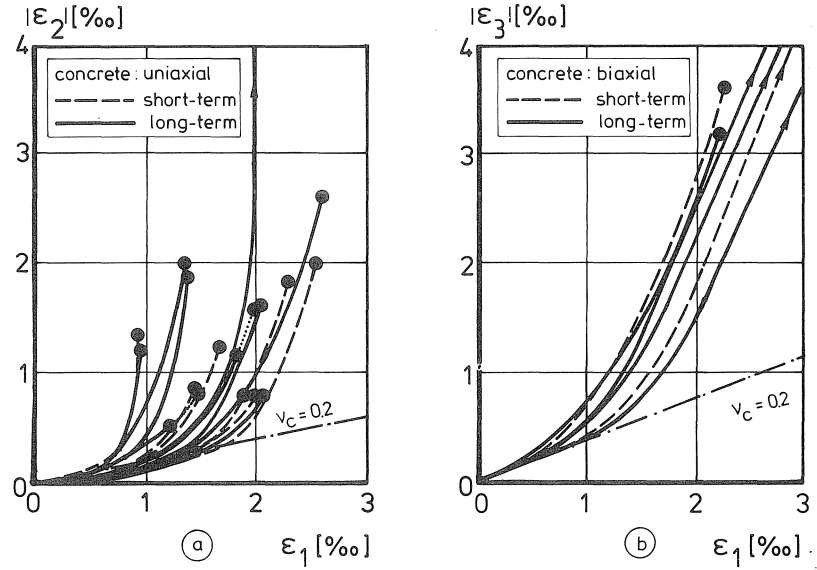
Fig. 5.16. (a) Uniaxial tests on $150 \times 150 \times 600$ mm prisms and (b) biaxial tests on $200 \times 200 \times 50$ mm sealed concrete plates [77].
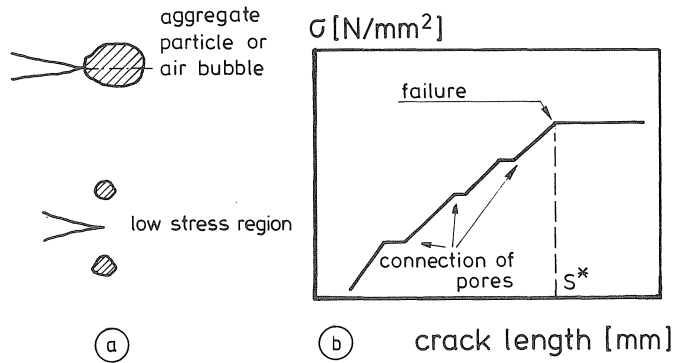
Fig. 5.17. (a) Crack arrest and (b) simulated development of crack length in a porous material [65, 77].

Equation (5.21) takes account of the two opposing processes in the material which take place at the microstructural level: crack growth (creep) and crack arrest (hydration; f_c and E_c gradually increase). The release of internal stress is expressed by $m > 1.0$ denoting that the short-term strength increases after a period of pre-loading. Types of η-curves according to Fig. 5.18a are also reported for multiaxial loading conditions, see in [24, 29, 65, 78]. An expression of the long-term strength ratio has been derived from an extensive Russian research program reported in [77]. The constant compressive stress levels were between 0.60 and 1.00; $t_0 = 7$–500 days; $f_{ccm} \approx 28$–60 N/mm^2. During the creep tests the ambient conditions were constant: 20 °C and 70% RH. The (safe) 5%
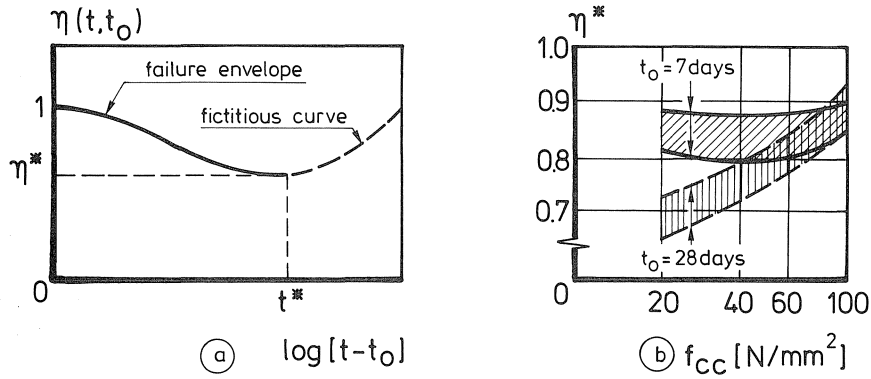
Fig. 5.18a–b. Examples of development of η and η^* [65, 77] for sustained compressive loading on concrete.

lower-boundary values of $\eta^* = \sigma_{cr}^*/f_c(t_0)$ have been expressed by a simple function of t_0 and the compressive strength of the concrete as:

$$\frac{\sigma_{cr}^*}{f_c(t_0)} = \frac{\log(t_0)}{p + q * \log(t_0)} \quad [-] \tag{5.22}$$

where

$$p = -1.1530 + 0.0364 * f_{ccm} - 3 * 10^{-4} * (f_{ccm})^2$$
$$q = 2.5314 - 0.0376 * f_{ccm} + 3 * 10^{-4} * (f_{ccm})^2$$

where σ_{cr}^* refers to the minimum sustained stress leading to material failure. Fig. 5.19 shows that the long-term strength ratio (≈ 0.77–0.80) displays a small variation for young concrete of moderate strength.

Remarkable differences occur for a concrete age $t_0 \geq 14$ days. In fact, the Russian test results revealed a considerable effect of the water content added to the concrete mix. A similar conclusion follows from the Eurocode [19] which prescribes the effect of the mix consistency on the time-dependent deformations (creep, shrinkage) of concrete.

Damage parameter λ_f and long-term strength
A long application period t yields for the damage parameter in equation (5.9a):

$$\lambda_f' \approx \sigma_{cr}^*/f_c(t_0) \quad [-] \tag{5.23}$$

For $t = 10^5$ h the λ_f'-values ($\lambda_f' = \lambda_f^{1/0.64}$, see Fig. 5.11b) are $0.844 * \beta = 0.844 * 0.860 = 0.728$ and $0.933 * 0.895 = 0.835$ for mix A and B respectively. Then the maximum ratio $f_{cc\infty}/f_{ccm}$ is assumed to be reached. Consequently, combining equations (5.17) and (5.23) leads to longer periods t:

$$\text{mix A: } \log(t) = \{1.0152 - (0.746/\beta)^{0.64}\}/23.749 * 10^{-3} \rightarrow t = 2.6 \text{ years}$$
$$\text{mix B: } \log(t) = \{0.9926 - (0.768/\beta)^{0.64}\}/10.751 * 10^{-3} \rightarrow t \gg$$

61
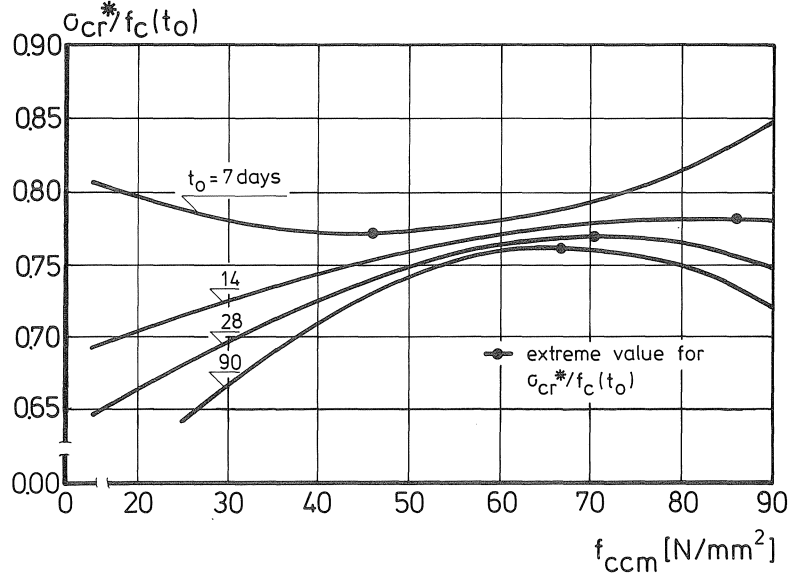
Fig. 5.19. Values of $\sigma^*_{cr}/f_c(t_0)$ according to equation (5.22).

The value of mix B is excessive in comparison with the life-time of concrete structures. Moreover, equation (5.22) considers lower-boundary values of σ^*_{cr} so that the average failure times are smaller. Both calculation methods reveal that mix B has a relatively large long-term strength ratio. One should bear in mind that the observations of the matrix material with respect to λ_f indicate an exponent 0.64 for the compressive strength of the concrete. This value was derived from the short-term tests but it is not certain whether it can be strictly maintained for the time-dependent case. For a sufficiently large period of load application it follows from equations (5.20–5.21) that:

$$\eta(t, t_0) = m(t, t_0) * \beta^{-1} * \sqrt{(\beta)^{1/3}/(1 + \varphi_c(t, t_0))} \quad [-] \tag{5.24}$$

where the modulus of elasticity is assumed to be in accordance with the Eurocode [19]. Coefficient m accounts for the release of internal stress. Generally, m depends on the type of loading, its duration and the constant stress level adjusted. Based on the analysis of several references, m was chosen as 1.10. With $1/\beta = 1.16$ (mix A) and 1.10 (mix B) and with long-term strength ratios $\lambda'_f = 0.728$ (mix A) and 0.835 (mix B), the creep coefficients are known:

$$\lambda'_f = \eta(t, t_0) \rightarrow \varphi_c(t, t_0) = 1.93 \text{ (mix A)} \quad \text{and} \quad \varphi_c(t, t_0) = 1.04 \text{ (mix B)}$$

so that φ_c(mix B)/φ_c(mix A) = 1.04/1.93 = 0.54. Creep deformation appears to be approximately proportional to (wcr)^2. The instantaneous deformation of the matrix material is equal to the ratio of the constant stress ($\cong f_{cc}^{0.64}$) and the modulus of elasticity ($\cong f_{cc}^{0.33}$). Now the ratio of the creep coefficients is:

62

$$\frac{\varphi_c(\text{mix B})}{\varphi_c(\text{mix A})} = \left(\frac{0.38}{0.50}\right)^2 * \left(\frac{51}{70}\right)^{0.31} = 0.52$$

This ratio agrees well with the theoretical prediction given above.

For young concrete at $t_0 = 7$ days, Fig. 5.19 indicates that the curve of the long-term strength ratio $\sigma_{cr}^*/f_c(t_0)$ diverges from the other curves. Young concrete exhibits a surplus of creep deformation as a function of the constant stress level applied. This refers to as "maturing creep". Ghosh [31] proposed four mechanisms to explain this phenomenon. Generally, it decays continuously with increasing maturity. The time-dependent physical processes are mainly governed by the rate and degree of hydration of the cement grains. Hydration has been quantified by the measured weight loss of concrete specimens heated to 105 °C and to 1050 °C respectively. These types of measurements were carried out for mix A and B at four different concrete ages [27], but the detailed analysis of the investigations has been omitted from this report.

6 Conclusions and outlook

The aim of the present study was to model the behaviour of a reinforced crack in concrete subjected to sustained shear loading. The tests and analyses resulted in a simple theoretical model based on Walraven's two-phase model and the modified empirical formula of Rasmussen. The long-term shear tests on cracks in plain and reinforced concrete are both adequately reflected by the analytical model provided that two empirical "damage" parameters are incorporated.

As stated before, fairly *high shear* stress levels were applied in view of the serviceability limit state of ordinary concrete structures. These levels were specifically chosen to attain reliable test data for long periods of load application. In fact, the measuring error of the crack displacements strongly influenced the shear stress levels applied in this research. The experimental results refer to complex practical applications for which severe and concentrated in-plane shear stresses may dominate the stiffness and/or stability of concrete structures. The theoretical model developed should be incorporated into advanced non-linear finite element programs which serve as an engineering tool for the structural designer.

The research also enables an accurate prediction of the time-dependent response of a crack in case of *low shear* stress levels, which correspond to usual structural applications where no excessive shear stresses are to be expected. Supplementary research may focus on the following subjects:

– *Numerical implementation* of the analytical model. As the sustained shear transfer is modelled quasi-statically the approach proposed by Pruijssers [59] for the static loading case may be applied. Preferably, the time-dependency is represented by parallel Maxwell chains;

– *Damage parameters*. It is thought that the change in the friction coefficient is related to the fictitious period of contact between a certain part of the matrix layer and an aggregate particle of the opposing crack half. Both mixes investigated display dif-

63

ferent formulae for $\lambda_f(t)$. Its time-dependent development might relate to the porous structure and the degree of hydration of the matrix. In the macroscopic sense material deterioration is related to the long-term uniaxial compressive strength of concrete;

– Experimental verification of the extended model for *large initial* crack widths which exceed 0.10 mm. Although the theory supplies good predictions for both transfer mechanisms (interlocking and dowel action), there is a lack of test data to substantiate them. It is expected that larger crack widths will induce shear failure within the life-time of a structure, provided that a sufficient concrete cover prevents premature splitting. Failure might occur if the crack displacements reach the descending branch of the static τ-δ_n envelope curve. Other related points of interest concern the response on long-term shear loading for:
  - cracks crossed by reinforcing bars at inclination $\neq 90°$, see [45];
  - cracks in cases of an arbitrary degree of prestressing, viz. a combination of prestressing steel and conventional bars, see [7, 9];

– Although the microscopic observations in this study clearly reveal the presence of a plastic hinge close to the shear plane and a local shift of the neutral axis in the steel bar, the actual *bond mechanism* of the dowel is not known. The rather flat crack-opening curves of the sustained tests are attributed to the time-dependent shear deformation of matrix material in the interface layer of the dowel. However, the explanation is based on a rather rough approximation of the real mechanism.

Notation

Unless otherwise stated, the dimensions are N, mm or N/mm^2.

a_x, a_y — projected contact areas A_x and A_y for a particle [mm^2]

d_b — bar diameter

f_b — bearing strength of concrete under a bar

f_{cc} — 150 mm cube compressive strength of concrete

f_{sy} — steel yield stress

g_i — boundary condition formulae or values $(i = 1, 2, ...)$

k — modulus of subgrade support [N/mm^3]

m — coefficient of internal stress release [−]

n — ratio E_s/E_c or number of observations [−]

p_k — volume of the particles/total concrete volume [−]

r — radius of particle or coefficient of correlation [−]

t — duration of load application [d] or thickness of matrix layer

t_0 — age of concrete at start of test [d]

t_f — duration to failure [d]

A_c — cross-sectional area of concrete shear plane [mm^2]

D_{max} — maximum particle size

E_c — modulus of elasticity of concrete

E_s — modulus of elasticity of steel

G_c — shear modulus of concrete

M_{pl} — plastic bending moment [Nmm]

V_d — dowel force

α — empirical constant

β — empirical constant or shear retention factor [−]

γ_a, γ_d — reduction factor for normal and/or shear stress [−]

δ_n, δ_t — crack width (or: separation), slip (or: parallel displacement)

δ_{nc} — separation increase due to sustained loading

δ_{nel} — instantaneous separation

δ_{no} — initial separation

ε_c — creep deformation of concrete [−]

η — strength ratio [−]

λ_f, λ_μ — "damage" parameters related to $t = 0$ h [−]

μ — coefficient of friction [−]

ϱ — reinforcement ratio (A_s/A_c) [−]

σ_a — normal stress due to aggregate interlock

σ_{pu} — yield stress of the matrix material

σ_s — steel stress

τ_a — shear stress due to aggregate interlock

τ_d — shear stress due to dowel action $= V_d/A_c$

τ_u — ultimate shear stress

φ_n — creep coefficient of cracked concrete $= \delta_{nc}(t)/\delta_{nel}$ [−]

$[\ ]$ — refers to references or to unit used

References

1. ACI-ASCE task-committee 426, The shear strength of reinforced concrete members – beams/slabs, Journ. of the structural div., ASCE, Vol. 99/100, No. ST6/ST8, June 1973/Aug. 1974, pp. 1091–1187/1543–1591.
2. BAUMANN, TH. and H. RÜSCH, Versuche zum Studium der Verdübelungswirkung der Biegezugbewehrung eines Stahlbetonbalkens, Deutscher Ausschuss für Stahlbeton, Heft 210, Berlin, 1970, pp. 45–83.
3. BAZANT, Z. P. AND P. G. GAMBAROVA, Rough cracks in reinforced concrete, Journal of the structural div., ASCE, Vol. 106, No. ST4, April 1980, pp. 819–842.
4. BENNETT, E. W. and S. BANERJEE, Strength of beam column connections with dowel reinforcement, The structural engineer, Vol. 54, No. 4, April 1976, pp. 133–139.
5. BIRKELAND, P. W. and H. W. BIRKELAND, Connections in precast concrete construction, ACI journal, Vol. 63, No. 3, March 1966, pp. 345–368.
6. BORST, R. DE, Non-linear analysis of frictional materials, Doctoral thesis, Delft University of Technology, 1986, 140 pp.
7. BRAAM, C. R. and J. W. FRÉNAY, Simple design method for partially prestressed concrete structures, IABSE Periodica, No. 3, 1989, pp. 77–94.
8. BROMS, B. B., Design of laterally loaded piles, Journal of the soil mechanics and foundations division, ASCE, Vol. 91, No. SM3, May 1965, pp. 79–99.
9. BRUGGELING, A. S. G., Structural concrete: science into practice, Heron, Vol. 32, No. 2, 1987, 67 pp.
10. CEDOLIN, L. and S. DEI POLI, Finite element studies of shear critical reinforced concrete beams, Journal of the eng. mech. div., ASCE, Vol. 103, No. EM3, June 1977, pp. 395–410.
11. COLLEY, B. E. and H. A. HUMPHREY, Aggregate interlock at joints in concrete pavements, Journal of the portland cement ass., Bulletin D124, Vol. 9, 1967, pp. 1–8.
12. COLLINS, M. P. and A. PORASZ, Shear design for high-strength concrete, in: Design aspects of high-strength concrete, 26th CEB plenary session, Dubrovnic, Sept. 1988, pp. 32–38.
13. Concrete mechanics: cooperative research between institutions in The Netherlands and the USA (eds. P. Gergely, R. N. White, J. W. Frénay, H. W. Reinhardt), June 1983, 161 pp.
14. CORDES, R., Statistische Untersuchung von Messfehlern zur Beurteilung der Verformungsansätze beim klassischen Standversuch, Bauingenieur, Vol. 53, 1978, pp. 139–146.
15. DEI POLI, S., P. G. GAMBAROVA and C. KARAKOC, Aggregate interlock role in reinforced concrete thin-webbed beams in shear, J. of struct. eng., ASCE, Vol. 113, No. 1, Jan. 1987, pp. 1–19.
16. DIVAKAR, M. P., A. FAFITIS and S. P. SHAH, A constitutive model for shear transfer in cracked concrete, J. of the struct. div., ASCE, Vol. 113, No. ST5, May 1987, pp. 1046–1062.
17. DULACSKA, H., Dowel action of reinforcement crossing cracks in concrete, ACI journ., Vol. 69, No. 12, Dec. 1972, pp. 754–757.
18. ELZANATY, A., A. H. NILSON AND F. O. SLATE, Shear capacity of reinforced concrete beams using high-strength concrete, ACI journal, Vol. 83, No. 2, March–April 1986, pp. 290–305.
19. Eurocode No. 2, Common unified rules for concrete structures, draft, April 1988, pp. 4.26–4.36.
20. FARDIS, M. N. AND O. BUYUKOZTURK, Shear transfer model for reinforced concrete, Journ. of the engineering mechanics div., ASCE, Vol. 105, No. EM2, April 1979, pp. 255–275.
21. FATTAH SHAIKH, A., Proposed revisions to shear-friction provisions, PCI journal, Vol. 23, No. 2, March–April 1978, pp. 12–21.
22. FENWICK, R. C. and TH. PAULAY, Mechanisms of shear resistance of concrete beams, Journal of the structural div., ASCE, Vol. 94, No. ST10, Oct. 1968, pp. 2325–2350.
23. Finite element analysis of reinforced concrete, ASCE state-of-the-art report, Ch. 5, 1982, 80 pp.
24. FOURÉ, B., Etude expérimentale de la résistance du béton sous contrainte soutenue, Béton, Vol. 229, No. 435, June 1985, pp. 3–22.
25. FRÉNAY, J. W. and H. W. REINHARDT, Creep analysis of structures, Fourth RILEM Symp. on Creep and shrinkage of concrete: mathematical modelling, Evanston, Aug. 1986, 12 pp.

26. Frénay, J. W., A. F. Pruijssers, H. W. Reinhardt and J. C. Walraven, Shear transfer in high-strength concrete, Proc. Symposium Utilization of high-strength concrete, Stavanger, June 1987, pp. 225–236.
27. Frénay, J. W., Time-dependent shear transfer in cracked reinforced concrete, Doctoral thesis, Delft Univ. of Techn., 1989, 170 pp. + app.
28. Furuuchi, H. and Y. Kakuta, Non-linear behaviour in dowel action of reinforcing bars, Transactions of the Japan concrete institute, Vol. 8, 1986, pp. 289–294.
29. Garrett, G. G., H. M. Jenning and R. B. Tait, The fatigue hardening behaviour of cement-based materials, Journal of the materials science, Vol. 14, 1979, pp. 296–306.
30. Gerstle, K. H., et al., Behaviour of concrete under multiaxial stress states, Journ. of the eng. mech. division, Vol. 106, No. EM6, Dec. 1980, pp. 1383–1403.
31. Ghosh, R. S., A hypothesis on the mechanism of maturing creep of concrete, Matériaux et constructions, Vol. 6, No. 31, 1973, pp. 23–26.
32. Hand, F. R., D. A. Pecknold and W. C. Schnobrich, Non-linear layered analysis of reinforced concrete plates and shells, J. of the struct. div., ASCE, Vol. 99, No. ST7, July 1973, pp. 1491–1505.
33. Hanson, N. W., Horizontal shear connections, Journal of the portland cement ass., Vol. 2, No. 2, May 1960, pp. 38–58.
34. Hofbeck, J. A., I. O. Ibrahim and A. H. Mattock, Shear transfer in reinforced concrete, ACI journal, Vol. 66, No. 2, Febr. 1969, pp. 119–128.
35. Houde, J. and M. S. Mirza, A finite element analysis of shear strength of reinforced concrete beams, Shear in reinforced concrete, ACI special publ. 42-5, 1974, pp. 103–128.
36. Hsu, Th. T. C., S. T. Mau and B. Chen, Theory of shear transfer strength of reinforced concrete, ACI structural journal, Vol. 84, No. 2, March–April 1987, pp. 149–160.
37. Jimenez, R., R. N. White and P. Gergely, Cyclic shear and dowel action models in reinforced concrete, Journ. of the structural div., ASCE, Vol. 108, No. ST5, May 1982, pp. 1106–1123.
38. Johansen, K. W., Brudlinieteorie (yield-line theory: English translation of the CCA, London, 1962), Copenhagen, 1943, 189 pp.
39. Kirmair, H. and R. Mang, Das Tragverhalten der Schubzone schlanker Stahlbeton- und Spannbetonträger bei Biegung mit Längskraft, Bauing., Vol. 62, 1987, pp. 165–170.
40. Kollegger, J. and G. Mehlhorn, Material model for cracked reinforced concrete, Proc. IABSE coll. Computational mechan. of concrete structures, Delft, Aug. 1987, pp. 63–74.
41. Krefeld, W. J. and C. W. Thurston, Contribution of longitudinal steel to shear resistance of reinforced concrete beams, ACI journal, Vol. 63, No. 3, March 1966, pp. 325–343.
42. Kupfer, H., S. Stöckl and H. Lanig, Kriechen und Restfestigkeit von Beton bei mehrachsiger Druckbeanspruchung, in: Stoffgesetze im konstruktiven Ingenieurbau, TU Braunschweig, 1988, pp. 63–70.
43. Marcus, H., Load carrying capacity of dowels at transverse pavement joints + discussion, ACI journal, Vol. 23, No. 2, Oct. 1951, pp. 169–183 + 184.
44. Mast, R. F., Auxiliary reinforcement in concrete connections, Journal of the structural division, ASCE, Vol. 94, No. ST6, June 1968, pp. 1485–1504.
45. Mattock, A. H., L. Johal and H. C. Chow, Shear transfer in reinforced concrete with moment or tension acting across the shear plane, PCI journal, Vol. 20, No. 4, July 1975, 18 pp.
46. Mattock, A. H., W. K. Li and T. C. Wang, Shear transfer in light-weight reinforced concrete, PCI journal, Vol. 21, No. 1, Jan.–Febr. 1976, pp. 20–39.
47. Mechanics of material interfaces, Proc. ASCE/ASME conference held in New Mexico (eds. A. P. S. Selvadurai and G. Z. Voyiadijs), Elsevier Publ., New York, 1986, pp. 63–77.
48. Mier, J. G. M. van, Examples of non-linear analysis of reinforced concrete structures with DIANA, Heron, Vol. 32, No. 3, 1987, 147 pp.
49. Millard, S. G. and R. P. Johnson, Shear transfer in cracked reinforced concrete + disc., Mag. of concrete res., Vol. 37/38, No. 130/134, March 1985/March 1986, pp. 3–15/47–51.
50. Mills, G. M., A partial kinking yield criterion for reinforced concrete slabs, Mag. of concrete research, Vol. 27, No. 90, March 1975, pp. 13–22.

51. MOOSECKER, W. VON, Zur Bemessung der Schubbewehrung von Stahlbetonbalken mit möglichst gleichmässiger Zuverlässigkeit, Deutscher Ausschuss für Stahlbeton, Heft 307, Berlin, 1979, 42 pp.
52. MÖRSCH, E., Der Eisenbetonbau – seine Theorie und Anwendung, Vol. 1, Part 2, 3rd edition, Konrad Witter, Stuttgart, 1909.
53. NIELSEN, M. P., Limit analysis of reinforced concrete slabs. Acta Polytechnica Scandinavica, 1963, pp. 167.
54. NISSEN, I., Rissverzahnung des Betons – gegenseitige Rissuferverschiebungen und über-tragene Kräfte, Dissertation TU München, 1987, 214 pp.
55. PAULAY, TH. and P. J. LOEBER, Shear transfer by aggregate interlock, Shear in reinforced concrete, ACI special publication 42-1, 1974, pp. 1–15.
56. PAULAY, TH., R. PARK and M. H. PHILLIPS, Horizontal construction joints in cast-in-place rein-forced concrete, Shear in reinforced concrete, ACI special publ. 42-27, 1974, pp. 599–616.
57. PERDIKARIS, PH. C. and R. N. WHITE, Shear modulus of precracked reinforced concrete panels, Journ. of structural eng., ASCE, Vol. 111, No. 2, Febr. 1985, pp. 270–289.
58. PRINCE, M. R. and K. O. KEMP, A new approach to the yield criterion for isotropically rein-forced concrete slabs, M. of concr. res., Vol. 20, No. 62, March 1968, pp. 13–20.
59. PRUIJSSERS, A. F., Aggregate interlock and dowel action under monotonic and cyclic loading, Doctoral thesis, Delft Univ. of Techn., 1988, 165 pp. + app.
60. RASMUSSEN, B. H., The carrying capacity of transversely loaded bolts and dowels embedded in concrete (in Danish), Bygningsstatiske Meddelser, Vol. 34, No. 2, 1963, pp. 39–55.
61. REINECK, K. H., Theoretical considerations and experimental evidence on web compression failures of high-strength concrete beams, in: Design aspects of high-strength concrete, 26th CEB plenary session, Dubrovnic, Sept. 1988, pp. 19–31.
62. ROSTÁSY, R. S. and B. KEPP, Time-dependence of bond, in: Bond in concrete, ed. by P. Bartos, Applied Science Publ., London, 1982, pp. 183–192.
63. ROTS, J. G., P. NAUTA, G. M. A. KUSTERS and J. BLAAUWENDRAAD, Smeared crack approach and fracture localization in concrete, Heron, Vol. 30, No. 1, 1985, 48 pp.
64. SAEMANN, J. C. and G. W. WASHA, Horizontal shear connections between precast beams and cast-in-place slabs, ACI journal, Vol. 61, No. 11, Nov. 1964, pp. 1383–1409.
65. SCERBAKOV, E. N. and J. V. ZAITSEV, Voraussage der Verformungs- und Festigkeitseigen-schaften von Beton unter Dauerlast, Cement and concrete research, Vol. 28, No. 102, March 1976, pp. 515–528.
66. SCHIESSL, P., Einfluss von Rissen auf die Dauerhaftigkeit von Stahlbeton- und Spannbeton-bauteilen, Deutscher Ausschuss für Stahlbeton, Heft 370, Berlin, 1986, 52 pp.
67. SCHIMMELPFENNIG, K., Bruchsicherheitsberechnung, Deutscher Ausschuss für Stahlbeton, Heft 257, Berlin, 1976, 48 pp.
68. TASSIOS, T. P. and E. N. VINTZELEOU, Concrete-to-concrete friction, Journal of structural engineering, Vol. 113, No. 4, April 1987, pp. 832–849.
69. TAYLOR, H. P. J., The fund. behaviour of reinforced concrete beams in bending and shear, Shear in reinforced concrete, ACI special publ. 42-3, 1974, pp. 43–77.
70. TELLER, L. W. and E. C. SUTHERLAND, The structural design of concrete pavements, Part 4, Public roads, Vol. 17, No. 7/8, Sept./Oct. 1936, pp. 143–171/175–192.
71. TIMOSHENKO, S. and J. M. LESSELS, Applied elasticity, Westinghouse Technical Night School Press, East Pittsburgh, 1925, pp. 133–141.
72. UTESCHER, G. and H. HERRMANN, Versuche zur Ermittlung der Tragfähigkeit in Beton einge-spannter Rundstahldollen aus nichtrostendem austenitischem Stahl, Deutscher Ausschuss für Stahlbeton, Heft 346, Berlin, 1983, pp. 49–104.
73. VECCHIO, F. J. and M. P. COLLINS, Predicting the response of reinforced concrete beams subjected to shear using modified compression field theory, ACI structural journal, Vol. 85, No. S27, May–June 1988, pp. 258–268.
74. WALRAVEN, J. C., Aggregate interlock: a theoretical and experimental analysis, Doctoral thesis, Delft University of Technology, 1980, 197 pp.

68

75. WALRAVEN, J. C., J. FRÉNAY and A. PRUIJSSERS, Influence of concrete strength and load history on the shear friction capacity of concrete members + discussion, PCI journal, Vol. 32/33, No. 1/1. Jan.–Febr. 1987/Jan.–Febr. 1988, pp. 68–84/165–170.
76. WHITE, R. N. and M. J. HOLLEY, Experimental study of membrane shear transfer + discussion, Journal of the structural division, ASCE, Vol. 98/99, No. ST8/7, Aug. 1972/July 1973, pp. 1835–1852/1664–1665.
77. WITTMANN, F. H. and J. ZAITSEV, Verformung und Bruchvorgang poröser Baustoffe bei kurzzeitiger Belastung und Dauerlast, Deutscher Ausschuss für Stahlbeton, Heft 232, Berlin, 1974, pp. 66–145.
78. WITTMANN, F. H., Fundamental research on creep and shrinkage of concrete, Nijhoff Publ., London, 1982, pp. 149–170 + pp. 269–278.
79. YOSHIKAWA, H. and T. TANABE, An analytical model for frictional shear slip of cracked concrete, Proc. IABSE coll. Computational mechan. of concrete structures, Delft, Aug. 1987, pp. 75–86.
80. ZIENKIEWICZ, O. C., Non-linear problems: Finite element method in engineering sciences, McGraw Hill Book Co., 2nd ed., 1972, pp. 369–377.

Appendix I: Mix proportions

	components	[kg/m³]	sieve opening [mm]	[kg]	[cum. %]
mix A	sand	877.2	8–16	623.7	100.0
	gravel	1065.0	4–8	441.3	67.9
	cement-B	325.0	2–4	312.1	45.2
	water	162.5	1–2	220.9	29.1
			0.50–1	156.2	17.7
			0.25–0.50	110.3	9.7
			0.10–0.25	77.7 +	4.0
		2429.7 +		1942.2	
mix B	sand	857.3	8–16	596.5	100.0
	gravel	1018.5	4–8	421.9	68.2
	cement-B	420.0	2–4	298.3	45.7
	water	147.0	1–2	212.0	29.8
	superpl. 2.5%	10.5	0.50–1	148.6	18.5
			0.25–0.50	105.0	10.6
			0.10–0.25	93.5 +	5.0
		2453.3 +		1875.8	

The time-dependent development of the mechanical properties of both types of concrete (with respect to compressive strengths, tensile splitting strengths, shrinkage deformations and losses of weight by drying) are all reported in [27].
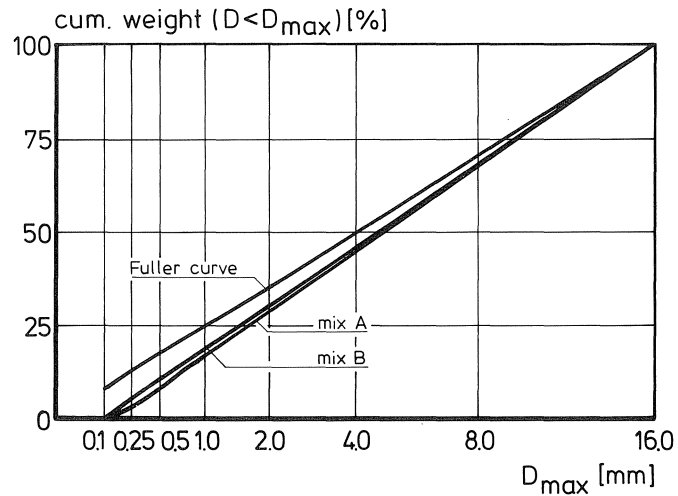
Appendix II: Sustained shear test results

The measured time-dependent crack-opening curves are presented on page 72–79. The first six figures refer to 34 shear tests on cracked *reinforced* concrete specimens. The last two figures correspond to eight tests on cracked *plain* concrete. Information about the related time-axis (duration of load application) and the development of the restraint stiffness of the shear plane is given in [27].

f$_{cc}$ [N/mm^2]	reinf. [%]	τ/τ_u [-]	δ_{no} [mm]	spec.no.	
50.0	1.12H	0.62	0.03	1	O
48.4	1.12L	0.84	0.03	2	●
47.6	1.12H	0.77	0.03	3	×
47.6	1.12H	0.77	0.03	4	+
43.6 *)	1.12H	0.78	0.01	5	△
48.4	1.12L	0.89	0.05	6	▽
50.0	1.12H	0.81	0.02	7	⋀
51.1	1.12H	0.85	0.01	7A	⋁

MIX A

*) t$_0$ = 10 days

*10^{-3} slip [mm]

*10^{-3} separation [mm]

72

MIX B

f$_{cc}$ [N/mm^2]	reinf. [%]	τ/τ$_u$ [-]	δ$_{no}$ [mm]	spec.no.	
70.8	1.12L	0.75	0.06	13	○
70.8	1.12L	0.75	0.03	14	●
73.6	1.12H	0.72	0.04	15	×
73.6	1.12H	0.72	0.04	16	+
67.3	1.12L	0.81	0.04	17	△
57.9 *)	1.12H	0.74	0.01	18	▽
67.3	1.12L	0.86	0.03	19	∧
67.1	1.12H	0.82	0.01	19A	∨
70.3 **)	1.12H	–	–	26	▲

*) t$_0$ = 10 days   **) uncracked

Y-axis: *10^{-3} slip [mm]

X-axis: *10^{-3} separation [mm]

73

MIX A

f_cc [N/mm²]	reinf. [%]	τ/τᵤ [-]	δ_no [mm]	spec.no.
56.7	1.68L	0.45	0.04	8 ○
56.7	1.68L	0.45	0.03	9 ●
53.2	1.68L	0.73	0.06	10 ✕
53.2	1.68L	0.73	0.05	11 +
49.5 *)	1.68H	-	-	25 △
51.1	1.68H	0.71	0.01	11A ▽
51.5	1.68H	0.75	0.01	11B ▲

*) uncracked

MIX B

f_cc [N/mm²]	reinf. [%]	τ/τ_u [-]	δ_no [mm]	spec.no.	
73.8	1.68L	0.55	0.02	20	○
73.8	1.68L	0.55	0.02	21	●
68.7	1.68L	0.69	0.03	22	×
68.7	1.68L	0.69	0.03	23	+
67.1	1.68H	0.70	0.01	23A	△
69.2	1.68H	0.70	0.01	23B	▽

75

MIX A

f$_{cc}$ [N/mm^2]	reinf. [%]	τ/τ_u [-]	δ_{no} [mm]	spec.no.	
53.5	2.24H	0.61	0.01	12	○
51.5	2.24H	0.66	0.01	12A	●

*10⁻³ slip [mm]

*10⁻³ separation [mm]

76

MIX B

f$_{cc}$ [N/mm^2]	reinf. [%]	τ/τ_u [-]	δ_{no} [mm]	spec.no.
73.2	2.24H	0.55	0.01	24 ○
69.2	2.24H	0.60	0.01	24A ●

$*10^{-3}$ slip [mm]

$*10^{-3}$ separation [mm]

MIX A

f_{cc} [N/mm^2]	d_b [mm]	τ/τ_u [-]	δ_{no} [mm]	σ_9 [N/mm^2]	spec.no.
58.0	10	0.80	0.02	2.0	5
49.0	10	0.69	0.02	1.0	6
58.0	10	0.65	0.02	1.0	7
52.6	16	0.73	0.02	0.9	9
58.0	16	0.49	0.01	2.0	10

MIX B

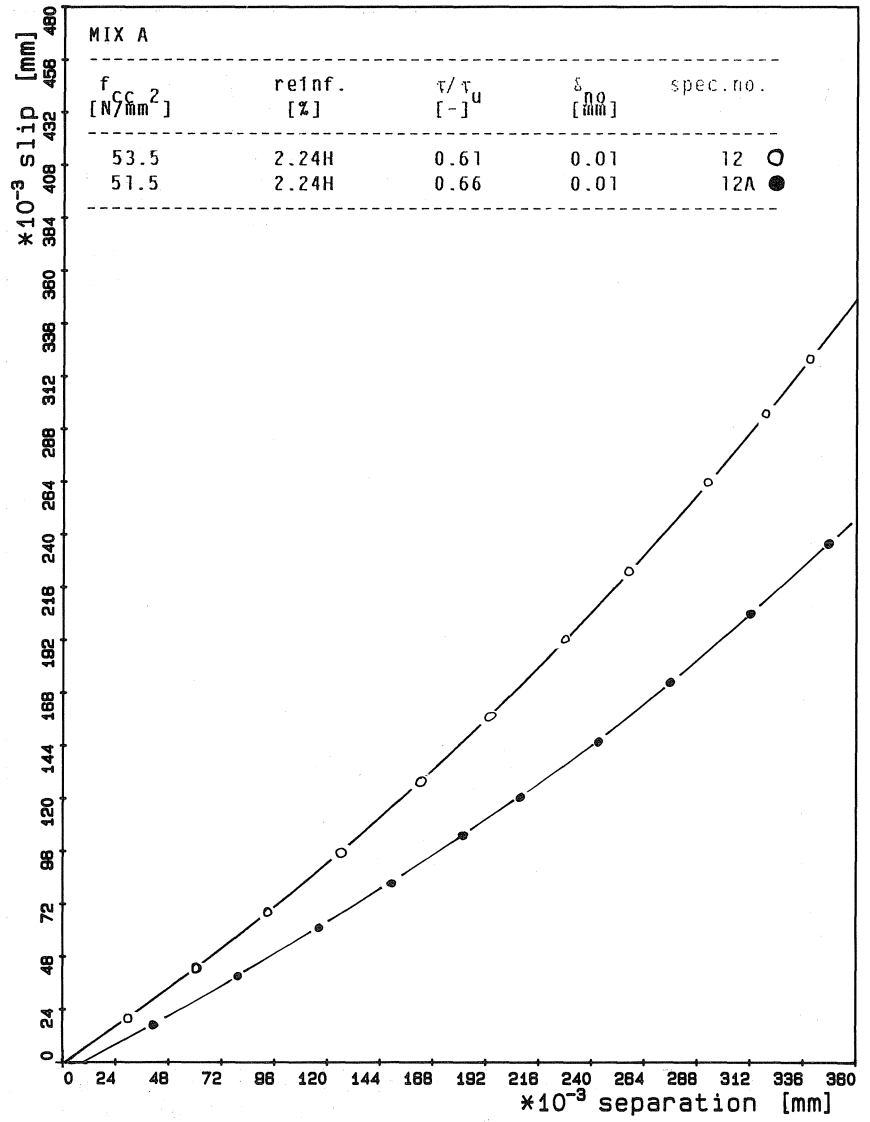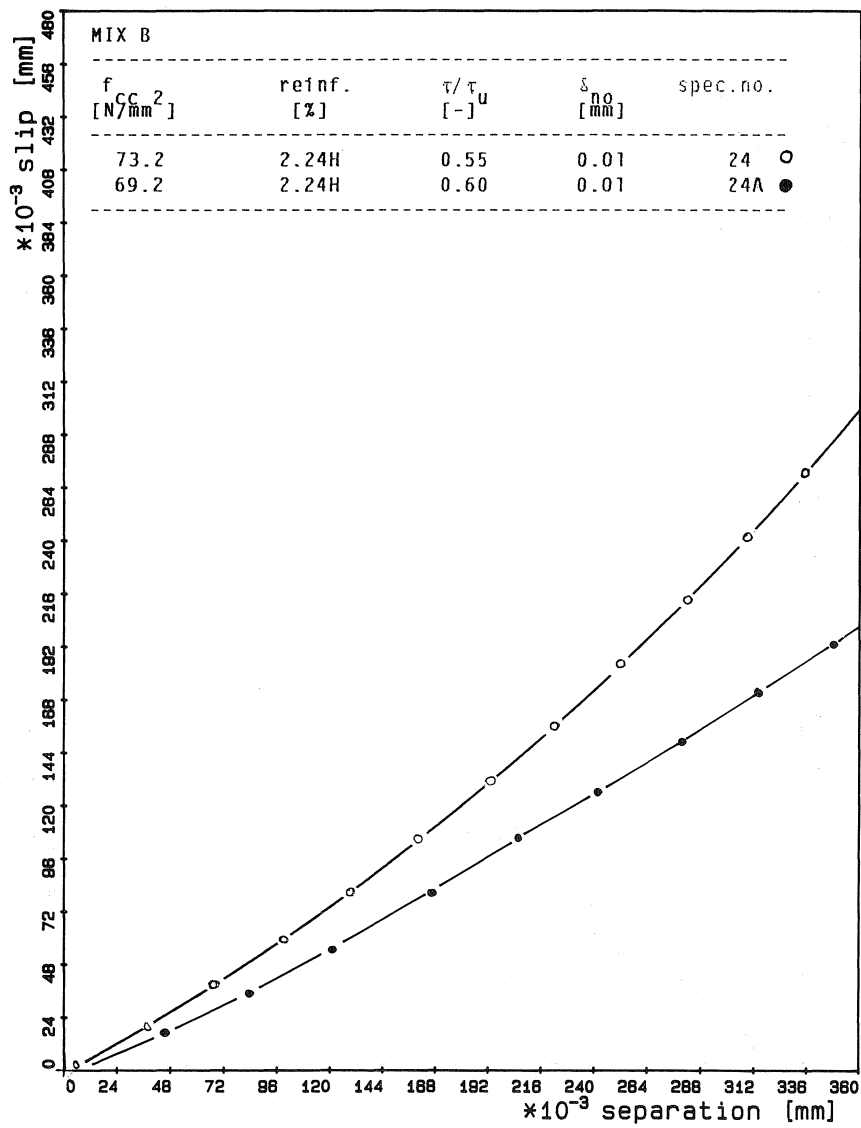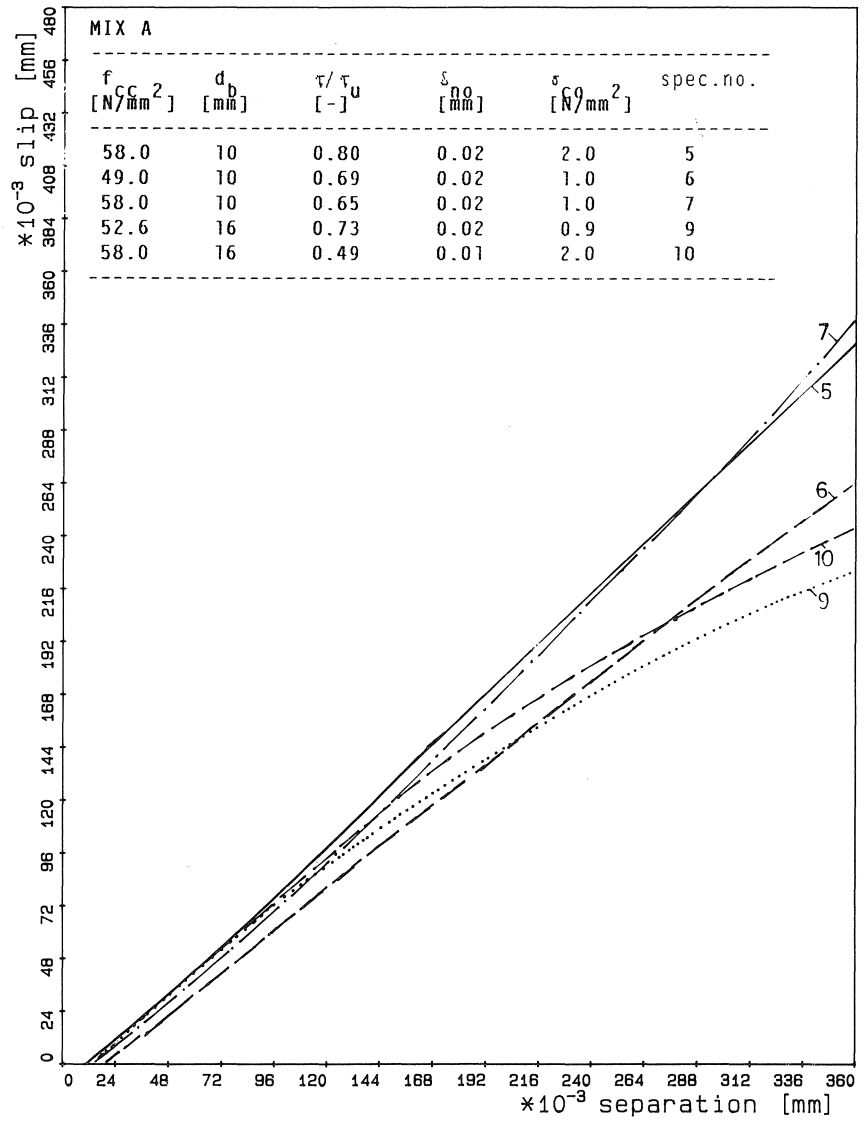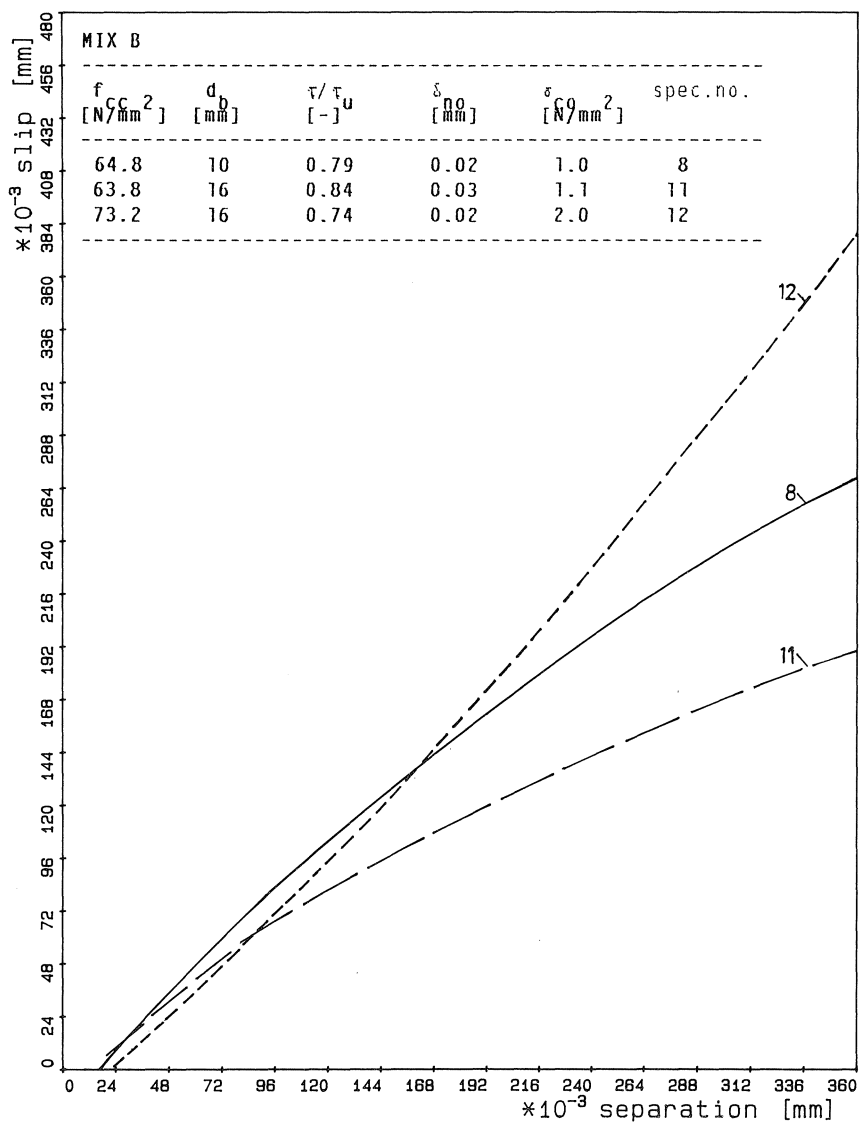| f_cc [N/mm²]	d_b [mm]	τ/τ_u [-]	δ_no [mm]	σ_no [N/mm²]	spec.no.
64.8	10	0.79	0.02	1.0	8
63.8	16	0.84	0.03	1.1	11
73.2	16	0.74	0.02	2.0	12

Appendix III: Computational procedure

The procedure given below can also be applied to transfer of *sustained* shear stress $\bar{\tau}$ (indicated by - - -) unless the friction coefficient $\mu(t)$ and damage parameters $\lambda(t)$ are considered, see section 5.3–5.5. Note that δ_n, $\delta_t \leq 0.80$ mm. The choice of the magnitudes of the variables should relate to the test range. Iterative computations are not indicated specifically.

Input: *concrete:* D_{max}, p_k, f_{ccm}, δ_{no}	type of mix
steel: d_b, f_{sy}, ϱ	$\tau = \bar{\tau}$, $t_i > 0$ h

$\delta_n \rightarrow \delta_t$ — eqs. (5.6c, 5.12) Figs. 5.6a–b

find δ_{nel}, δ_{tel} — eqs. (5.13, 5.19)

A_x, A_y — Fig. 2.10c

find $\lambda_f(t)$, $\lambda_\mu(t)$ — eqs. (5.16–5.17)

σ_a, τ_a, τ_{du} — eqs. (2.5a–c, 5.1, 5.4–5.6) and Figs. 5.5–5.6

γ_d — eq. (5.3)

find σ, τ — eqs. (5.11a–b)

$\tau \leq 0.9\tau_u$ — eqs. (3.1a–b, 5.14a–b)

(shear) stress-displacement relationships of crack found